1974

Elastic-plastic large deformation response of clay to footing loads, Davidson's Ph.D., February 1974 NTIS number: PB237524/AS (77-26)

Hugh L. Davidson

W. F. Chen

ELASTIC-PLASTIC LARGE DEFORMATION RESPONSE OF CLAY TO FOOTING LOADS

by

Hugh Lawson Davidson

A Dissertation

Presented to the Graduate Committee

of Lehigh University

in Candidacy for the Degree of

Doctor of Philosophy

in

Civil Engineering

Lehigh University

1974

CERTIFICATE OF APPROVAL

Approved and recommended for acceptance as a dissertation in partial fulfillment of the requirements for the degree of Doctor of Philosophy.

Jan. 9, 1974
(date)

Wai F. Chen
Professor in Charge

Accepted Jan. 18, 1974
(date)

Special committee directing the doctoral work of Mr. Hugh L. Davidson

Professor Ti Huang
Chairman

Professor Hsai-Yang Fang

Professor Dean P. Updike

Professor David A. VanHorn

ACKNOWLEDGEMENTS

The author is indebted to Professor Wai-Fah Chen, Professor in charge of this dissertation, for guidance and encouragement in the preparation of the dissertation. The guidance of Professors H. Y. Fang, T. J. Hirst, T. Huang, D. P. Updike and D. A. VanHorn, members of the special committee directing the author's doctoral work, is also acknowledged.

Special thanks are given to fellow graduate students Dr. Andrie Chen, Dr. Suresh Desai, Dr. John Struik and Dr. Negussie Tebedge with whom the author had many enlightening discussions concerning his dissertation. Further thanks are due Dr. Desai for helping the author become acquainted with the Lehigh University computer system.

The author gratefully acknowledges the free computer time granted by the Lehigh University Computing Center, without which this dissertation would have been impossible.

Acknowledgements are also due to Shirley Matlock for carefully typing the manuscript and to David VanCott and John Gera for preparing the figures.

TABLE OF CONTENTS

LIST OF TABLES

LIST OF FIGURES

ABSTRACT

An analytical study of the static response of a homogeneous clay stratum to footing loads is presented in this dissertation. Clay is modeled as a linear elastic-perfectly plastic material with the Drucker-Prager yield condition and associated flow rule. The effect of large deformations on the response of the clay is included in the analysis. Both drained and undrained analyses are considered.

In particular a single, strip surface footing bearing on a finite stratum of clay is considered. The footing is assumed to be rigid and the interface between the footing and soil may be either smooth or rough. The base of the soil stratum is rigid and perfectly rough. A plane strain condition is assumed.

Numerical techniques are utilized to solve this elastic-plastic, large deformation boundary value problem. The finite element method is used for spatial discretization, while an incremental integration scheme, referred to as the mid-point rule, is used to develop the complete load-displacement-stress response. A FORTRAN IV computer program was written to formulate and solve the governing equations.

A 50 ft. deep clay stratum loaded by a 5 ft. wide footing is treated in detail. Effective stress analyses for overconsolidated clays are presented for three different friction angles (all other material parameters are fixed). Total stress undrained analyses are presented for two values of Young's modulus, the other material

parameters being fixed. Footing load-displacement curves are shown for each problem considered, while stress distributions, zones of yielding and velocity fields are presented for selected problems only.

For reasonable values of both total and effective stress parameters, the results of small and large deformation analyses are found to differ only near the limit load. It was also determined that for a rough punch bearing on a von Mises or an extended von Mises (Drucker-Prager) material, the mode of failure corresponds to the so-called Prandtl velocity field. For a smooth punch bearing on either a von Mises or extended von Mises material, the failure mechanism does not exactly correspond to either a Hill or Prandtl type velocity field.

1. INTRODUCTION

1.1 The Physical Problem

The primary purpose of this dissertation is to present an analytical study of the static response of a homogeneous clay stratum to footing loads. Clay is modeled as a linear elastic-perfectly plastic material with the Drucker-Prager yield condition (22) and associated flow rule. The effect of large deformations on the response of the soil is included in the analysis. Both drained and undrained analyses are considered.

In particular we consider here a single, strip, surface footing bearing on a finite stratum of clay (loaded normally and centrally). The footing is assumed to be rigid and the interface between the footing and soil may be either smooth or rough. The base of the soil stratum is rigid and perfectly rough. A plane strain condition is assumed.

Footing width and stratum depth are two of the many parameters which affect this problem. However here we chose a single set of geometric parameters while allowing the material parameters of the soil to vary. As can be seen in Fig. 1, the footing is 5 ft. wide and the soil stratum is 50 ft. deep. In addition to this particular problem which is treated in Chap. 6, we also consider in Chap. 5 a shallow layer of undrained clay as well as some additional solid mechanics problems, e.g., a notched elastic-plastic tensile specimen and an elastic cantilever beam suffering large displacements. Also in Chap. 5 we examine, by means of numerical experiment, some of the

variables associated with the numerical solution techniques used here.

Numerical techniques are utilized to obtain the solutions presented herein. The finite element method (79) is used for spatial discretization while an incremental integration scheme, referred to as the mid-point rule, is used to develop the complete load-displacement-stress response. Constant strain triangles are used exclusively. A FORTRAN IV computer program was written to formulate and solve the governing equations. A brief description of this program is presented in Appendix III.

The principal physical problem considered here is clearly highly idealized. Clay is not strictly an elastic-plastic material nor are most soil strata homogeneous, and, in fact, most footings are submerged below the soil surface. Idealized problems are solved in order to gain insight, qualitative information and sometimes quantitative information with regard to real physical problems. The aim here is not to solve a particular problem but to look at a class of problems and to observe, through analysis, the behavior of the footing-soil system. The introduction of additional parameters associated with layered soil profiles, subsurface footings and more complex soil models would confuse rather than enlighten.

1.2 Previous Work

In the past few years a number of investigators have considered horizontal nonlinear clay strata subjected to vertical loads such as those transmitted by a footing. Some have treated soil as a

nonlinear elastic material while others have utilized elastic-plastic models. We consider first the nonlinear elastic investigations followed by elastic-plastic investigations.

Girijavallabhan and Reese (30) considered a circular footing bearing on an undrained clay where an isotropic nonlinear elastic model was used for the clay. Poisson's ratio was assumed to be constant and the secant value of the shear modulus was assumed to be uniquely related to the octahedral shearing strain. An iterative approach was used to solve the equilibrium equations and the finite element method was used to discretize the soil stratum. A model footing test was analyzed, and analysis and experiment were shown to agree reasonably well.

Desai and Reese (16) also used an elastic model and the finite element method to treat circular footings bearing on an undrained clay. An incremental approach was used to integrate the equations. It was assumed that in each increment the instantaneous stiffness of the clay could be described by a constant Poisson's ratio and a tangent value of Young's modulus. The incremental material parameters were obtained directly from undrained triaxial tests. Model footing tests for a single soil layer and two soil layers were analyzed. Experiment and analysis were shown to agree well.

Desai (15) used spline functions to numerically approximate undrained triaxial stress-strain data. An incremental integration scheme was utilized and incremental elastic parameters were determined directly from the spline functions. The finite element method was

used to analyze model circular footing tests, with good results. Some comparisons were also made between footing load displacement curves obtained from spline approximations and hyperbolic approximations for undrained triaxial stress-strain curves.

Duncan and Chang (23) used a hyperbolic representation for undrained triaxial stress strain curves. The finite element method and an incremental integration scheme were used to analyze circular footings bearing on undrained clay.

Hoeg, Christian and Whitman (35) used a finite difference technique to analyze a shallow layer of undrained clay subjected to a strip load. The clay was modeled as an elastic-perfectly plastic material with a Tresca yield criterion. The numerically determined limit load and the exact limit load were shown to be identical.

Tang and Hoeg (71) utilized a linear elastic-plastic strain hardening model developed by Christian (13) to treat strip footings bearing on frictional materials (e.g., normally consolidated clay). The soil model is similar to the strain hardening models proposed by Drucker et al (21) and Roscoe et al (61). A finite difference technique and an incremental integration scheme were used to solve the problem. The results were somewhat unsatisfactory with the load-displacement curve having a zig-zag character. Some dynamic problems were also considered with better results.

Fernandez and Christian (26) treated a strip footing bearing on undrained clay and both material and geometric nonlinearities were

included in the formulation. A hyperbolic nonlinear elastic model and an elastic-plastic Tresca model were used to describe the clay. The finite element method and the mid-point integration rule were utilized in the solution. The results were evidently very poor, particularly for the elastic-plastic model. The load displacement curves were very irregular and the numerical limit load was far above the theoretical limit load. It is not clear if large deformations were included or excluded in the footing problem treated in the report. However for the particular soil parameters utilized in the example, the changing soil geometry should have little affect on the results.

Hoeg (34) considered a circular footing bearing on a shallow layer of undrained soft clay in which the clay was assumed to be a linear elastic-linear strain softening material. An isotropic softening von Mises material model was utilized. The finite element method and an incremental integration technique were used to solve the problem. For a softening stiffness equal to about 20 percent of the elastic stiffness, the maximum load was found to be reduced by 40 percent.

Finally Zienkiewicz et al (84) treat a uniform strip load bearing on a soil obeying the Drucker-Prager yield condition and its associated flow rule. A combined iterative-incremental integration scheme in association with the finite element method was used to solve the problem. For the particular set of material properties considered, the iterative scheme failed to converge at a load which is approximately half of the theoretical limit load. No load displacement curve

was presented but zones of yielding at various load levels were shown.

1.3 Sign Convention for Stress

The typical continuum mechanics sign convention (tensile stresses positive) and the usual soil mechanics sign convention (compressive stresses positive) are shown in Fig. 1. In Chaps. 2 and 3 the continuum mechanics sign convention is utilized while the stresses reported in Chap. 6 follow the soil mechanics convention.

1.4 Scope of the Investigation

We present here plane strain analyses of a rigid strip footing bearing on elastic-perfectly plastic soil. Neither strain hardening nor strain softening is considered. Complete load-displacement histories are presented from zero load to failure, encompassing initial elastic behavior, contained plastic flow and collapse. We show also stress distributions and zones of yielding at various load levels and show velocity fields at the collapse state. Particular attention is given to the affect of the changing soil geometry on the response of the soil stratum to the footing loads. The finite element method and an incremental integration scheme are used to numerically solve the governing equations.

A von Mises model is used for total stress analysis of undrained clay while a Drucker-Prager model (extended von Mises) is utilized for effective stress (drained) analysis of overconsolidated clay. Some elastic-plastic analyses of undrained clay strata have appeared in the literature, as indicated in Sec. 1.2 However, the

more general case of a C-φ soil has been treated only briefly with inconclusive results. We present here in-depth treatment of both drained and undrained cases. In addition, a successful formulation and solution of the large deformation problem in soil mechanics is presented here for the first time. We also show, for the first time, that the well known Prandtl velocity field corresponds to the true failure mode for a rough punch bearing on an extended von Mises or von Mises material.

This dissertation is organized as follows. In Chap. 2 we discuss two elastic-plastic soil models--the Drucker-Prager perfectly plastic model and a strain hardening model of Roscoe and Burland (59). Incremental constitutive relationships are developed for both models. Incremental equilibrium equations for the large deformation problem are formulated in Chap. 3 and subsequently used to develop the instantaneous stiffness of a constant strain triangle. Incremental integration techniques are reviewed in Chap. 4. The mid-point rule and various details of the integration scheme used here are also discussed. Some example problems and numerical experiments are presented in Chap. 5,and drained and undrained analyses of a 50 ft. deep clay stratum are presented in Chap. 6. A summary and some conclusions are given in Chap. 7.

2. ELASTIC-PLASTIC STRESS-STRAIN MODELS FOR SOIL

2.1 Introduction

Since we propose here to make an analytical study of the response of soil to footing loads, we must necessarily select a mathematical model for soil stress-strain behavior. The amount of valid information that can be extracted from such a study is, of course, dependent upon the degree to which the mathematical model approximates real soil behavior. The complexity of soil stress-strain response might be cause for severe pessimism in this regard. However, the mechanical behavior of all materials is complex and must be drastically idealized in order to make mathematical analysis tractable. For example, metal behavior has been extensively investigated, yet in most analytical work metal is idealized as being a perfectly plastic, isotropic hardening or kinematic hardening material. In certain instances all three idealizations can be shown to fall short of real metal behavior. The proper idealization is, of course, problem dependent. For instance, most engineers would feel justified in using an elastic model for initial settlement analysis when the working load was far below the maximum bearing capacity of the foundation.

Soil is less amenable to simple modeling than is metal. Unlike metal, soil behavior is affected by hydrostatic pressure, and the tensile and compressive behavior of soils differ. Here we treat soil as a plastic material and assume that plasticity theory applies. We discuss in this chapter two elastic-plastic soil models--an elastic-perfectly plastic model and an elastic-plastic strain hardening model.

However, only the perfectly plastic model is used in the subsequent computations. We view both models as useful computational tools not as highly accurate predictors of detailed soil stress-strain behavior.

2.2 Typical Soil Stress-Strain Behavior

Some representative stress-strain curves for soil are shown in Fig. 2. For the moment we think in terms of a strain-controlled triaxial test, and except where noted stress means effective stress.

The stress-strain behavior of loose sand or remolded clay is characterized by a highly nonlinear response curve which rises to a maximum and remains there as straining is continued. The behavior of undisturbed insensitive clay is characterized by an initial linear portion and peak stress followed by softening to a residual stress. Sensitive clay behaves similarly except that the difference between the peak stress and the residual stress is substantial. Finally, undrained total stress behavior of clay is characterized by an initial linear portion and peak stress with perhaps some strain softening.

In the most fundamental sense, soil is a plastic material rather than an elastic material. For example, considering Fig. 2a, if we strain the soil to point A and then reverse the strain direction such that complete unloading takes place, we find that we are left with a residual strain, OB. A nonlinear elastic material would unload along loading path OA, and it is in this sense that soil is plastic rather than elastic.

It is of course not necessarily the case that soil stress-strain behavior can be successfully modeled using the classical theory of plasticity. It is in fact possible that nonlinear elastic models may be more suitable for most loading histories. Duncan and Chang (23) have used a nonlinear elastic model (with linear unloading) to successfully predict the response of a sand in the triaxial test when a fairly complex stress history was prescribed.

Here we choose to use elastic-plastic models to describe soil stress-strain behavior. We discuss first the Drucker-Prager perfectly plastic model followed by a Cambridge strain hardening model.

2.3 Drucker-Prager Perfectly Plastic Soil Model

The stress-strain curves shown in Figs. 2a, b, and d can all be approximated to some degree by a linear elastic-perfectly plastic model. It is unlikely however that a perfectly plastic idealization would be a useful model for sensitive clays. The complete description of an elastic-perfectly plastic model entails appropriate elastic constants, a yield function and a flow rule.

There exist a number of failure criteria which reflect a fundamental feature of soil behavior, that is, soil failure, unlike metal yield, is in some way a function of the hydrostatic stress component. The Mohr-Coulomb criterion (8) is certainly the best known of these criteria. Shield (66) presented a pictorial representation of the Mohr-Coulomb criterion in three-dimensional principal stress space and also discussed the criterion in the context of perfect

plasticity and the associated flow rule. Drucker and Prager (22) discussed an extension of the well known von Mises yield condition which included the hydrostatic component of the stress tensor, and subsequently Drucker (18) presented the so-called extended Tresca yield condition.

The extended von Mises yield function, as viewed in three-dimensional principal stress space, is shown in Fig. 3. The space diagonal is a line defined by $\sigma_1 = \sigma_2 = \sigma_3$ where σ_1, σ_2 and σ_3 are the principal stresses. Any plane perpendicular to the space diagonal is referred to as an octahedral plane. The extended von Mises yield condition is a cone with the space diagonal as its axis. The extended Tresca criterion is a pyramid with a regular hexagonal base and the space diagonal as its axes, while the Mohr-Coulomb criterion is a pyramid with an irregular hexagonal base and the space diagonal as its axis.

Bishop (8) has attempted to correlate all three criteria with experimental data and has concluded that the Mohr-Coulomb criterion best predicts soil failure. Roscoe, et al (62) contend that the available experimental data (particularly triaxial extension tests) are not sufficiently reliable to allow one of the criteria to be favored over the others. They thus recommend the extended von Mises criterion because of its simplicity. Furthermore, for the plane strain case it can be shown that in the limit state (where elastic strains are identically zero) both the extended von Mises and the extended Tresca criteria reduce to a Mohr-Coulomb type expression (18,22).

This implies that we can adjust the constants of the extended von Mises and extended Tresca criteria such that all three criteria will give identical limit loads. We note however that the three soil models will give different predictions for soil response below the limit load. In the spirit of the Cambridge soil models (64) and with the above discussion in mind, we utilize herein the Drucker-Prager condition (extended von Mises).

Yield Function

Referring the components of stress and strain to any Cartesian coordinate system with axes x, y and z, the Drucker-Prager yield criterion may be written as,

$$\alpha p + J_2^{1/2} = k \tag{1}$$

where p is the hydrostatic component of the stress tensor,

$$p = (\sigma_x + \sigma_y + \sigma_z)/3 \tag{2}$$

and J_2 is the second invariant of the deviatoric stress tensor,

$$J_2 = \frac{1}{6}\left[(\sigma_x - \sigma_y)^2 + (\sigma_x - \sigma_z)^2 + (\sigma_y - \sigma_z)^2\right] + \sigma_{xy}^2 + \sigma_{xz}^2 + \sigma_{yz}^2 \tag{3}$$

where σ_x, σ_y, σ_z, σ_{xy}, σ_{xz}, σ_{yz} are Cartesian stress components at a point in the soil, and α and k are material constants. If α is zero, Eq. 1 reduces to the von Mises yield condition. Referring again to the principal stress space shown in Fig. 3, $\sqrt{3}$ k corresponds to the radius of the cone at p = 0. We will find later that α is related to plastic volumetric strain.

In order that the Drucker-Prager and Mohr-Coulomb criteria give identical limit loads, α and k must be defined as follows (22)

$$\alpha = \frac{3 \tan\varphi}{\sqrt{(9 + 12 \tan^2\varphi)}} \tag{4}$$

$$k = \frac{3C}{\sqrt{(9 + 12 \tan^2\varphi)}} \tag{5}$$

where C is the cohesion and φ is the friction angle of the soil.

Stress-Strain Relations

In order to determine the elastic-plastic, incremental stress-strain relations, we start with the associated flow rule after Drucker (17) and write, in indicial notation,

$$\dot{e}^p_{ij} = \lambda \frac{\partial f}{\partial \sigma_{ij}} \tag{6}$$

where

$$f = \alpha p + J_2^{1/2} - k \tag{7}$$

and e^p_{ij} is the infinitesimal strain tensor with superscript p denoting plastic strain and the super dot denoting strain rate. The Cartesian stress tensor is denoted by σ_{ij}, and λ is an arbitrary non-negative number which is greater than zero for plastic loading ($f(\sigma_{ij}) = 0$) and equal to zero for plastic unloading or if the stress state lies within the yield surface ($f(\sigma_{ij}) < 0$). In general if the current stress state is known and the stress rate tensor is prescribed, the strain rate tensor is not uniquely determined since the plastic strains can only be defined to within the indeterminate parameter λ. Conversely if the strain rate is prescribed, the stress rate is uniquely determined. Since a displacement formulation is to be utilized

here, we wish to develop an expression relating stress rate as a function of strain rate. Thus λ will be determined as a function of the strain rate tensor.

The elastic rate relationship between the stress and strain is

$$\dot{\sigma}_{ij} = \frac{E}{1 + \nu}\left[\dot{e}^{e}_{ij} + \frac{\nu}{1 - 2\nu}\,\dot{e}^{e}_{kk}\,\delta_{ij}\right] \tag{8}$$

where E is Young's modulus, ν is Poisson's ratio, δ_{ij} is the Kronecker delta, e^{e}_{ij} is the elastic component of the strain tensor and we sum over repeated indicies. Noting that total strain rate, $\dot{e}_{ij}$, is the sum of elastic and plastic strain rates, we can relate stress rate to total strain rate, as follows,

$$\dot{\sigma}_{ij} = \frac{E}{1 + \nu}\left[\left(\dot{e}_{ij} - \lambda\,\frac{\partial f}{\partial \sigma_{ij}}\right) + \frac{\nu}{1 - 2\nu}\left(\dot{e}_{kk} - \lambda\,\frac{\partial f}{\partial \sigma_{kk}}\right)\delta_{ij}\right] \tag{9}$$

The stress-rate-strain rate equation is fully defined once λ is known. To determine λ we note that during plastic loading, the stresses must lie on the yield surface, $f(\sigma_{ij}) = 0$, and

$$df = \frac{\partial f}{\partial \sigma_{ij}}\,\dot{\sigma}_{ij} = 0 \tag{10}$$

that is, the stress rate vector must be tangent to the yield surface.

Equations 9 and 10 permit the determination of λ. To compute λ we start with some preliminaries as follows. From Eq. 7

$$\frac{\partial f}{\partial \sigma_{ij}} = \alpha\,\frac{\partial p}{\partial \sigma_{ij}} + \frac{1}{2}\,J_2^{-1/2}\,\frac{\partial J_2}{\partial \sigma_{ij}} \tag{11}$$

where

$$\frac{\partial p}{\partial \sigma_{ij}} = \frac{1}{3}\,\delta_{ij} \tag{12}$$

$$\frac{\partial J_2}{\partial \sigma_{ij}} = s_{ij} \tag{13}$$

and s_{ij} is the deviatoric stress tensor. Hence we can rewrite Eq. 11 as

$$\frac{\partial f}{\partial \sigma_{ij}} = \frac{1}{3}\,\alpha\,\delta_{ij} + \frac{1}{2}\,J_2^{-1/2}\,s_{ij} \tag{14}$$

From Eq. 14 we can write

$$\frac{\partial f}{\partial \sigma_{kk}} = \alpha \tag{15}$$

We note from Eq. 15, that

$$\dot{e}^{p}_{kk} = \lambda\,\frac{\partial f}{\partial \sigma_{kk}} = \lambda\,\alpha \tag{16}$$

Thus for α other than zero, plastic volume change is nonzero. Finally, using Eqs. 9, 14 and 15 we can rewrite Eq. 10 as

$$df = 0 = \left\{\frac{1}{3}\,\alpha\,\delta_{ij} + \frac{1}{2}\,J_2^{-1/2}\,s_{ij}\right\} \times \left\{\frac{E}{1+\nu}\left[\left(\dot{e}_{ij} - \frac{\lambda\,\alpha\,\delta_{ij}}{3} - \frac{\lambda J_2^{-1/2}}{2}\,s_{ij}\right) + \frac{\nu}{1-2\nu}\left(\dot{e}_{kk} - \lambda\,\alpha\right)\delta_{ij}\right]\right\} \tag{17}$$

This equation can be solved for λ, and after some simplification we obtain,

$$\lambda = \frac{G J_2^{-1/2}\,s_{pq}\,\dot{e}_{pq} + B\dot{e}_{kk}}{G + \alpha B} \tag{18}$$

where G is the elastic shear modulus,

$$G = \frac{E}{2(1 + \nu)} \tag{19}$$

and

$$B = \frac{2\alpha G}{3}\left[\frac{1 - \nu}{1 - 2\nu}\right] \tag{20}$$

To obtain the desired stress rate-strain rate relationship, Eq. 18 is substituted into Eq. 9 to give

$$\dot{\sigma}_{ij} = D_{ijpq}\,\dot{e}_{pq} \tag{21}$$

where

$$D_{ijpq} = \frac{E}{1 + \nu}\left[\delta_{ip}\,\delta_{jp} + \frac{\nu}{1 - 2\nu}\,\delta_{ij}\,\delta_{pq}\right] - \frac{\left[B\delta_{ij} + GJ_2^{-1/2}\,s_{ij}\right]}{G + \alpha B}\left[GJ_2^{-1/2}\,s_{pq} + B\delta_{pq}\right] \tag{22}$$

The matrix D_{ijpq} is referred to here as the elastic-plastic constitutive matrix.

For the plane strain case ($\gamma_{yz} = \gamma_{xz} = e_z = 0$) we can write, in matrix form,

$$\begin{Bmatrix} \dot{\sigma}_x \\ \dot{\sigma}_y \\ \dot{\sigma}_{xy} \\ \dot{\sigma}_z \end{Bmatrix} = [D] \begin{Bmatrix} \dot{e}_x \\ \dot{e}_y \\ \dot{\gamma}_{xy} \end{Bmatrix} \tag{23}$$

where the z axis is normal to the plane, γ_{xy} is the so-called engineering shearing strain,

$$\gamma_{xy} = 2e_{xy} \tag{24}$$

and

$$[D] = \frac{E}{(1+\nu)\ (1-2\nu)} \begin{bmatrix} 1-\nu & \nu & 0 \\ \nu & 1-\nu & 0 \\ 0 & 0 & (1-2\nu)/2 \\ \nu & \nu & 0 \end{bmatrix}$$

$$- \frac{1}{G + \alpha B} \begin{bmatrix} H_1^2 & H_1H_2 & H_1H_3 \\ H_2H_1 & H_2^2 & H_2H_3 \\ H_3H_1 & H_3H_2 & H_3^2 \\ H_4H_1 & H_4H_2 & H_4H_3 \end{bmatrix} \tag{25}$$

and

$$H_1 = B + GJ_2^{-1/2}\ s_x \tag{26a}$$

$$H_2 = B + GJ_2^{-1/2}\ s_y \tag{26b}$$

$$H_3 = GJ_2^{-1/2}\ \sigma_{xy} \tag{26c}$$

$$H_4 = B + GJ_2^{-1/2}\ s_z \tag{26d}$$

What we have done to this point is to develop a set of incremental stress-strain equations for soil using an elastic-perfectly plastic model. To the extent that soil failure can be predicted with the conventional material parameters C and φ, this model can capture soil failure (at least for plane strain). However this drastic idealization can not capture some important characteristics of soil behavior. For example, it has been often noted that the amount of dilation at failure predicted by the perfectly plastic model is considerably in excess of that observed experimentally

(19). According to Drucker (19) the failure surface for soil may not be the limit of a sequence of yield surfaces as is normally considered to be the case for metals. Accordingly, in the next section we discuss a strain hardening model which for some loading histories may more closely predict soil behavior than can a perfectly plastic model.

2.4 An Elastic-Plastic Strain Hardening Model

A Brief Historical Account

Considering again Fig. 2a, we note that long before the maximum stress has been reached some irreversible straining has occured as evidenced by the fact that unloading from point A leaves a residual strain. In the context of the theory of plasticity this soil might be referred to as a strain hardening material since the onset of plastic yielding is not synonymous with the maximum stress. A few researchers have investigated the possibility of modeling soil as a strain hardening material, and in particular this has been one of the major thrusts of the soil mechanics group at Cambridge University for the past twenty years (58).

Apparently Drucker, Gibson and Henkel (21) were the first to suggest that soil might be modeled as an elastic-plastic strain hardening material. They proposed that successive yield functions might resemble extended von Mises cones with convex end caps. As the soil strain hardens both the cone and cap expand. Drucker (19) again discussed this concept in a later paper in which he suggested that the failure surface may not be a yield surface. This point is

further emphasized by Drucker (20) who noted that successive loading surfaces or yield surfaces do not approach the failure surface.

In 1958 Roscoe, Schofield and Wroth (63) published a paper which contained the basis for a number of subsequent strain hardening models for soil. The paper was concerned primarily with the behavior of soil in the triaxial test and contained the so-called "state boundary surface" (called a yield surface in the 1958 paper) postulate and the "critical state line" postulate. These concepts were utilized by Roscoe and Poorooshasb (60) to develop a stress-strain theory for clay which was not, however, based upon the theory of plasticity. Calladine (10) suggested an alternate interpretation of this theory using concepts from strain hardening plasticity. Subsequently Roscoe, Schofield and Thurairajah (61) utilized the strain hardening theory of plasticity to formulate a complete stress-strain model for normally consolidated or lightly overconsolidated clay in the triaxial test. This model has since become known as the Cam-clay model (64).

Burland (9) suggested a modified version of the Cam-clay model and this model was subsequently extended to a general three-dimensional stress state by Roscoe and Burland (59). It is the modified Cam-clay model that we are concerned with here. We will see later that for certain stress histories modified Cam-clay strain softens rather than strain hardens.

Modified Cam-Clay

Modified Cam-clay is an isotropic, nonlinear elastic-plastic strain hardening material. Only volumetric strain is assumed to partially recoverable, that is, elastic distortional strain (shearing strain) is assumed to be identically zero. Elastic volumetric strain is nonlinearly dependent on hydrostatic stress and is independent of deviatoric stresses.

In order to introduce the reader gradually to the idea of soil as a plastic strain hardening material, we consider first the response of soil to pure hydrostatic stress. Typical response for a real soil is shown in Fig. 4, where void ratio is plotted versus the natural logarithm of the negative of the hydrostatic stress (p is of course negative here). If the current pressure, denoted by point A, is the greatest the soil has experienced, then upon application of increased pressure the soil will load along line AB. If the pressure is then decreased, the soil will unload along curve BC and upon further application of pressure will reload along curve CD. If we continue to apply pressure, the response curve tends to approach asymptotically line ABE (virgin isotropic consolidation line).

An idealized version of this response is pictured in Fig. 5. The virgin isotropic consolidation line is assumed to be linear. The rebound and reloading curves are assumed to be identical and linear, and all rebound-reloading curves are parallel. Thus the equation for the virgin isotropic consolidation line is

$$e_v = e_{v1} - \Lambda \, \mathrm{Ln}(-p) \tag{27}$$

where e_v is soil void ratio, the natural logarithm (logarithm to the base e) is denoted by Ln, and e_{v1} and Λ are material constants. A generic rebound-reloading curve is defined by

$$e_v = e_{v2} - \eta \, \mathrm{Ln}(-p) \tag{28}$$

where η is a material constant, and e_{v2} defines a particular rebound-reloading curve.

Referring still to Fig. 5, consider an infinitesimal increment of loading from A to B followed by unloading from B to C. From Eq. 27, the void ratio change from A to B is

$$\dot{e}_v = - \Lambda \frac{\dot{p}}{p} \tag{29}$$

where p is the current hydrostatic stress and $\dot{p}$ is the increment of hydrostatic stress (stress rate), and, from Eq. 28, the void ratio recovered when unloading from B to C is

$$\dot{e}_v = - \eta \, \dot{p}/p \tag{30}$$

Now

$$\dot{e}_{ii} = \frac{\dot{e}_v}{1 + e_v} \tag{31}$$

where

$$\dot{e}_{ii} = \dot{e}_{11} + \dot{e}_{22} + \dot{e}_{33} \tag{32}$$

and in the context of the theory of plasticity, the recoverable or elastic component of the volumetric strain is

$$\dot{e}^{e}_{ii} = - \frac{\eta \, \dot{p}}{(1 + e_v) \, p} \tag{33}$$

while, from Eqs. 29 and 30, the plastic or irrecoverable component of the volumetric strain is

$$\dot{e}^{p}_{ii} = - \frac{(\Lambda - \eta)\ \dot{p}}{(1 + e_v)\ p} \tag{34}$$

since

$$\dot{e}^{p}_{ii} = \dot{e}_{ii} - \dot{e}^{e}_{ii} \tag{35}$$

The State Boundary Surface and the Critical State Line

Although the Cambridge models were originally formulated in order to describe the behavior of soil in the triaxial test, we are concerned here with general states of stress and will hence use general stress invariants rather than those peculiar to the triaxial test. It is postulated that there exists a unique "state boundary surface" in a three-dimensional space of hydrostatic stress p, J_2, and void ratio e_v. A point in this space is referred to as a state point, and the state boundary surface is said to delimit admissible and inadmissible state points.

A portion of the state boundary surface is shown in Fig. 6. State points below the state boundary are admissible, while those points above the surface are inadmissible. A continuous sequence of state points is referred to as a state path. From the point of view of the theory of plasticity, state paths which lie below the state boundary surface are associated with elastic behavior, while those which lie on the state boundary surface are associated with strain hardening.

It is further postulated that there exists on the state

boundary surface a "critical state line" where unlimited distortional strain may occur with no corresponding change in the stress state or the void ratio.

Consider now a soil specimen stressed uniformly (for example in the triaxial test). We load the soil until failure and plot the results in state space. Referring to Fig. 6, curve HIJK corresponds to the state path of the soil. We assume that the initial state point (denoted by point H) lies below the state boundary surface. Thus the initial portion of the state path, HI, corresponds to elastic behavior. At point I the state path intersects the state boundary surface and at point K failure occurs. State path IJK lies on the state boundary surface and is thus associated with strain hardening, while point K lies on the critical state line.

As the soil strain hardens the stress state passes through a sequence of yield surfaces until failure is reached at the critical state line. These yield curves can be uniquely represented in $p - J_2$ space. For example the initial yield curve is curve CID on the state boundary surface and is also denoted by curve CID in Fig. 7 where the stress path is also shown. Curve EJF, shown in Figs. 6 and 7 corresponds to a subsequent yield curve.

The reader should recall that we have assumed that elastic distortional strain is identically zero and that elastic volumetric strain is independent of deviatoric stresses. Thus if we apply a deviatoric stress increment to the soil sample in its initial state (point H in Fig. 5), the void ratio remains unchanged and the state

path corresponds to a vertical line. If we apply a hydrostatic stress increment the state path must be defined by Eq. 28. We say then that state path HI lies in a so-called vertical "elastic wall". The elastic wall intersects the $J_2 = 0$ plane along a rebound-reloading curve and intersects the state boundary surface along a yield curve. Each yield curve is thus associated with a particular isotropic rebound-reloading curve.

Modified Cam-Clay Yield Surface

A modified Cam-clay yield surface and the projection of the critical state line in $p - J_2$ space are shown in Fig. 8. The yield curve is elliptical and is defined by

$$f = p^2 - p_o\, p + \frac{J_2}{M^2} = 0 \tag{36}$$

where M is a material constant and p_o is a strain hardening parameter. The critical state line intersects the ellipse at its maximum point and is defined by

$$J_2^{1/2} = - M\, p \tag{37}$$

that is, the critical stress state is defined by an extended von Mises type expression.

The stress-strain model will be completely defined once we have specified the relationship between the strain hardening parameter and the strains. Consider now an infinitesimal stress increment denoted by line AB in Fig. 8. Point A lies on the current yield curve while point B lies on the subsequent yield curve. Associated

with the current yield curve is an elastic wall and an isotropic rebound-reloading curve, and, of course, there is also an elastic wall and a rebound-reloading curve associated with the subsequent yield curve.

Referring to Figs. 6 and 7, the current value of the strain hardening parameter is defined by the intersection of the current isotropic rebound-reloading curve and the isotropic virgin consolidation curve. Both the current and subsequent isotropic rebound-reloading curves are shown in Fig. 9 along with the projection of the incremental state path on to e_v - Ln(- p) space. If we now allow the soil sample to unload, the unloading state path lies in an elastic wall and its projection is denoted by BC in Fig. 9. Recalling Eq. 34 it is clear that we can relate the plastic volumetric strain and the change in the strain hardening parameter as follows,

$$\dot{e}^p_{ii} = - \frac{(\Lambda - \eta)\ \dot{p}_o}{(1 + e_v)\ p_o} \tag{38}$$

or

$$\dot{p}_o = - \frac{1 + e_v}{\Lambda - \eta}\ p_o\ \dot{e}^p_{ii} \tag{39}$$

Behavior of Modified Cam-Clay in the Triaxial Test

We consider now a hypothetical drained triaxial test on modified Cam-clay. The test sample is first subjected to an all around confining pressure sufficient to cause plastic yielding. Thus after applying the pressure the value of the strain hardening parameter, p_o, is identical to the applied pressure. The pressure is then reduced to some value denoted by p_1. The specimen is

subsequently strained axially while the confining pressure is held constant.

The stress path is denoted by line ABCD in Fig. 10. The specimen yields at point B and strain hardening begins. At points B, C and D we have superimposed on the stress space a plastic strain rate vector. The horizontal component of the strain rate vector corresponds to volumetric strain while the vertical component corresponds to distortional strain. We use the associated flow fule here and hence the plastic strain rate vector is normal to the yield surface.

At point B the plastic component of the volumetric strain is decreasing, and thus the load increases as we continue to strain the body. We see from Eq. 39 that a decrease in the plastic volumetric strain is associated with an expanding yield surface. As we continue to strain the body further, the sample volume continues to decrease so that strain hardening continues. However, as the critical state line is approached the rate of the plastic volumetric strain decreases until at the critical state the plastic volumetric strain is identically zero, as indicated by the vertical strain rate vector at point D. Hence as we continue to strain the sample the vertical load remains constant and we have thus reached the failure condition. If we were to plot the axial stress versus axial strain, the curve would resemble that shown in Fig. 2a.

We should emphasize that the function which defines failure is not a yield curve nor is it the limit of a sequence of yield curves. In addition, although the Drucker-Prager model and the modified

Cam-clay model incorporate similar failure functions, the former predicts dilation at failure while the latter predicts zero dilation at failure.

Although the modified Cam-clay model was developed in order to predict the strain hardening behavior of clay, the model will in fact predict strain softening for certain stress histories. We consider now the same type of test as described previously in which an initial hydrostatic stress(p_o) is applied and subsequently reduced to a value denoted by p_1. In this case p_1 is considerably less than p_o as indicated in Fig. 11.

Referring to Fig. 11, as the test specimen is strained axially plastic yielding first occurs at point B. However here the plastic volumetric strain is positive and the specimen begins to strain soften with the axial load reducing. From Eq. 39 we see that an increase in the plastic volumetric strain is associated with a contracting yield surface. The specimen continues to strain soften until point C is reached where the plastic volumetric strain rate is identically zero. Continued axial straining produces no change in the axial load.

The peak stress is no longer defined by an extended von Mises expression but is rather dependent on the maximum past hydrostatic stress. It is the residual stress that is defined by the extended von Mises expression. The test specimen dilates at the peak stress whereas at the residual stress no dilation occurs.

We might refer to the first specimen as lightly overconsolidated and the second specimen as heavily overconsolidated. The lightly overconsolidated specimen strain hardened when sheared while the heavily overconsolidated specimen strain softened when sheared.

Incremental Stress-Strain Equations Suitable for Numerical Analysis

Although modified Cam-clay is suitable for predicting the response of soil in the triaxial test, it is not suitable for general stress analysis. Since the model is rigid-plastic with respect to shearing deformation, the function we require in a displacement formulation, stress as a function of strain, is singular. The possibility of strain softening is also a problem. Any numerical approach which requires inversion of the tangent stiffness may break down in the presence of strain softening. In addition the solution of boundary value problems involving strain softening materials is not yet well defined. In general it can not be shown that such solutions are unique. We thus present a variant of the modified Cam-clay model which is suitable for a tangent stiffness formulation.

Considering first elastic response, from Eq. 33, we have

$$\dot{e}^e_{ii} = - \frac{\eta}{1 + e_v} \frac{\dot{p}}{p} \tag{40}$$

If elastic distortional strain is identically zero, the elastic strain rate-stress rate equation is

$$\dot{e}^e_{ij} = - \frac{\eta}{9(1 + e_v)\, p} \dot{\sigma}_{kk}\, \delta_{ij} \tag{41}$$

In order to invert Eq. 41 we introduce some distortional flexibility as follows,

$$\dot{e}^e_{ij} = - \left[\frac{\eta}{9(1 + e_v)\, p} + \frac{1}{3\beta} \right] \dot{\sigma}_{kk}\, \delta_{ij} + \frac{1}{\beta} \dot{\sigma}_{ij} \tag{42}$$

where β is the instantaneous elastic shear modulus of the soil. Equation 40 is still valid. Finally, Eq. 42 can be inverted to give,

$$\dot{\sigma}_{ij} = -\left[\frac{p(1 + e_v)}{\eta} + \frac{\beta}{3}\right] \dot{e}^e_{kk}\, \delta_{ij} + \beta\, \dot{e}^e_{ij} \tag{43}$$

If we desire to keep the computational model as close as possible to modified Cam-clay, the shear modulus, β, can be made quite large, perhaps one hundred times the plastic bulk modulus.

In order to determine the elastic-plastic, incremental stress-strain relations, we again start with the associated flow rule after Drucker and write

$$\dot{e}^p_{ij} = \lambda \frac{\partial f}{\partial \sigma_{ij}} \tag{44}$$

where

$$f(\sigma_{ij}, p_o) = p^2 - p_o\, p + \frac{J_2}{M^2} \tag{45}$$

Noting that

$$\dot{e}^e_{ij} = \dot{e}_{ij} - \dot{e}^p_{ij} \tag{46}$$

We rewrite Eq. 43 as

$$\dot{\sigma}_{ij} = -\left[\frac{p(1 + e_v)}{\eta} + \frac{\beta}{3}\right] \left(\dot{e}_{kk} - \lambda \frac{\partial f}{\partial \sigma_{kk}}\right) \delta_{ij} + \beta\left(\dot{e}_{ij} - \lambda \frac{\partial f}{\partial \sigma_{ij}}\right) \tag{47}$$

The problem again is to determine λ, and we note that during plastic loading the stress state and the strain hardening parameter change such that the new stress state lies on the subsequent yield surface defined by the new value of the strain hardening parameter. At the beginning of the increment,

$$f(\sigma_{ij}, p_o) = 0 \tag{48}$$

and at the end of the increment,

$$f(\sigma_{ij} + \dot{\sigma}_{ij}, p_o + \dot{p}_o) = 0 \tag{49}$$

Thus

$$df = \frac{\partial f}{\partial \sigma_{ij}} \dot{\sigma}_{ij} + \frac{\partial f}{\partial p_o} \dot{p}_o = 0 \tag{50}$$

Equations 47 and 50 permit the determination of λ.

Now, from Eq. 45,

$$\frac{\partial f}{\partial \sigma_{ij}} = \frac{1}{3} (2p - p_o) \delta_{ij} + \frac{s_{ij}}{M^2} \tag{51}$$

and

$$\frac{\partial f}{\partial p_o} = - p \tag{52}$$

Also, repeating Eq. 39

$$\dot{p}_o = - \frac{1 + e_v}{\Lambda - \eta} p_o \dot{e}^p_{kk} = - \frac{1 + e_v}{\Lambda - \eta} p_o \lambda \frac{\partial f}{\partial \sigma_{kk}} \tag{53}$$

Utilizing Eqs. 51, 52 and 53 and substituting Eq. 47 into Eq. 50 gives

$$df = \left\{\frac{(2p - p_o)}{3} \delta_{ij} + \frac{s_{ij}}{M^2}\right\} \left\{\beta\left[\dot{e}_{ij} - \lambda\left(\frac{(2p - p_o)}{3} \delta_{ij} + \frac{s_{ij}}{M^2}\right)\right]\right.$$
$$\left. - L\left[\dot{e}_{kk} - \lambda (2p - p_o)\right] \delta_{ij}\right\} - p R \lambda (2p - p_o) \tag{54}$$

where,

$$L = p \frac{(1 + e_v)}{\eta} + \frac{\beta}{3} \tag{55}$$

and

$$R = - p_o \left(\frac{1 + e_v}{\Lambda - \eta}\right) \tag{56}$$

Simplifying Eq. 54 and solving for λ gives,

$$\lambda = \frac{\frac{\beta s_{ij}}{M^2}\dot{e}_{ij} + H\,\dot{e}_{kk}}{(2p - p_o)\,H + \frac{2\beta J_2}{M^4} + p\,(2p - p_o)\,R} \tag{57}$$

where

$$H = (2p - p_o)\left(\frac{\beta}{3} - L\right) \tag{58}$$

Finally, substituting Eq. 57 into Eq. 47 yields the incremental elastic-plastic stress-strain relationship

$$\dot{\sigma}_{ij} = \beta\,\dot{e}_{ij} - L\,\dot{e}_{mm}\,\delta_{ij} - \frac{1}{\psi}\left(H\,\delta_{ij} + \frac{\beta}{M^2}\,s_{ij}\right)\left(\frac{\beta}{M^2}\,s_{k\ell}\,\dot{e}_{k\ell} + H\,\dot{e}_{mm}\right) \tag{59}$$

where

$$\psi = (2p - p_o)\,H + \frac{2\beta J_2}{M^4} + p\,(2p - p_o)\,R \tag{60}$$

Equation 59 is applicable in both the strain hardening and strain softening regions and is, of course, applicable at the critical state. If $p \leq p_o/2$ the model is either strain hardening or at the critical state and Eq. 59 is suitable for the numerical formulation used here. If $p > p_o/2$ the model is strain softening and hence would not be suitable for application here.

In order to get around this problem we could introduce a perfectly plastic idealization in the strain softening region which would be compatible with the modified Cam-clay model. For instance we might use the critical state line as a perfectly plastic yield surface. A simpler approach would utilize the current value of the modified Cam-clay yield surface as a perfectly-plastic yield surface. The stress-strain equations would still be defined by Eq. 59, however,

ψ would now be defined by

$$\psi = (2p - p_o)\ H + \frac{2\beta J_2}{M^4} \tag{61}$$

If we utilized Eq. 59 for the incremental stress-strain equation and define ψ by Eq. 60 for $p \leq p_o/2$ and by Eq. 61 for $p > p_o/2$, we have then a complete stress-strain model suitable for use in a tangent stiffness approach. This model has one potential drawback, that is, if the hydrostatic stress component is zero, the incremental stress-strain equations are singular. This may be troublesome for some boundary value problems. To avoid this problem, Zienkiewicz and Naylor (83) have suggested using a model which is linear in the elastic region.

Boundary Value Problems and the Cambridge Soil Models

Smith (67) has used the so-called Cam-clay model to analyze the plane strain, drained behavior of a pressurized thick cylinder of clay. Smith and Kay (68) analyzed the same problem using modified Cam-clay as well as Cam-clay. In both papers elastic strains were assumed to be identically zero. Zienkiewicz and Naylor (82) have analyzed the drained behavior of modified Cam-clay in the triaxial test. Some elastic distortional flexibility was introduced into the model.

Zienkiewicz and Naylor (83) have considered a clay layer consolidating under a footing load. The soil skeleton was modeled by a variant of modified Cam-clay. Elastic behavior was assumed to be linear and in the strain hardening region a modified Cam-clay

yield curve was used. In the strain softening region a softening Mohr-Coulomb type expression with a nonassociated flow rule was utilized.

3. INCREMENTAL EQUILIBRIUM EQUATIONS

3.1 Preliminaries

The purpose of this chapter is to develop the governing differential equations by introducing the preceeding stress-strain relations into equilibrium equations which reflect the changing geometry of the soil stratum. We assume that the magnitude of the deformations is such that geometric changes caused by deformation must be considered when writing the equilibrium equations.

Herein, we formulate a set of equilibrium equations (in virtual work form)for a small increment of deformation superimposed on an already deformed and stressed body (initial configuration). Our final objective is to determine the tangent stiffness of the body, with due consideration given to large deformations.

We note to begin with that the equations of continuum mechanics can be posed in Eulerian or Lagrangian form. Briefly, in a Lagrangian formulation all quantities (e.g., stress and strain) are referred to coordinates associated with some reference configuration, perhaps the undeformed condiguration of the body. In an Eulerian formulation all quantities are referred to coordinates associated with the current configuration of the body. Lagrangian and Eulerian coordinates are sometimes referred to as material and spatial coordinates respectively.

We differentiate now between a Lagrangian incremental formulation, an Eulerian incremental formulation and a mixed incremental

formulation. Both the Lagrangian and mixed incremental equations employ a known material reference state. The reference state used in the Lagrangian incremental approach is the same for all increments and is usually the undeformed, unstressed state of the body. The reference state employed in the mixed formulation is the current spatial configuration of the body, that is, the current Eulerian coordinates of the body, and this reference state is updated following each incremental step. A pure Eulerian incremental formulation, obtained by taking the first variation of the nonlinear Eulerian equations, has also been presented in the literature. A mixed incremental formulation will be utilized here.

3.2 Some Previous Finite Element Work

Incremental approaches to geometrically nonlinear structural problems have appeared in the finite element literature since 1960. However, the mechanics of incremental deformations was a subject of interest considerably before this time. Linearized mechanics of an initially stressed body was discussed by Biot (5)(6). Biot (7) presented a comprehensive treatment of the subject. In the context of an incremental approach to nonlinear problems, Biot's formulation is mixed.

Turner, Dill, Martin, and Melosh (72) introduced the incremental finite element approach to the solution of geometrically nonlinear structures. A somewhat long derivation leads to a stiffness matrix for a plate element which includes the infinitesimal stiffness matrix and so-called geometric or initial stress stiffness matrix.

The incremental equilibrium equations are meaningful when used properly in the context of a mixed incremental approach, as this term is defined here. Strains are assumed to be small.

Martin (44) introduced the Green strain tensor into an incremental formulation of the small strain, large rotation problem. The stiffness matrix so developed can be used in a consistent mixed approach in the following two ways. If one takes the initial stress as the Kirchhoff stress (accumulated from the undeformed configuration), the stiffness matrix is referred correctly to a local coordinate system which has followed the element rotation. This would be the natural way to handle beam-column problems. One might alternately take initial stresses in the global system, and the incremental stiffness matrix will hence also be referred to the global system.

Wissmann (75) presented a Lagrangian, tensor formulation for bodies suffering large rotations but small strains. A set of Lagrangian incremental equations was obtained through a linear Taylor expansion of the nonlinear equations about a stressed, deformed configuration.

Felippa (25) introduced a virtual work equation for initially stressed bodies. The incremental approach is mixed and, as indicated by Fernandez and Christian (26), may only be strictly applicable to the small strain, large rotation problem. It appears that Felippa (25) was the first to combine both material and geometric nonlinearities, solving a plastic buckling problem.

In a manner similar to Wissmann (75), Mallett and Marcal (40) developed Lagrangian incremental equations for linear elastic structures suffering large rotations. The so-called initial displacement matrix, unique to the Lagrangian incremental approach, was discussed in some detail. Marcal (42) used a virtual work approach to formulate Lagrangian incremental equations for the elastic-plastic, large rotation problem.

Yaghmai (77) presented an in-depth study of incremental virtual work formulations of the large strain, large rotation problem. Both Lagrangian and mixed incremental approaches were considered and the mixed formulation was applied to shells of revolution.

Lagrangian incremental formulations for problems involving large strains as well as large rotations were presented by Hartz and Nathan (32), Oden (50) and Hibbitt, Marcal and Rice (33). Hartz and Nathan considered hyperelastic materials and obtained incremental equations through a Taylor expansion of the nonlinear equations. A hierarchy of nonlinear theories was presented in the manner of Novozhilov (49). Oden developed incremental equations by considering a small perturbation about a known configuration. Hibbitt, Marcal and Rice used virtual work to formulate incremental equations. A rationally developed incremental elastic-plastic constitution law relating Kirchhoff stress and Green strain was presented in the paper.

Hofmeister, Greenbaum and Evensen (36) presented a mixed incremental formulation for the elastic-plastic, large strain, large rotation problem. A modified version of the incremental equations,

accounting for nonequilibrium of the initial stress state, was discussed. A similar modification for a small strain Lagrangian formulation was proposed by Strickland, Haisler and Von Riesemann (69). They demonstrated through numerical example the superiority of the modified incremental approach as compared to the conventional incremental approach.

Dupuis, Hibbitt, McNamara, and Marcal (24) and Zienkiewicz and Nayak (80) presented parallel Lagrangian and Eulerian incremental formulations. The finite element concept was used explicitly in the derivations of both papers, and the incremental equations were obtained by taking the first variation of the nonlinear equations. Dupuis et al assumed strains to be small, while Zienkiewicz and Nayak consider large strains. In addition Zienkiewicz and Nayak discussed a large strain, elastic-plastic formulation.

Finally, Fernandez and Christian (26) considered the effect of large deformations on some soil mechanics problems using the incremental approach of Biot (7).

The bibliography presented here represents only a small part of the finite element literature on geometric nonlinearities. A good overview of the subject is presented by Oden (50), and an informative comparison of solution techniques is presented by Haisler, Strickland and Stebbins (31). Additional references can be found in Gallagher (28) and Oden (51).

3.3 Mixed Incremental Formulation

When presenting an incremental formulation, one must first of all be careful to differentiate between Eulerian, Lagrangian and mixed approaches. Secondly, in the context of large rotations and deformations, "stress" and "strain" must be precisely defined. Finally, an incremental formulation is not complete until one has described fully the procedures for progressing from increment to increment.

We make no a priori assumptions concerning the magnitude of rotations or strains. However, the equations governing incremental deformation are predicated upon the assumption that incremental strains are an order of magnitude smaller than incremental rotations. The large strain phenomenon is captured by updating the geometry at the end of each increment.

A brief word concerning the notation used in this chapter is appropriate here. We use indicial notation and the associated summation convention. Any term containing a repeated index is to be summed over that index (from 1 to 3). A comma followed by a subscript indicates a partial derivative with respect to current material coordinates.

To formulate the equations governing an increment of deformation we consider two different configurations of the body, an initial configuration and a subsequent configuration. The stresses, strains and displacements in the initial configuration are presumed known and have been determined through a sequence of incremental steps.

We note that due to the approximate nature of the analysis, the initial stresses probably do not satisfy identically the equations of equilibrium. The subsequent configuration is reached through a further increment of deformation, and it is the incremental stresses, strains and displacements that we wish to determine.

Equations of equilibrium for the subsequent configuration are written in terms of the geometry of the initial configuration. We can say that we use a Lagrangian formulation to prescribe equilibrium of the subsequent configuration where the material coordinates are the coordinates of the body in the initial configuration. Initial stresses are referred to a global reference frame, and the initial geometry is a deformed geometry determined by previous increments.

Before beginning the analysis, it might be helpful to introduce some of the terminology to be used here. We will refer to three different stress tensors:

σ_{ij} - Initial Cartesian stress tensor referred to a global reference frame. It is to be clearly understood that these are physical stress components representing force per unit of area of the initial geometry. This tensor is called Euler's stress tensor in the engineering mechanics literature. In addition $\bar{\sigma}_{ij}$ is the Eulerian stress tensor in the subsequent configuration.

τ_{ij} - A Cartesian stress tensor in the subsequent configuration. The stress components are referred to a locally rotated Cartesian frame which varies from point to point. These

are physical stress components, that is, force per unit of area of the subsequent geometry.

S_{ij} - Kirchhoffs stress tensor (27). This tensor will be formally defined later, it being noted however that Kirchhoff's stress tensor describes the stress state in the subsequent configuration as referred to the geometry of the initial configuration. These are not physical stress components as defined above.

We will also refer to two different strain tensors. Green's strain tensor (27) is defined as

$$\epsilon_{ij} = \frac{1}{2} (u_{i,j} + u_{j,i} + u_{k,i}\, u_{k,j}) \tag{62}$$

and the infinitesimal strain tensor is

$$e_{ij} = \frac{1}{2} (u_{i,j} + u_{j,i}) \tag{63}$$

where u_i is the incremental displacement vector.

Consider now a body situated in a fixed Cartesian reference frame (X,Y,Z). Referring to Fig. 12, let s denote the boundary surface of the body in its initial configuration and s' denote the boundary in the subsequent configuration. Let (x_1,x_2,x_3) be the initial Cartesian coordinates of a generic point in the body, and let (ξ_1, ξ_2,ξ_3) be the Cartesian coordinates of the same point after an increment of deformation. We write

$$\xi_i = x_i + u_i \tag{64}$$

Equilibrium of the initial state is implied by the virtual work expression

$$\int_s T_i \, \delta u_i \, ds + \int_v \rho_o \, F_i(x) \, \delta u_i \, dv = \int_v \sigma_{ij} \, \delta e_{ij} \, dv \tag{65}$$

where T_i is the boundary traction vector per unit of initial area, $F_i(x)$ is the body force vector per unit mass and ρ_o is the mass density of the initial configuration. It is assumed here that body force is purely a function of position in the fixed reference frame. The virtual displacement field is denoted by δu_i and is identically zero where displacements are prescribed. Also

$$\delta e_{ij} = \frac{1}{2} \left\{ (\delta u_i)_{,j} + (\delta u_j)_{,i} \right\} \tag{66}$$

where we note for the sake of clarity that

$$(\delta u_i)_{,j} = \frac{\partial (\delta u_i)}{\partial x_j} \tag{67}$$

We now consider equilibrium of the subsequent configuration. The Kirchhoff stress tensor in the subsequent configuration is denoted by S_{ij} and is defined as (27),

$$S_{ij} = \frac{\rho_o}{\rho} \frac{\partial x_i}{\partial \xi_k} \frac{\partial x_j}{\partial \xi_\ell} \bar{\sigma}_{k\ell} \tag{68}$$

where ρ is mass density in the subsequent configuration and $\bar{\sigma}_{k\ell}$ is the Eulerian stress tensor in the subsequent configuration. We note that S_{ij} is symmetric.

Remembering that the equation of equilibrium of the subsequent configuration is to be written in terms of the geometry of the initial

configuration, we note that the internal virtual work per unit of initial volume is the product of Kirchhoff's stress tensor and the variation of Green's strain tensor (49), that is,

$$\delta W_i = \int_v S_{ij}\, \delta\epsilon_{ij}\, dv \tag{69}$$

Equilibrium of the subsequent configuration is then implied by the virtual work expression

$$\int_s (T_i + \Delta T_i)\, \delta u_i\, ds + \int_v \rho_o\, F_i(\xi)\, \delta u_i\, dv = \int_v S_{ij}\, \delta\epsilon_{ij}\, dv \tag{70}$$

where ΔT_i is the incremental surface traction vector per unit of initial area. We note that the simplicity of the incremental traction vector shown here hides a more complex phenomenon in which ΔT_i may be a function of incremental boundary displacements as well as incremental boundary forces (51)(33). Since surface tractions are not of primary concern here, we retain this simplified representation.

We write now,

$$S_{ij} = \sigma_{ij} + \Delta S_{ij} \tag{71}$$

and call ΔS_{ij} the incremental Kirchhoff stress tensor. Substituting Eq. 71 into Eq. 70 and noting that

$$\delta\epsilon_{ij} = \delta e_{ij} + \frac{1}{2}\{u_{k,i}\, (\delta u_k)_{,j} + u_{k,j}\, (\delta u_k)_{,i}\} \tag{72}$$

we obtain

$$\int_s \Delta T_i\, \delta u_i\, ds + \int_v \rho_o\, \Delta F_i\, \delta u_i\, dv + \{\int_s T_i\, \delta u_i\, ds + \int_v \rho_o\, F_i(x)\, \delta u_i\, dv$$

$$- \int_v \sigma_{ij}\, \delta e_{ij}\, dv\} = \int_v \sigma_{ij}\, \frac{1}{2}\{u_{k,i}\, (\delta u_k)_{,j} + u_{k,j}\, (\delta u_k)_{,i}\}\, dv$$

$$+ \int_v \Delta S_{ij} \, \delta\epsilon_{ij} \, dv \tag{73}$$

$$\text{where } \Delta F_i = F_i(\xi) - F_i(x) \tag{74}$$

Regarding Eq. 73, we note, first of all, that the left hand side of the equation is devoid of unknown incremental quantities. Secondly, the expression in braces on the left-hand side of the equation would be identically zero if the initial stress distribution satisfied the equation of equilibrium (Eq. 65). However, recognizing the approximate nature of the analysis, we retain this expression as per Hofmeister, Greenbaum and Evensen (36). If one could find incremental stress and displacement distributions satisfying Eq. 73 for all kinematically admissible virtual displacements, the subsequent configuration would be in a state of equilibrium.

3.4 Two Sets of Linearized Incremental Equations

To this point no approximating assumptions have been made. Equation 73 is an exact statement of the equilibrium of the subsequent configuration. In what follows two linearized versions of the incremental equilibrium equations are presented. We linearize first without making any assumptions concerning the relative magnitudes of strains and rotations and find the resultant equations to be asymmetric. By assuming the order of magnitude of the incremental strains is less than that of the incremental rotations, we are led to a second set of linear incremental equilibrium equations which are symmetric.

To begin with we note that in the context of small displacements, our elastic-plastic constitutive law relates physical Cartesian

stress rate to the infinitesimal strain rate. In the context of a large strain, large rotation analysis, care must be taken to relate the proper stress increment to the proper strain increment. Consider now the initial Eulerian stress tensor for a two-dimensional body as depicted in Fig. 13. During an increment of deformation, the neighborhood of a generic point translates, rotates and deforms, where to the first order the rotation is defined by

$$\omega = \frac{1}{2}\left\{\frac{\partial u_2}{\partial x_1} - \frac{\partial u_1}{\partial x_2}\right\} \tag{75}$$

Physical stresses in the subsequent configuration, referred to a local coordinate system rotated an amount ω from the fixed reference frame, are depicted in Fig. 14. We write

$$\tau_{ij} = \sigma_{ij} + \Delta\tau_{ij} \tag{76}$$

It is clear that if the neighborhood of the generic point suffers rotation but no deformation, then

$$\Delta\tau_{ij} = 0 \tag{77a}$$

and

$$\tau_{ij} = \sigma_{ij} \tag{77b}$$

We thus propose to use the elastic-plastic constitutive law developed in Chap. 2 in the following manner,

$$\Delta\tau_{ij} = D_{ijk\ell}\, e_{k\ell} \tag{78}$$

We show in Appendix I that the incremental Kirchhoff stress tensor is related to $\Delta\tau_{ij}$, to the first order, in the following manner (2 - D plane strain),

$$\begin{Bmatrix} \Delta S_{11} \\ \Delta S_{22} \\ \Delta S_{12} \end{Bmatrix} = \begin{Bmatrix} \Delta \tau_{11} \\ \Delta \tau_{22} \\ \Delta \tau_{12} \end{Bmatrix} + \begin{bmatrix} -\sigma_{11} & \sigma_{11} & -2\sigma_{12} \\ \sigma_{22} & -\sigma_{22} & -2\sigma_{12} \\ 0 & 0 & -(\sigma_{11}+\sigma_{22}) \end{bmatrix} \begin{Bmatrix} e_{11} \\ e_{22} \\ e_{12} \end{Bmatrix} \tag{79}$$

Writing the above expression in indicial notation, we have

$$\Delta S_{ij} = \Delta \tau_{ij} + \Psi_{ijpq}\, e_{pq} \tag{80}$$

Substituting Eq. 80 into Eq. 73, rearranging some terms and eliminating products of incremental quantities, we obtain the following linear incremental equilibrium equation

$$\begin{aligned} &\int_s (T_i + \Delta T_i)\, \delta u_i\, ds + \int_v \rho_o\, F_i(\xi)\, \delta u_i\, dv - \int_v \sigma_{ij}\, \delta e_{ij}\, dv \\ &= \int_v \sigma_{ij}\, u_{k,i}\, (\delta u_k)_{,j}\, dv + \int_v (\Delta \tau_{ij} + \Psi_{ijpq}\, e_{pq})\, \delta e_{ij}\, dv \end{aligned} \tag{81}$$

Considering the Ψ matrix defined by Eq. 79, one can readily show that the differential equilibrium equations associated with the virtual work expression (Eq. 81) are identical to the two-dimensional incremental equations developed by Biot (7).

An interesting feature of Eq. 81 is the asymmetry of matrix Ψ. If a finite element expansion is employed in conjunction with virtual work Eq. 81, the asymmetry of the Ψ matrix will cause the set of discrete equilibrium equations to be also asymmetric. Although the solution of asymmetric sets of linear simultaneous equations presents no conceptual difficulties, there are some practical drawbacks involved in such solutions. Considering for the moment direct solution algorithms as coded for a digital computer, core storage required for the equations is approximately twice that needed

for a symmetric set, and the time required to solve the equations is also about twice that needed for a symmetric set. With these penalties in mind we return to our original incremental equilibrium equations to examine the possibility of eliminating asymmetric terms. In what follows we do exactly this using a physical argument concerning relative magnitudes of incremental quantities.

To linearize the incremental equilibrium equations, we made the implicit assumption that incremental deformations and rotations are "small". One consequence of assuming incremental deformations to be small is that relative elongations and shears (as defined by Novozhilov (49)) are given by Green's strain tensor (Eq. 62). If we further assume that incremental deformations (ϵ_{ij}) are an order of magnitude less than incremental rotations ($\omega_{ij} = \frac{1}{2}(u_{j,i} - u_{i,j})$), the linear incremental equations are rendered symmetric.

Noting the following identity,

$$u_{i,j} = e_{ij} - \omega_{ij} \tag{82}$$

and incorporating the identity in Green's strain tensor yields

$$\epsilon_{ij} = e_{ij} + \frac{1}{2}(e_{ki} - \omega_{ki})(e_{kj} - \omega_{kj}) \tag{83a}$$

or

$$\epsilon_{ij} = e_{ij} + \frac{1}{2}(e_{ki}\, e_{kj} - e_{ki}\, \omega_{kj} - \omega_{ki}\, e_{kj} + \omega_{ki}\, \omega_{kj}) \tag{83b}$$

Clearly Green's strain tensor and the infinitesimal strain tensor (e_{ij}) are of the same order of magnitude, and hence the infinitesimal strain tensor is also of a lesser order of magnitude than the rotation tensor. With this in mind we eliminate products of infinitesimal

strain components to obtain the following approximate expression.

$$\epsilon_{ij} \approx e_{ij} + \frac{1}{2} (- e_{ki}\, \omega_{kj} - \omega_{ki}\, e_{kj} + \omega_{ki}\, \omega_{kj}) \tag{84}$$

Considering again Eq. 80 and recalling our assumption that incremental deformations are very small, we also incorporate the following approximation as per Novozhilov (49),

$$\Delta S_{ij} \approx \Delta \tau_{ij} \tag{85}$$

and eliminate the asymmetric part of the incremental equations. Our new incremental equilibrium equation is then,

$$\int_s (T_i + \Delta T_i)\, \delta u_i\, ds + \int_v \rho_o\, F_i(\xi)\, \delta u_i\, dv - \int_v \sigma_{ij}\, \delta e_{ij}\, dv$$

$$= \int_v \sigma_{ij} (- e_{ki}\, \delta\omega_{kj} - \omega_{ki}\, \delta e_{kj} + \omega_{ki}\, \delta\omega_{kj})\, dv + \int_v \Delta\tau_{ij}\, \delta e_{ij}\, dv \tag{86}$$

It is to be understood that we do not claim that soil response is characterized by small deformation and large rotation. We have merely shown that assuming incremental deformations to be smaller than incremental rotations leads us to a set of symmetric equations. To reiterate, it is still our intention to capture large deformations as well as large rotations.

Although Eq. 81 is itself an approximate equation governing incremental response, it more accurately describes the response of the body than does Eq. 86. However, the symmetry characteristics of Eq. 86 recommend it. If one chooses to use Eq. 86, then a greater number of increments must be employed as compared to using Eq. 81. The choice is not clear however since a greater computational effort

is required per increment if the asymmetric equations are employed.

Actually, the choice we make here is governed by other factors. Although the soil response we attempt to predict here is highly nonlinear, material nonlinearities dominate geometric nonlinearities. Increment size will be governed by the severity of the material nonlinearities and hence even a relatively crude approximation can capture the geometric nonlinearities. With this in mind we use here the symmetric incremental equilibrium equation, Eq. 86.

3.5 Incremental Finite Element Equations

We first recast Eq. 86 in matrix form for the two-dimensional plane strain problem. Some matrix definitions follow:

$$\{U\} = \begin{Bmatrix} u_1 \\ u_2 \end{Bmatrix} \tag{87a}$$

$$\{T\} = \begin{Bmatrix} T_1 \\ T_2 \end{Bmatrix} \tag{87b}$$

$$\{F\} = \begin{Bmatrix} F_1 \\ F_2 \end{Bmatrix} \tag{87c}$$

$$\{\tau\} = \begin{Bmatrix} \tau_{11} \\ \tau_{22} \\ \tau_{12} \end{Bmatrix} \tag{87d}$$

$$\{e\} = \begin{Bmatrix} e_{11} \\ e_{22} \\ \gamma_{12} \end{Bmatrix} \tag{87e}$$

$$\{\tilde{e}\} = \begin{Bmatrix} e_{11} \\ e_{22} \\ \gamma_{12} \\ \omega \end{Bmatrix} \tag{87f}$$

$$\{\sigma\} = \begin{Bmatrix} \sigma_{11} \\ \sigma_{22} \\ \sigma_{12} \end{Bmatrix} \tag{87g}$$

where

$$\gamma_{12} = 2\, e_{12} = \frac{\partial u_1}{\partial x_2} + \frac{\partial u_2}{\partial x_1} \tag{88}$$

Noting that

$$\omega_{11} = \omega_{22} = 0 \tag{89a}$$

$$\omega_{12} = \omega \tag{89b}$$

and

$$\omega_{21} = -\omega \tag{89c}$$

we have,

$$\sigma_{ij}\,(-e_{ki}\,\delta\omega_{kj} - \omega_{ki}\,\delta e_{kj} + \omega_{ki}\,\delta\omega_{kj}) = \sigma_{11}\,[e_{21}\,\delta\omega + \omega\delta\, e_{21} + \omega\delta\omega]$$

$$+ \sigma_{12}\,[-e_{11}\,\delta\omega + \omega\delta\, e_{22}] + \sigma_{21}\,[e_{22}\,\delta\omega - \omega\delta\, e_{11}]$$

$$+ \sigma_{22}\,[-e_{12}\,\delta\omega - \omega\delta\, e_{12} + \omega\delta\omega] \tag{90}$$

Finally, noting the symmetry of the stress and strain tensors, the right hand side of Eq. 90 can be written in matrix form as,

$$\begin{Bmatrix} \delta e_{11} \\ \delta e_{22} \\ \delta\gamma_{12} \\ \delta\omega \end{Bmatrix}^T \begin{bmatrix} 0 & 0 & 0 & -\sigma_{12} \\ 0 & 0 & 0 & \sigma_{12} \\ 0 & 0 & 0 & \frac{1}{2}(\sigma_{11}-\sigma_{22}) \\ -\sigma_{12} & \sigma_{12} & \frac{1}{2}(\sigma_{11}-\sigma_{22}) & (\sigma_{11}+\sigma_{22}) \end{bmatrix} \begin{Bmatrix} e_{11} \\ e_{22} \\ \gamma_{12} \\ \omega \end{Bmatrix}$$

$$= \{\delta\tilde{e}\}^T\,[A]\,\{\tilde{e}\} \tag{91}$$

where superscript "T" denotes matrix transpose. We note that [A] is a symmetric matrix.

The incremental virtual work expression in matrix form is thus

$$\int_s \{\delta U\}^T \{T + \Delta T\}\, ds + \int_v \rho_o \{\delta U\}^T \{F(\xi)\}\, dv - \int_v \{\delta e\}^T \{\sigma\}\, dv$$

$$= \int_v \{\delta \tilde{e}\}^T [A] \{\tilde{e}\}\, dv + \int_v \{\delta e\}^T \{\Delta\tau\}\, dv \qquad (92)$$

Consider now a generic finite element. We write in symbolic form

$$\{U\} = [N] \{v\} \qquad (93)$$

where $\{v\}$ is a vector of nodal displacements referred to the global fixed Cartesian frame, and $[N]$ is a matrix of coordinate functions. In addition we write,

$$\{e\} = [B] \{v\} \qquad (94)$$

and

$$\{\tilde{e}\} = [\tilde{B}] \{v\} \qquad (95)$$

Matrices $\{v\}$, $[N]$, $[B]$ and $[\tilde{B}]$ for a constant strain triangle are explicitly defined in Appendix II.

We now rewrite Eq. 92 for a single element. Although the equal sign is retained, we recognize that we have true equality only when the contribution of all elements is summed in the manner of the conventional direct stiffness method. Element surface integrals are identically zero unless part of the element boundary is coincident with the body boundary. We have then,

$$\int_s \{\delta v\}^T [N]^T \{T+\Delta T\}\, ds + \int_v \rho_o \{\delta v\}^T [N]^T \{F(\xi)\}\, dv - \int_v \{\delta v\}^T [B]^T \{\sigma\}\, dv$$

$$= \int_v \{\delta v\}^T [\tilde{B}]^T [A] [\tilde{B}] \{v\}\, dv + \int_v \{\delta v\}^T [B]^T \{\Delta\tau\}\, dv \qquad (96)$$

Since Eq. 96 must be satisfied for all kinematically admissible virtual nodal displacements we have,

$$\{\Delta P\} = \int_v [\tilde{B}]^T [A] [\tilde{B}]\, dv\, \{v\} + \int_v [B]^T \{\Delta\tau\}\, dv\, \{v\} \qquad (97)$$

where we compute the nodal force vector as

$$\{\Delta P\} = \int_s [N]^T \{T + \Delta T\}\, ds + \int_v \rho_o [N]^T \{F(\xi)\}\, dv - \int_v [B]^T \{\sigma\}\, dv \qquad (98)$$

We introduce the symbolic constitutive law,

$$\{\Delta\tau\} = [D] \{e\} = [D] [B] \{v\} \qquad (99)$$

Hence $$\{\Delta P\} = \int_v [\tilde{B}]^T [A] [\tilde{B}]\, dv\, \{v\} + \int_v [B]^T [D] [B]\, dv\, \{v\} \qquad (100)$$

We label the tangent element stiffness matrix as $[K]$, where

$$[K] = [K_m] + [K_G] \qquad (101)$$

and $$[K_m] = \int_v [B]^T [D] [B]\, dv \qquad (102)$$

and $$[K_G] = \int_v [\tilde{B}]^T [A] [\tilde{B}]\, dv \qquad (103)$$

We recognize $[K_m]$ as the conventional infinitesimal stiffness matrix and $[K_G]$ is the so-called geometric or initial stress stiffness matrix. The stiffness matrix is referred to the global reference frame.

3.6 Preparation for the Next Increment

Before analyzing a new increment we must determine the Eulerian stress tensor, the mass density and element matrices [N], [B] and $[\tilde{B}]$ in the subsequent configuration. We have

$$\bar{\sigma}_{11} = \tau_{11} \cos^2\omega + \tau_{22} \sin^2\omega - \tau_{12} \sin 2\omega \tag{104a}$$

$$\bar{\sigma}_{22} = \tau_{11} \sin^2\omega + \tau_{22} \cos^2\omega + \tau_{12} \sin 2\omega \tag{104b}$$

$$\bar{\sigma}_{12} = \frac{1}{2} (\tau_{11} - \tau_{22}) \sin 2\omega + \tau_{12} \cos 2\omega \tag{104c}$$

where $\bar{\sigma}_{ij}$ is the Eulerian stress tensor in the subsequent configuration and τ_{ij} is defined by Eq. 76. Also

$$\rho = \frac{\rho_o}{1 + e_{ii}} \tag{105}$$

and matrices [N], [B], and $[\tilde{B}]$ are defined with respect to the subsequent geometry.

4. INTEGRATION OF THE DISPLACEMENT RATE EQUILIBRIUM EQUATIONS

4.1 Introduction

In Chap. 2 we developed a constitutive matrix relating stress rate and strain rate, and in Chap. 3 this matrix was used in the formulation of the tangent stiffness of a generic finite element. A direct sum of element stiffnesses and load vectors yields a set of displacement rate equilibrium equations for the discretized body. This chapter concerns the integration of these equations.

Since we employ here the so-called incremental plasticity theory in which the material response is load path dependent, we deal with displacement rates rather than displacements. If a nonlinear elastic material model had been considered, we would have had the option of formulating equations in terms of displacements and, perhaps, solving these equations iteratively for any applied load. Here we do not have that option and, although iterative techniques can be employed in the solution, we are essentially dealing with an integration procedure, not an iterative procedure.

The displacement rate equilibrium equations are written as follows,

$$[K]\{\dot{V}\} = \{\dot{P}\} \tag{106}$$

where V and P are the displacement vector and load vector respectively of the discretized body. Matrix K is the current tangent stiffness of the discretized body and is a function of the current stress state and current configuration of the body. If plastic unloading is

admitted, the tangent stiffness is also a function of the displacement rate vector. As before, the super dot denotes rate and in particular it implies differentiation with respect to a time like parameter denoted by t. An initial condition associated with Eq. 106 is

$$\{V(t = 0)\} = \{0\} \tag{107}$$

A numerical integration technique is utilized here in which the applied load history (or applied displacement history) is divided into a finite number of increments. In the next section we discuss various methods for numerically approximating incremental response.

4.2 Determination of Incremental Response

All of the methods discussed here can be roughly described as forward integration techniques. Some involve iteration while some do not. Some utilize directly the tangent stiffness while others do not.

Euler Integration Method

Perhaps the most obvious way of approximating the response in an increment is to use the Euler integration method (38) in which the tangent stiffness at the beginning of an increment is used to obtain a linear approximation for incremental response. For example, referring to Fig. 15a, we suppose that the solution at point A is known and we wish to determine incremental displacements ΔV associated with the applied incremental load ΔP. We project along a tangent at point A to obtain an approximate solution denoted by point B. We can expect that after a number of increments the approximate solution

will diverge from the true solution as indicated in Fig. 15b.

In conjunction with a finite element approach, variations of the Euler integration method have been used by Pope (53), Swedlow et al (70), Marcal and King (43), and Yamada and Yoshimura (78) to solve elastic-plastic problems. Pope (53) used a modified Euler approach which accounts for unloading of previously plastified elements as well as yielding of previously elastic elements. Since this information can not be known a priori, an iterative scheme is used. Each iteration involves the solution of a set of linear algebraic equations. Marcal and King (43) used an approach suggested by Marcal (41). Elements which yield for the first time during an increment are assigned a weighted average of elastic and elastic-plastic stiffness, and thus an iterative scheme is required. Yamada and Yoshimura (78) used an Euler approach, however, only one element per increment was allowed to yield.

Runge-Kutta Method

Richard and Blacklock (57) used a fourth order Runge-Kutta method (38) to solve an elastic-plastic problem. Although the solution of four sets of linear equations is required per increment, the method was shown to be clearly superior to Euler's method, at least for the particular problem considered.

Strickland et al (69) treated geometrically nonlinear structures using an initial value formulation. Both a fourth order Runge-Kutta technique and an Adams predictor-corrector method (38) were used to solve the equations.

Initial Strain Method

A number of incremental solution techniques, which do not require formation of the tangent stiffness, have appeared in the literature. One of these techniques, utilized in elastic-plastic problems, is called the initial strain method. Consider now the analysis of an increment. The stress rate-strain rate equation is

$$\{\dot{\tau}\} = [D]\{\dot{e}\} \tag{108}$$

If we employ the Euler method, the incremental constitutive relationship is,

$$\{\Delta\tau\} = [D_o]\{e\} \tag{109}$$

where D_o is the elastic-plastic constitutive matrix evaluated at the beginning of the increment and, as in the last chapter, e denotes incremental strain. An equivalent constitutive relationship is

$$\{\Delta\tau\} = [D^e](\{e\} - \{e^P\}) \tag{110}$$

where D^e is the elastic constitutive matrix. If somehow we knew the value of the incremental plastic strain vector, we could use Eq. 110 rather than Eq. 109 to evaluate element stiffness. Equation 100 would thus become, neglecting geometric stiffness for the moment,

$$\{\Delta P\} = \int_V [B]^T [D^e][B]\, dv \{V\} + \int_V [B]^T [D^e]\{e^P\}\, dv \tag{111}$$

The second integral thus corresponds to an effective load vector which can be shifted to the left hand side leaving only the elastic stiffness on the right.

Gallagher et al (29) suggested this approach for the analysis of linear elastic, hardening materials suffering small displacements. The global elastic stiffness matrix is thus the same for each increment and need be inverted or triangularized only once. The incremental plastic strain vector determined in the immediately preceeding increment is used to estimate the incremental plastic strain vector in the increment being analyzed. For example, once incremental strain and incremental stress have been determined, the increment of plastic strain vector can be computed as

$$\{e^p\} = \{e\} - [D^e]^{-1} [D_o] \{e\} \tag{112}$$

or

$$\{e^p\} = [D_o]^{-1} \{\Delta\tau\} - [D^e] \{\Delta\tau\} \tag{113}$$

where superscript -1 denotes matrix inverse. Equation 112 is associated with the so-called constant strain method of computing plastic strain, while Eq. 113 is associated with the so-called constant stress method (39). As has often been noted the constant stress method breaks down in the presence of perfect plasticity since matrix D_o contains no inverse. The initial strain technique as proposed by Gallagher et al (29) was used by Lansing et al (39) and Armen et al (4) to analyze elastic-plastic problems.

Considering again Eq. 110, if we could choose an incremental plastic strain vector such that the incremental solution satisfied Eq. 109, the initial strain method would be identical to an Euler method. This suggests an iteration technique in which we select an initial incremental plastic strain vector (perhaps that from the

previous increment), solve for incremental response, and compute a new estimate of the incremental plastic strain vector. This procedure would be continued until convergence was obtained.

The above approach was suggested by Argyris (3). A somewhat similar technique was proposed by Capurso (11), where a proof of convergence was presented. An interesting variation of the method was used by Witmer and Kotanchik (76) to analyze perfectly plastic materials. The iterative technique is such that the total stress state at the end of the increment is guaranteed to satisfy the yield inequality, while the incremental stresses and incremental strains satisfy constitutive Eq. 109 where, however, matrix D_o is now evaluated at the end of the increment.

Mendelson and Manson (46) used an initial strain iterative approach to solve simple problems using deformation plasticity. Mendelson (45) presented a generalization of this procedure for incrementally plastic materials. This approach appears to yield a tangent stiffness solution where the tangent stiffness is evaluated at the end of the increment.

Initial Stress Method

Zienkiewicz et al (84) discussed a so-called initial stress iteration technique for elastic-plastic problems. As in the initial strain technique only the elastic stiffness need be formulated and triangularized. A first estimate of the incremental stresses is obtained from an elastic solution. A revised estimate of the incremental stresses is obtained from

$$\{\Delta\tau\} = [D]\{e\} \tag{114}$$

where the constitutive matrix is evaluated at the beginning of the increment. The new estimate of incremental stresses will in general not satisfy equilibrium for the discretized body. The resultant nodal force unbalance is then distributed using the already reduced elastic stiffness. This process is continued until convergence is obtained. At each stage of the iteration process the constitutive matrix is evaluated using the most recently determined stress state. The initial stress technique as proposed by Zienkiewicz et al (84) is similar to the so-called modified Newton-Raphson iterative technique (38).

A variant of the initial stress method was presented by Zienkiewicz and Nayak (81). A first solution for the strains is obtained by using the tangent stiffness at the beginning of the increment (initial tangent stiffness). An associated stress state is then obtained by numerically integrating the stress rate-strain rate equations over the first estimate of the incremental strains. Since these stresses can not be expected to satisfy equilibrium, a nodal force unbalance exists. We can distribute the unbalanced nodal forces using either the current tangent stiffness or the initial tangent stiffness. Again this procedure is repeated until convergence is obtained. If at each stage, the current value of the tangent stiffness is used to distribute the unbalanced nodal forces, the method is similar to a Newton-Raphson iteration (38). If on the other hand, the initial tangent stiffness is always used, the method is similar to a modified Newton-Raphson iteration.

The accuracy of the iteration procedures just described is of course dependent upon increment size as is the case with all of the methods discussed here. Even if a Newton-Raphson like procedure is employed we must still use a fairly large number of increments in order to obtain an accurate solution. This is the case regardless of the convergence criterion used and simply reflects the fact that we employ incremental plasticity theory.

4.3 The Mid-Point Integration Rule

We use here the so-called mid-point integration rule to determine incremental response. This technique has been used previously by Felippa (25), Akyuz and Merwin (1) and Fernandez and Christian (26) to solve elastic-plastic, geometrically nonlinear problems. A non-linear one-dimensional load displacement curve is shown in Fig. 16a. Presumably at point A the true solution is known and we wish to approximate incremental displacement ΔV associated with applied incremental load ΔP.

The mid-point integration rule is motivated by the idea that the secant stiffness, denoted by line AD, can probably be closely approximated by the tangent stiffness evaluated at mid-increment (half of the load increment). The mid-increment stiffness, of course, is not known but we can estimate it. Referring to Fig. 16b, we first apply half the incremental load and use the tangent stiffness evaluated at point A to approximate the mid-increment solution denoted by point B. We subsequently apply the complete incremental load and use the tangent stiffness evaluated at point B to obtain an approximate

incremental solution denoted by point C. In each increment we thus solve two sets of linear, simultaneous, algebraic equations.

Herein the elastic-plastic constitutive matrix is modified at mid-increment to reflect mid-increment stresses. However, neither the geometry nor the geometric stiffness matrix is updated at mid-increment, rather their value at the beginning of the increment is used to compute mid-increment tangent stiffness. This was done in order to save computation time, under the assumption that geometric nonlinearities would not be as severe as material nonlinearities.

4.4 Plastic Unloading

In any elastic-perfectly plastic body with a nonuniform stress field, plastic unloading is a possibility even if the applied loads or applied displacements are monotonically increasing. Herein we check for plastic unloading following the calculation of mid-increment response.

If at the beginning of an increment an element is plastic, the elastic-plastic constitutive matrix is used to calculate the initial tangent stiffness. After mid-increment strains have been determined we check for plastic unloading as follows. If $\lambda < 0$, as defined by Eq. 18, the element has suffered plastic unloading and the elastic constitutive matrix is used to compute mid-increment tangent stiffness. Otherwise, the elastic-plastic constitutive matrix is utilized. Any element which has been found to load plastically at mid-increment is assumed to still be plastic at the end of the increment

regardless of whether the end-of-increment stress state lies inside or outside of the yield surface.

4.5 Stress Scaling Back to the Yield Curve

Consider for the moment an element which is found to be plastic at the beginning of an increment, and assume that the stress state lies exactly on the yield surface. A schematic diagram including a yield curve and the initial stress state, denoted by point A, is shown in Fig. 17a. At the end of the increment the stress state, denoted by point B, probably lies somewhat outside of the yield surface. After a number of such load increments have been analyzed, the stress state may lie far enough from the yield curve to render the analysis of subsequent increments meaningless. A possible stress path produced by a number of increments is denoted by broken line ABC.

In order to correct this situation we scale stresses back to the yield surface at the end of each increment and at mid-increment. Since there is no unique way to scale, we arbitrarily require that the hydrostatic component and principal directions of the stress tensor remain unchanged. A schematic stress path associated with stress scaling is shown in Fig. 17b. As can be seen in the figure, stresses are adjusted back to the yield surface at the end of an increment.

In general the scaled stressed can not be expected to satisfy the equilibrium equations of the discretized body. We thus compute an equilibrium correction vector as per Eq. 98 and apply this load vector, along with the prescribed loads, in the next increment.

4.6 Elements Which Yield During an Increment

We have yet to discuss the transition of an element from an elastic to a plastic stress state. We discuss now a technique for treating elements which yield during an increment.

Assume that the stress state at the beginning of the increment lies within the yield surface. We then use the elastic constitutive matrix to compute the initial tangent stiffness. Let

$$k_1 = \alpha p + J_2^{1/2} \tag{115}$$

where p and J_2 are evaluated at the beginning of the increment. Similarly, to evaluate k_2 we use the stress state at mid-increment, and k_3 is to correspond to the stress state at the end of the increment, which we do not yet know. However we can estimate k_3 as follows,

$$k_3 = k_1 + 2(k_2 - k_1) \tag{116}$$

If k_3 is greater than the yield value k, we can expect that the element will yield during this increment. In a somewhat arbitrary manner we require that if

$$\frac{k_2 - k_1}{k - k_1} \leq \frac{2}{3} \tag{117}$$

the elastic constitutive matrix is used to compute mid-increment tangent stiffness. If

$$\frac{k_2 - k_1}{k - k_1} > \frac{2}{3} \tag{118}$$

we use a weighted average of the elastic and elastic-plastic constitutive

matrices in a manner similar to Marcal (41).

To compute the averaged matrix, the stress state at mid-increment is scaled to the yield surface using the technique described in the previous section. The averaged constitutive matrix is then computed as

$$[D]_{avg.} = m\,[D^e] + (1 - m)\,[D] \tag{119}$$

where

$$m = \frac{k - k_1}{2(k_2 - k_1)} \tag{120}$$

and D is evaluated at the scaled stress state.

If an averaged matrix has been used to determine mid-increment stiffness, the element is assumed to be plastic at the end of the increment regardless of whether the stresses lie inside or outside of the yield surface. The final stress state is then scaled to the yield surface. If the elastic constitutive matrix has been used to compute mid-increment stiffness, we check for yielding at the end of the increment. If the stress state lies outside the yield surface we scale back to yield in preparation for the next increment. Otherwise we leave the stress state unchanged and use the elastic constitutive matrix to start the next increment.

4.7 Solution of the Linear Algebraic Equations

We use here the so-called square-root method (38) to solve the linear simultaneous algebraic equations associated with the mid-point integration rule. The banded character of the global stiffness

matrix was considered when coding this procedure for the computer.

A number of investigators have preferred to use iterative procedures to solve the linear equations involved in elastic-plastic incremental analysis (1) (43). Iterative methods are appealing since we can obtain a reasonably good initial guess for the solution in the current increment by using the known solution for the previous increment. Most investigators have, however, used direct methods and we follow suit here.

5. CHECK PROBLEMS AND NUMERICAL EXPERIMENTS

5.1 Introduction

There exist no closed form solutions for the class of problems being considered here, that is, a punch bearing on a finite stratum (or infinite halfspace) of elastic-plastic material under the conditions of plane strain. Two extreme parts of the small displacement solution are however known--the linear elastic solution and the plastic collapse or limit load solution, at least for some materials. However we have no absolute check on the accuracy of the elastic-plastic intermediate response.

The numerical methods used here, the particular algorithms used in the computer program as well as possible mistakes in the computer coding are all potential sources of error. In order to demonstrate that the computer program is giving reasonable and believable results, a number of example problems are presented in this section. We first discuss the solutions of some simple but nontrivial problems followed by solution of complex problems that have been numerically analyzed by other investigators. Finally we present the results of some numerical experiments in which the effect of some of the variables associated with the numerical methods used here are investigated.

5.2 A Plane Strain Compression Test

Consider a hypothetical one-dimensional plane strain compression test of an elastic-perfectly plastic Mohr-Coulomb material. Since the Mohr-Coulomb yield function is independent of the out-of-plane

stress, the applied stress at which the material first yields is identical to the maximum stress. However, this is not the case for a Drucker-Prager material. After first yield, additional stress can be applied and the change in the out-of-plane stress is just sufficient to maintain the stress state on the yield surface.

For a Drucker-Prager material the stress at first yield is dependent on Poisson's ratio, and the difference between the maximum stress and the stress at first yield is most pronounced for a Poisson's ratio of zero. Consider for example the following material parameters,

$$E = 500{,}000 \text{ psf}$$

$$\nu = 0$$

$$C = 500 \text{ psf}$$

$$\varphi = 30^{\circ}$$

With α and k defined by Eqs. 4 and 5 respectively, the applied stress at first yield is 990 psf and the exact maximum applied stress is 1730 psf (same as for a Mohr-Coulomb material).

We show in Fig. 18 the complete Drucker-Prager stress-strain curve for the material parameters shown above, as obtained from the computer program utilized here. As would be expected first yield occurs at about 1000 psf and the maximum stress is 1725 psf. The open circles represent actual computed points.

5.3 An Elastic Large Deformation Problem with Uniform Stress

Consider now the plane strain problem shown in Fig. 19 in which an elastic specimen is bounded on three sides by smooth rigid

walls, and a uniform stress is applied to the fourth side. The linear solution to the problem is, of course,

$$\sigma = \bar{E}\ (u/\ell_o) \tag{121}$$

where

$$\bar{E} = \frac{E\ (1 - \nu)}{(1 + \nu)\ (1 - 2\nu)} \tag{122}$$

ℓ_o is the original length of the specimen and u is the vertical displacement of the applied stress.

If displacements are large we might relate the stress to the so-called logarithmic strain, that is,

$$\sigma = \bar{E}\ e_\ell \tag{123}$$

where

$$e_\ell = \int_o^u \frac{du}{\ell_o - u} = \text{Ln}\left[\frac{\ell_o}{\ell_o - u}\right] = \text{Ln}\left[\frac{1}{1 - (u/\ell_o)}\right] \tag{124}$$

Thus

$$\sigma = \bar{E}\ \text{Ln}\left[\frac{1}{1 - (u/\ell_o)}\right] \tag{125}$$

A nondimensionalized plot of this equation is shown in Fig. 19 along with two numerical solutions, one obtained using six increments and one with twelve increments. It appears that the approximate solution converges towards the true solution as the number of increments increases.

5.4 Notched Tensile Specimen

A number of investigators have presented numerical results for the plane strain notched tensile specimen (43)(84) and we also consider this problem here. One half of the specimen, along with

relevant dimensions and material properties, is shown in Fig. 20, where $\sigma_o = 24.3$ kg/mm^2 is the yield stress in simple tension. The material is assumed to be elastic-perfectly plastic with a von Mises yield condition and, in terms of the model used here, $\alpha = 0$ and $k = \sigma_o/\sqrt{3} = 14.03$ kg/mm^2. Kachanov's (37) slip-line solution for this problem gives

$$\sigma_{max}/\sigma_o = .8925 \tag{126}$$

where σ_{max} is the maximum or collapse value of the applied stress σ. For $\sigma_o = 24.3$ kg/mm^2, the limit stress $\sigma_{max} = 21.6$ kg/mm^2.

The finite element mesh used here is shown in the left hand half of Fig. 20 and consists of 105 nodes and 169 triangular elements. This mesh is similar to, but not exactly the same as, that used by Zienkiewicz et al (84). In Fig. 21 the applied stress is plotted versus the centerline displacement at the end of the specimen. The curve remains almost linear up to 18 kg/mm^2, after which it bends over quite rapidly. A fairly well defined limit load is reached at about 22.5 kg/mm^2, only 4 percent above the slipline solution. Zienkiewicz et al (84) reported a so-called lower bound for the limit load of 19.4 kg/mm^2, that is, this was the last load at which their iterative procedure converged. This solution represents a true lower bound for the discretized body since the iterative procedure utilized ensures that the discrete equations of equilibrium and the yield inequality are satisfied at the end of each increment. However this may not represent a lower bound for the continuum since the continuum equations of equilibrium are in general not satisfied by a finite element solution.

Zones of yielding for loads of 15 and 18 kg/mm^2 are shown in the right hand half of Fig. 20 and are similar to those reported by Marcal and King (43) and by Zienkiewicz et al (84). Yielding starts at the notch root and spreads upward and toward the centerline. At 18 kg/mm^2 the zone of yielding has just extended across the entire specimen. Until this point, the load displacement response is essentially linear and afterwards it becomes highly nonlinear.

5.5 Uniform Strip Load on Undrained Clay

Apparently Hoeg, Christian and Whitman (35) were the first to treat soil as an elastic-perfectly plastic material for the purpose of obtaining the complete load displacement response of a strip footing. A shallow layer of undrained clay, shown in Fig. 22, was analyzed using the finite difference like technique of Ang and Harper (2). The Tresca yield condition and its associated flow rule were utilized with a cohesive strength of 17.5 psi, and the footing load was assumed to be uniformly distributed.

Here we solve this same plane strain problem using the finite element method and the von Mises yield condition. Both yield conditions should give the same limit load (k defined by Eq. 5) but the intermediate response may be different. Two different meshes are utilized here. One mesh is uniform (Fig. 22) and is similar to that used by Hoeg et al (35), while the other is nonuniform (Fig. 24) and is similar to that used here for a deeper soil stratum. Boundary conditions in both meshes are identical to those used by Hoeg et al (35). The base of the clay stratum is rigid and perfectly rough,

while the vertical boundary is assumed to be rigid and perfectly smooth. The uniform mesh is shown in the left hand half of Fig. 22 and consists of 120 nodes and 98 rectangular elements. Each rectangle is defined by four constant strain triangles. Since the mesh is perfectly uniform we are actually considering a loading width of 10.28 ft. rather than 10 ft. as used by Hoeg. We assume that this will make little difference in the solution and subsequent results show this to be the case.

Results for the uniform mesh are shown in Fig. 23 where the applied pressure is plotted versus the centerline displacement directly beneath the load. The closed circles correspond to actual computed points indicating that sixteen increments were used in the solution. This solution agrees almost point by point with that presented by Hoeg. We obtained here a well defined numerical limit load of 92 psi while Hoeg reported 90 psi. Both values are in remarkable agreement with the exact value of 90 psi.

Valliappan (73) also solved this same problem using the von Mises yield condition and a somewhat coarser finite element mesh of 94 nodes and 150 triangular elements. As might be expected his solution, also shown in Fig. 23, lies above that presented here. The initial stress method (84) was used to integrate the equations and the last load at which this iterative technique converged was 78 psi.

Zones of yielding defined by the rectangular mesh are shown in the right hand half of Fig. 22. These zones agree fairly well with those presented by Hoeg for loads of 53 psi and 90 psi.

A nonuniform mesh consisting of 100 nodes and 90 elements (Fig. 24) was also used to analyze this problem. Each quadrilateral in the nonuniform mesh was divided into four constant strain triangles. Near the edge of the footing this mesh is finer than the uniform mesh while away from the footing edge this mesh is somewhat coarser. The two meshes gave nearly identical results except near the maximum load where the nonuniform mesh overestimated the limit load by 7 percent.

For this particular problem in which the footing load is uniformly distributed, there is no need for such a fine mesh near the edge of the footing and the nonuniform mesh is probably to coarse away from the footing. However, comparative analyses for a rigid footing show the nonuniform mesh to be superior to the uniform mesh. Since we are primarily concerned here with rigid footing and deeper soil strata, a nonuniform mesh will prove to be a necessity.

5.6 Elastic Cantilever Beam

In order to investigate the geometrically nonlinear algorithms used in the computer program, we consider here a cantilever beam suffering large displacements. Although the nonlinear elastic solution for slim cantilever beams is known (rotations large, strains small, shearing deformation negligible) we will not be able to check with this solution because of the relative coarseness of the finite element mesh. We will however be able to get some feeling for the affect on the solution of geometric stiffness and equilibrium correction.

The cantilever beam is 10 ft. long with a 1 ft. square cross-

section. Poisson's ratio is equal to zero so that the out-of-plane normal stress is identically zero. A uniform finite element mesh was utilized consisting of 147 nodes and 240 triangular elements with 7 nodes through the depth of the beam and 21 nodes along the length. Portions of the mesh are shown in Fig. 25. The applied load was assumed to be distributed parabolically over the cross-section. Consistent nodal forces associated with a unit applied load are shown in Fig. 25.

Some results are shown in Fig. 26 where the nondimensionalized force $PL^2/3EI$ is plotted versus the nondimensionalized vertical displacement Δ/L at the end of the beam. Here L is the beam length, P is the applied load and I is the cross-section moment of inertia. The lower solid line corresponds to the small displacement solution for the discretized beam and is hence linear. The upper solid curve corresponds to a nonlinear solution obtained using 16 increments. The three additional solutions were obtained using 8 increments.

The solution denoted by open circles utilized the complete integration scheme as described in the previous chapter. The solution denoted by triangles did not use equilibrium correction, while the solution denoted by open squares utilized neither equilibrium correction nor the geometric stiffness matrix. Comparing the three solutions with the sixteen increment solution, which we expect is close to the exact solution, the complete integration scheme is clearly superior to the alternate schemes.

The power of the equilibrium correction vector is particularly noteworthy. Not only does it improve the solution but it tends to maintain a constant percentage error. The percentage error associated with the alternate solutions tends to grow with each increment.

5.6 Rigid Strip Footing on a Soil Stratum

In this section we consider a number of variables associated with the finite element discretization and the numerical integration technique used here. The problem used for the experiments is the same as that considered in the next chapter, that is, a 5 ft. wide rigid strip footing bearing on a 50 ft. deep soil stratum supported by a rigid rough base. The horizontal extent of the stratum was arbitrarily set at 50 ft. from the footing center and a smooth rigid boundary was prescribed. The following soil parameters were used

$$E = 500{,}000 \text{ psf}$$

$$\nu = .3$$

$$C = 500 \text{ psf}$$

$$\varphi = 30^{\circ}$$

$$\gamma = 0.$$

where γ is soil weight per unit volume.

Finite Element Discretization

Three finite element meshes, shown in Figs. 27, 28 and 29, were utilized for the numerical experiments. Each mesh is composed of a number of triangular and quadrilateral regions. Three different arrangements of triangles were used to define stiffness for the

quadrilateral regions. In the first arrangement, pictured in Fig. 30a, the quadrilaterals are divided into two triangles with the dividing diagonal having the same orientation for all quadrilaterals. The second arrangement is shown in Fig. 30b, and here the diagonals are staggered. In the third arrangement, shown in Fig. 30c, the quadrilateral is subdivided into four triangles connected to a fifth node located at the quadrilateral centroid. Static condensation is used to reduce the 10x10 quadrilateral stiffness to the desired 8x8 (74). Triangle stiffness is based on a linear displacement expansion (constant strain triangles).

All three meshes, as shown in Figs. 27, 28 and 29, are finest near the corner of the footing and get progressively coarser as the distance from the corner increases. It is not the aim here to capture the stress singularity at the corner since it is well known that it is difficult or perhaps impossible to do this with analytic finite element expansions (47). The aim here is simply to make the mesh fine where stress gradients are high.

We discuss now the results of four numerical experiments in which the effects of mesh size, element arrangement, increment size, and stress scaling with associated equilibrium correction were investigated. Since the footing is assumed to be rigid, displacements rather than stresses are prescribed beneath the footing. For all of the numerical experiments the footing is assumed to be smooth and displacements are assumed to be small, that is, for the moment we consider only material nonlinearities. The theoretical bearing capacity

obtained by Prandtl (56) is q_o = 15,040 psf. Shield (65) has shown that the Prandtl solution is the true limit load for weightless soils with a Mohr-Coulomb yield condition and the associated flow rule.

Effects of Mesh Size

Results for the three meshes are shown in Fig. 31 where we plot average stress beneath the footing, q, versus vertical displacement of the footing. Element arrangement 3 (Fig. 30) was used to compute quadrilateral stiffness for the quadrilateral regions shown in Figs. 27, 28 and 29, and an increment size of .04 ft. of footing displacement per increment was used. Although the curves shown are smooth, there were some oscillations in the solutions, particularly at the higher loads. As might be expected, the finest mesh gave the softest response. Even with the finest mesh there is still a noticeable difference between the theoretical plastic limit load and that determined from the numerical finite element solution. If we take the limit load of the discretized body associated with mesh 3 (Fig. 29) to be 18,500 psf, then this load is approximately 23 percent greater than the theoretical limit load.

Effects of Element Arrangement

Figure 32 shows the results for the three element arrangements for the quadrilateral regions shown in Fig. 28 (mesh 2) and .04 ft. of footing displacement per increment. Most remarkable is the large difference in the solutions obtained from arrangements 1 and 2. Many writers have commented on the stress discontinuities between adjacent elements when constant strain triangles are used in finite

element analysis (for a recent example see Owen et al (52)). In regions where the stress gradient is high, element stresses tend to oscillate from element to element. This tendency is particularly noticeable in element arrangement 1 where stresses at the higher loads oscillate from tension to compression. The best solution was obtained with element arrangement 3, but we should note that computation time was approximately 40 percent greater than the time required for arrangements 1 and 2.

Effects of Increment Size

The effect of the size of the footing displacement increment is shown in Fig. 33. Mesh 2 (Fig. 28) with element arrangement 2 for the quadrilateral regions was used for the three solutions. Three displacement increments were utilized, 0.02, 0.04 and 0.08 ft. per increment. Up to a footing displacement of about 0.7 ft. the solutions are essentially the same. After this the three curves diverge somewhat with the smallest increment size giving the softest response. We can see that the integration scheme is not highly sensitive to increment size, at least at low and intermediate load levels.

Effect of Stress Scaling

In the context of geometrically nonlinear analysis, Strickland, Haisler, and Von Riesemann (69) have shown that correcting for nonequilibrating stresses significantly increases accuracy when used in conjunction with an incremental Euler integration approach. The cantilever beam analysis presented here corroborates this conclusion. We show now that for elastic-plastic analysis, scaling stresses back

to the yield surface and subsequently distributing the unbalanced nodal forces during the next increment is also computationally efficient.

In Fig. 34 two of the solutions were obtained without scaling stresses back to the yield surface after each increment. Thus, to within round-off and truncation errors, stresses determined at the end of each increment satisfied equilibrium. A third solution, shown by open circles in Fig. 34, was obtained using stress scaling and equilibrium correction. We note first of all that for the same increment size there is a noticeable difference in the solutions with and without scaling. We note secondly that the solution without scaling can be made to agree closely to the solution with scaling by using a very small increment size. We can thus conclude that for a small increase in computational effort, we get a significant increase in accuracy by using stress scaling with equilibrium correction.

6. ELASTIC-PLASTIC ANALYSES OF A FOOTING ON HOMOGENEOUS CLAY STRATA

6.1 Introduction

We consider here a 50 ft. deep soil stratum loaded by a 5 ft. wide strip footing. The width of the stratum is taken to be 50 ft. The base of the soil stratum is assumed to be rigid and perfectly rough, and the footing is also assumed to be rigid and perfectly rough. The finite element mesh shown in Fig. 29 was used for all of the analyses presented in this chapter, where the quadrilateral regions were defined by four constant strain triangles. The boundary conditions are identical to those shown in Fig. 29.

An elastic stratum is treated first in order to compare the finite element solution with an existing exact solution. Subsequently we consider an elastic-plastic effective stress analysis of an overconsolidated clay, and finally an elastic-plastic total stress analysis of an undrained clay is presented. For the elastic-plastic cases both small and large deformation analyses are considered, that is, solutions are presented with and without geometric nonlinearities included in the equilibrium equations (as described in Chap. 3).

6.2 Elastic Solution for a Rough Rigid Footing

We compare in this section finite element solutions for a finite elastic stratum with exact solutions for an infinite halfspace (48). The finite element solutions and the exact halfspace solution should be in general agreement near the footing but will not necessarily agree near the soil stratum base. Finite element stresses presented

in this chapter correspond to nodal stresses and were determined from a simple average of the stresses in all triangles adjacent to a particular node. For example, if a node is adjacent to four quadrilateral elements, each nodal stress would be an average of eight triangle stresses.

Vertical and horizontal stress distributions for a Poisson's ratio of 0.3 are listed in Tables 1 through 3. The sign convention is shown in Fig. 1 where positive normal stresses correspond to compression. In Table 1 contact stress distributions at the footing-soil interface are presented. In Table 2 stress distributions along a vertical line beneath the footing centerline are presented, while Table 3 shows stress distributions along a vertical line beneath the footing corner.

Referring to Table 1, both horizontal and vertical contact stresses, as computed from the finite element method, are seen to agree well with the halfspace exact solution, except near the footing corner. The vertical stress components, σ_y, agree somewhat less well than the horizontal stress components, σ_x, with the differences ranging from 3 to 10 percent. Considering now the stresses below the footing centerline (Table 2), the vertical stress components, σ_y, agree remarkably well whereas the horizontal stress components, σ_x, differ somewhat. This difference most likely reflects the finite stratum depth in the finite element analysis and should not be interpreted as an indicator that the present finite element mesh is not fine enough to capture the true solution. Likewise considering the stress distributions beneath the footing corner (Table 3) the vertical stress components agree well

while the horizontal stress components differ somewhat.

In Tables 4 and 5 halfspace stress components are presented for Poisson's ratios of 0.48 and 0.5, while the corresponding finite element stress components are presented for a Poisson's ratio of 0.48 only. A Poisson's ratio of 0.5 is relevant to undrained total stress analysis in which clay is assumed to be incompressible. However the displacement formulation utilized herein does not admit a Poisson's ratio of 0.5 since the constitutive matrix becomes singular. Nevertheless we can attempt to approximate the incompressibility condition by using a high value of Poisson's ratio such as 0.48. We present exact solutions for both values of Poisson's ratio in order to examine the validity of this approximation.

Examination of Tables 1 through 5 reveals that Poisson's ratio has little effect on the vertical stress components, σ_y. Considering Table 4 we see that the horizontal contact stresses are decreased by about 10 percent when Poisson's ratio is reduced from 0.5 to 0.48. However referring to Table 5, we need move only 1 ft. below the footing for the difference to be reduced to about 3 percent. We conclude therefore that we can obtain a reasonable approximation for the incompressible case by using a Poisson's ratio of 0.48. We note further the good correlation between the finite element stresses and the halfspace stresses as indicated in Tables 4 and 5.

6.3 Elastic-Plastic Analysis of a Footing on an Overconsolidated Stratum of Insensitive Clay

We deal here with an effective stress analysis of an overconsolidated clay. Presumably the load rate is such that no excess pore water pressures are generated. The material parameters utilized in this study are:

$E = 5 \times 10^5$ psf $\quad \varphi = 10^\circ, 20^\circ$ and 30°

$\nu = 0.3 \quad \gamma = 50$ pcf

$C = 500$ psf $\quad K_o = 1.0$

where K_o is the ratio of the initial in-situ horizontal and vertical stress components. Only the friction angle φ is varied here with all other parameters being held constant.

In Chap. 5 we presented a solution for a smooth footing bearing on a weightless C-φ soil. For a friction angle of 30 degrees and a cohesive strength of 500 psf, it was shown that the numerically determined limit load (limit load determined from the finite element analysis) was 23 percent greater than the exact limit load. We consider here a more realistic problem of a rough footing bearing on a ponderable soil, for which exact limit loads have not as yet been determined. We can, however, use the limit analysis technique of Chen and Davidson (12) to estimate the limit loads to within 1 to 2 percent for the soil parameters considered here. The approximate limit loads are thus $q_o = 4350$, 8260 and 18,720 psf for friction angles of $\varphi = 10^\circ$, 20° and 30° respectively.

Load-Displacement Curves

Load displacement curves for large and small deformation analyses are shown in Figs. 35 through 37 for the three friction angles mentioned above. The closed and open circles represent actual computed points and the solution following each increment is plotted. None of the solutions are perfectly smooth but show some oscillations.

Considering first the small deformation solutions, we note that the limit loads are overestimated in each case with the error increasing with increasing friction angle. For friction angles of 10, 20 and 30 degrees, the errors are 10, 18 and 26 percent respectively. Considering the entire elastic-plastic solution where the load is increased from zero to failure, we know from the above discussion that the initial part of the load-displacement curve is highly accurate because the soil stratum is behaving essentially as an elastic medium. However, as the load increases we can expect that the numerical solution presented here diverges from the true solution, given the known error in the limit load. It is also apparent that as the friction angle increases, the mesh must become finer if the limit load is to be captured within a specified tolerance.

Consider now the solution obtained from a large deformation analysis for the case $\varphi = 10^{\circ}$ (Fig. 35). Except near the limit load the load displacement curve corresponding to the large deformation analysis is identical to that of the small deformation solution. Near the limit load the two curves diverge somewhat with the large deformation curve appearing to approach a limiting load only 2 percent

above the small deformation numerical limit load at the displacement of 0.27 ft. In this case ($\varphi = 10^{\circ}$) we can thus say that the small deformation analysis is valid for all load levels up to and including the limit load. In addition the small deformation limit load is clearly a meaningful measure of the maximum bearing capacity of the footing.

Referring now to Fig. 36, we can see that if the friction angle is increased to 20 degrees, the load-displacement curves corresponding to the small and large deformation analyses remain essentially the same except near the small deformation limit load. Whereas the small deformation curve bends over and approaches a maximum, the large deformation curve continues to rise without any apparent limit. Although in this case the small deformation limit load is not a true measure of the maximum bearing capacity of the footing, it is nevertheless an indicator of the load level at which large increases in footing displacement can be expected for small increases in footing load.

Although there is a marked difference in the solutions by the small and large deformation analyses for the case when $\varphi = 30^{\circ}$ (Fig. 37), the two curves are still virtually the same up to about 75 percent of the numerical limit load. Beyond this point the solutions diverge. There is no noticeable break in the large deformation curve, rather the curve rises smoothly past the small deformation numerical limit load. We may conclude that for this particular set of soil parameters, the small deformation perfectly plastic limit load solution is not a meaningful measure of the bearing capacity of the footing. We

might note, however, that a friction angle of 30 degrees is higher than would be expected for an overconsolidated clay.

Clearly with all other parameters held fixed, an increase in the friction angle is associated with an increase in the difference between the small and large deformation solutions. In general if the elastic parameters are held fixed while the strength parameters increase, we can expect an increase in the difference between the two solutions.

Referring to Fig. 36, we see that for $\varphi = 20^{\circ}$, the footing has displaced almost half a foot by the time the numerical limit load has been reached. The corresponding deformed surface profile at the numerical limit load is shown in Fig. 38. In Fig. 38(a) the surface profile is drawn to scale while in Fig. 38(b) it is not. If the small and large deformation solutions differ significantly we would expect the deformed geometry and initial geometry of the soil stratum to differ also significantly. Figure 38 clearly shows this to be the case. We can also see from Fig. 38 that soil deformation must be severe near the footing corner. In Fig. 38(b) we show a deformed surface profile for both small and large deformation solutions. There is a noticeable difference between the two profiles corresponding to similar load levels. The footing displacement determined from the large deformation analysis is less than that determined from the small deformation analysis. This is consistent with the load-displacement curves shown in Fig. 36 where the large deformation solution is stiffer than the small deformation solution.

In the remainder of this section we consider in some detail the behavior of a soil with a friction angle of 20 degrees and a cohesive strength of 500 psf. In Figs. 39 through 41 we show stress distributions at various load levels as obtained from a small deformation analysis, and in Figs. 42 and 43 stress distributions from large and small deformation analyses are compared. None of these stress distributions include the initial overburden stresses.

Stress Distributions

Referring to Figs. 39 through 41, at a load of 1140 psf some yielding has occurred near the footing corner but most of the soil stratum is still elastic. At q = 4030 psf significant yielding has occurred and q = 9620 corresponds to the numerical limit load. Considering first the contact stress at the soil-footing interface (Fig. 39), the stress distributions at q = 1140 psf are essentially that of an elastic body. The vertical stress component, σ_y, at the footing corner is about three times that at the footing center. As the load increases and yielding spreads, the horizontal and vertical stress distributions tend to become flatter. At the numerical limit load the vertical stress, σ_y, at the corner is only about 30 percent greater than that at the footing center. As would be expected the shearing stress, τ_{xy}, has completely changed direction by the time the numerical limit load has been reached.

The shearing stress distribution at the limit load is nearly linear up to a peak value of about 1700 psf, after which it falls off sharply. If we define the maximum value of the mobilized friction

angle between the footing base and adjacent soil to be

$$\delta_m = \tan^{-1}\left(\frac{\tau_{max} - C}{q_o}\right) \tag{127}$$

where τ_{max} is the maximum value of the contact shearing stress, then for friction angles of 10, 20 and 30 degrees, $\delta_m = 2^\circ$, 7° and 11° respectively. Thus for the material parameters studied here, a friction angle between footing base and soil of 11 degrees is sufficient to produce an essentially perfectly rough condition. This is consistent with the results of Chen and Davidson (12).

In Figs. 40 and 41 horizontal and vertical stress distributions along vertical lines beneath the footing center and corner are shown. As the load increases and yielding spreads, the distributions change somewhat, particularly near the footing. There is a noticeable change in the shearing stress distribution beneath the footing corner as the load increases.

Stress distributions at the numerical limit load are shown in Figs. 42 and 43 for small and large deformation analyses. Referring first to the contact stresses shown in Fig. 42, vertical and horizontal stresses differ only near the footing corner, although the shearing stresses differ all along the footing. As can be seen in Fig. 43, stresses beneath the footing corner differ only near the footing. At a depth of 3 to 4 ft. beneath the footing, the large and small deformation stresses are essentially the same.

Yield Zones

In Fig. 44 zones of yielding for various load levels are presented. Theoretically some yielding should occur near the footing corner for any load level since the true solution contains a singularity at the corner. In the finite element solution yielding occurred in the first increment of loading ($q \approx 1140$ psf) and a small yield zone near the footing corner can be seen in Fig. 44. As the load increases yielding spreads downward and toward the footing centerline. The yield zone reaches the footing centerline at a load just below 3240 psf. The zone of yielding continues to spread outward from the footing as the load increases. In addition yielding spreads upward toward the footing until at a load of 6740 psf all of the soil immediately below the footing is yielded. At the numerical limit load (9620 psf) a significant portion of the soil stratum has yielded.

In Fig. 45 we show the yield zone at the numerical limit load for $\varphi = 30^{\circ}$. The extent of yielding at the limit load is clearly influenced by the value of the friction angle φ. As can be seen from the figure, small and large deformation solutions give somewhat different zones of yielding at similar load levels. The large deformation analysis produces a smaller zone of yielding, and as partial explanation for this we note that as the footing punches down into the clay, an effective surcharge is created by the clay which now lies above the footing base. This surcharge should increase the hydrostatic stress component and thus increase the shear required to yield the soil.

Velocity Fields

Finally in Fig. 46 we show the velocity field at the numerical limit load for a friction angle of 20 degrees. Superimposed on the figure is the outline of the Prandtl velocity field which is only strictly applicable to weightless soils. However for the particular set of soil parameters used here, the actual velocity field and the Prandtl field can be expected to be similar. It can be seen in Fig. 46 that the Prandtl field and the numerically determined field are indeed similar. We can clearly identify a wedge beneath the footing which moves downward with the footing. There is also an intermediate zone in which the velocity vectors are essentially perpendicular to radial lines eminating from the footing corner. The velocity magnitude can also be seen to grow as the radial line rotates counterclockwise. A fairly well defined third zone exists which appears to be moving upward and out as a rigid body. This problem was also solved for a weightless soil (all other material parameters unchanged) and the velocity field determined at the limit load was virtually the same as that shown in Fig. 46. The velocity field at a similar load level and as determined from a large deformation analysis is shown in Fig. 47. It is no surprise that there is a distinct difference between the small and large deformation fields since the large deformation solution has yet to reach a limiting load.

In Fig. 48 the velocity field, at the numerical load, for a smooth footing bearing on a weightless C-φ soil is shown. The outline of a Hill like velocity field is also shown in the figure. The Hill velocity field has been described by Chen and Davidson (12)

and is characterized by two wedges beneath the footing rather than one as in the Prandtl mechanism. Each wedge makes an angle of 55 degrees with respect to the footing base. As can be seen in Fig. 48, the numerically determined velocity field does not exactly correspond to the Hill field, nor does it correspond to the Prandtl field, although it contains characteristics of both fields.

6.4 Elastic-Plastic Analysis of a Footing on a Stratum of Undrained Clay

We deal here with an elastic-plastic total stress analysis of a saturated undrained clay. Presumably the load rate is such that the excess porewater pressure has no chance to dissipate, that is, volumetric strain is almost zero throughout the analysis. The material parameters utilized in this study are

$E = 1 \times 10^5$ and 1×10^6 psf $\quad \varphi = 0$

$\nu = 0.48 \quad \gamma = 100$ pcf

$C = 1000$ psf $\quad K_o = 1.0$

With $\varphi = 0$, the Drucker-Prager yield function reduces to a von Mises function.

Only Young's modulus is varied here. Two values of the ratio E/C are considered, namely 1000 and 100. This ratio in real soils is expected to range from approximately 100 to 3000 with perhaps 1000 being a typical value (14). In the following we consider first the case of a soil with a Young's modulus of 1×10^6 psf and present a fairly detailed description of the soil response to the footing load. Only limited data is presented later for the case of a soil with a Young's modulus of 1×10^5 psf.

Case 1 - $E = 1 \times 10^6$ psf

Load displacement curves obtained from small and large deformation analyses are shown in Fig. 49 for a Young's modulus of 1×10^6 psf. The curves are almost linear up to a load of 3600 psf. After this point the curves bend over quite sharply and gradually approach the numerical limit loads corresponding to small and large deformation analyses. The two curves are seen to be essentially identical. Thus for E/C = 1000, the small deformation solution is valid for all load levels up to and including the limit load. The exact limit load for this problem is 5140 psf and the numerical limit load is 10 percent above this value.

Stress distributions for various load levels are shown in Figs. 50 through 52. At 800 psf the soil stratum was essentially elastic. Considerable yielding had occurred at q = 3060 psf, and q = 5520 psf corresponds to the numerical limit load. There is a marked similarity in these curves and those obtained for a C-φ soil (Figs. 39 through 41). It is of interest to note that the maximum contact shearing stress at the limit load is equal to the cohesive strength (1000 psf).

Zones of yielding for various load levels are shown in Fig. 53. Again yielding starts at the corner of the footing and spreads downward and toward the footing centerline. At a load of about 3610 psf the yield zone has just reached the footing centerline. At this point the footing and an adjacent elastic wedge (which makes a 45 degree angle with the base) are separated by a band of yielded material

from the remainder of the still elastic stratum. The spread of the yield zone to the centerline is coincident with the sharp break in the load displacement curve (Fig. 49). This kind of behavior is similar to that noted for the notched tensile specimen (Chap. 5). At the numerical limit load all of the soil directly beneath the footing has yielded. At the limit load the zone of yielding in the present case ($\varphi = 0$) is considerably smaller than that of C-φ soils (Figs. 44 and 45).

The corresponding velocity field at the numerical limit load is shown in Fig. 54 along with the outline of the Prandtl velocity field. The velocity field is denoted by the small arrows. The close agreement between the two fields is evident. Outside of the Prandtl field the velocity magnitudes are too small to appear in the figure. In Fig. 55 we show the velocity field at the limit load for a smooth footing bearing on the same material. The outline of the Hill velocity field (55) is also superimposed on the figure. Although the numerical velocity field is similar to the Hill field, it can not be said to be identical to the Hill field. The numerical field, in fact, appears to be a combination of the Hill and Prandtl fields. Prager and Hodge (55) have previously suggested a combination of the Hill and Prandtl fields as a possible failure mode.

Case 2 - $E = 1 \times 10^5$ psf

Load displacement curves for the case of a clay with a Young's modulus of 1×10^5 psf are shown in Fig. 56. The shape of the small deformation curve must, of course, be identical to that for

a Young's modulus of $1x10^6$ psf. The ratio, E/C, is 100 here and we see from the figure that the small and large deformation analyses produce somewhat different results. The large deformation curve stops at a load of approximately 5600 psf. Although the analysis was continued beyond this point, the response became somewhat erratic. A very curious velocity field was observed at 5600 psf and is shown in Fig. 57. A wedge beneath the footing is moving downward with the footing, and the soil adjacent to the wedge is being squeezed up and to the right. Beyond this is a region resembling a radial shear zone, and finally there is a rigid zone moving up and to the right.

In an attempt to obtain an improved solution, the problem was recomputed using half of the original increment size. The revised solution lay slightly above the original solution and a maximum load of about 5800 psf was obtained. At this point a solution for the linear equations could not be obtained. The problem was also solved using a reduced Poisson's ratio of 0.4 and again the solution behaved irregularly at about 5800 psf. Thus in the context of the finite element mesh and numerical integration scheme used here, the maximum footing load is 5800 psf. It may be the case that the velocity field shown in Fig. 57 corresponds to the actual failure mode for a clay with E/C = 100.

6.5 Some Comments on the Numerical Solutions

In this section we discuss the adequacy of the increment size used in the various solutions, the accuracy of the solutions with respect to satisfaction of the discrete equilibrium equations, and

finally element stresses are discussed.

Increment Size

When an incremental integration scheme is utilized, there is always a question as to the adequacy of the increment size. Referring to Figs. 35, 36 and 37, it can be seen that about twice as many increments were used for a friction angle of 10 degrees as were used for friction angles of 20 and 30 degrees. In particular, 48 increments were used for $\varphi = 10^{\circ}$. This problem was originally solved using about half as many increments, however, near the small deformation limit load, the large deformation solution behaved somewhat erratically. For this reason both the large and small deformation curves were recomputed using a smaller increment size. The small deformation curves were virtually the same for both increment sizes with the smaller increment size giving a 1 percent reduction in the numerical limit load. The large deformation curves were the same except near the limit load where the smaller increment gave a smoother response.

As further evidence of the adequacy of the increment sizes used, the small deformation solution for $\varphi = 20^{\circ}$ (Fig. 36), the large deformation solution for $\varphi = 30^{\circ}$ (Fig. 37), and the small deformation undrained solution (Fig. 49) were all recomputed using half the original increment size. Although in all three cases the smaller increment size produced a smoother load displacement curve, damping the oscillations mentioned previously, the two solutions were essentially the same. We can thus conclude that any error in the solutions can

be ascribed to the finite element discretization rather than to the integration scheme.

Accuracy of the Solutions

In each increment two sets of linear simultaneous equations must be solved. As the footing load approaches the limit load we can expect these simultaneous equations to become somewhat illposed since at the limit load of the discretized body the tangent stiffness is singular. We thus need some measure of the accuracy of the linear equation solutions and herein two checks were used.

At the end of each increment the incremental displacements are substituted back into the mid-increment equations and a residual vector, R, is computed as follows,

$$\{R\} = [K]\{V\} - \{P\} \tag{128}$$

Of course, for an exact solution the residual vector is identically zero. For all the solutions presented here and for each increment of those solutions, every residual vector component was less than .005 lb.

After the last increment of every solution, overall equilibrium of the soil stratum was checked, that is, all of the external forces (including constraint forces) were summed. For all of the solutions presented here both the vertical and horizontal components of this sum were less than .002 lb.

Element Stresses

As discussed previously, stresses in constant strain triangles often exhibit sharp jumps between adjacent elements. This tendency appears to be even more pronounced in elastic-plastic solutions than in elastic solutions. Stress jumps were found to be greatest in the undrained analysis where element stresses oscillated between tension and compression near the footing corner at the higher loads. It should be noted however the nodal stresses were reasonably smooth at all load levels.

7. SUMMARY, CONCLUSIONS AND RECOMMENDATIONS

7.1 Summary

We have discussed here two elastic-plastic soil models; the perfectly plastic Drucker-Prager model and the isotropic strain hardening model of Roscoe and Burland. An explicit incremental constitutive matrix was presented for the Drucker-Prager model and an indicial expression for the Roscoe-Burland constitutive tensor (suitable for numerical analysis) was presented. We have also presented a "mixed" incremental formulation of the large deformation problem. It was found that in order to render the associated finite element equations symmetric, it was necessary to assume incremental strains to be an order of magnitude smaller than incremental rotations. In Chap. 4 we reviewed integration techniques suitable for elastic-plastic analysis and discussed the mid-point integration rule.

A number of example problems were considered in Chap. 5, including a shallow layer of undrained clay under uniform strip loading and a notched tensile specimen. Finally in Chap. 6 total stress and effective stress solutions for 50 ft. deep elastic-plastic clay strata loaded by a rigid strip footing were presented, with particular attention given to the affect of large deformations on the solutions.

7.2 Conclusions

Numerical Techniques

It was shown in Chap. 5 that for a given set of nodal points,

the elastic-plastic solution is significantly influenced by the element arrangement. Of the three arrangements considered, the division of quadrilaterals into four triangles gave, as expected, the best results. These conclusions are, of course, meaningful only for the constant strain triangles used here.

It appears that a fairly fine finite element mesh is needed to capture limit loads. However the finite element method is clearly capable of predicting limit loads to within small tolerances as evidenced by the solutions for the shallow clay layer and the notched tensile specimen. In the context of the Drucker-Prager model, it seems that the higher the friction angle, the finer the mesh must be in order to determine limit loads to within a specified error. It was also demonstrated in Chap. 6 that mesh 3 (Fig. 29) is fine enough to capture the elastic solution for the 50 ft. stratum.

The numerical integration scheme utilized here was shown, in Chaps. 5 and 6, to be relatively insensitive to increment size. It was further indicated in Chap. 6 that the increment sizes used for the 50 ft. stratum examples were adequate. It was demonstrated in Chap. 5 that in the context of large displacement analysis, the equilibrium correction technique is a powerful numerical tool. In addition it was demonstrated that stress scaling with equilibrium correction is an efficient numerical technique in elastic-plastic analysis.

Large Deformation vs. Small Deformation Analysis

For realistic values of effective stress parameters for

overconsolidated clay, changes in geometry caused by deformation of the soil is such as to affect the load-displacement response only near the limit load. For reasonable values of undrained clay parameters (E/C = 1000), soil deformation has practically no effect on the load-displacement response of a footing, even near the limit load. In such a case, small deformation analysis neglecting the changes in geometry is sufficient for an elastic-plastic analysis. For the extreme value of E/C = 100, clay response is affected near the limit load. For reasonable values of both drained overconsolidated parameters and undrained parameters, the small displacement limit load is a meaningful measure of the load at which footing displacements become excessive.

Clearly for practical settlement calculations a small deformation analysis is sufficient for the total and effective stress parameters considered here. Depending on the precision required, a linear analysis may, in fact, be suitable for practical settlement analysis. This is particularly true for undrained analysis where a significant portion of the load settlement curve is nearly linear.

Deformation Modes at the Limit State

For some time there has been a question as to the true velocity field at incipient collapse or plastic limit state for a smooth punch bearing on a perfectly plastic, weightless von Mises or Tresca material (plane strain). The results presented here indicate that the actual field is a combination of both the Hill and Prandtl velocity fields, a possibility suggested by Prager and

Hodge (55). For a smooth punch bearing on an extended von Mises (Drucker-Prager) weightless material, it was determined here that the actual failure mode contains elements of both the Prandtl and Hill velocity fields.

For both the von Mises and extended von Mises yield functions, we have demonstrated that the Prandtl velocity field corresponds to the actual mode of failure for a perfectly rough punch bearing on a weightless material.

7.3 Recommendations for Future Work

It is recommended that the analyses presented here be extended to subsurface footings. Furthermore, the effective stress analyses of normally consolidated clay strata and the analyses of sand strata constitute a natural extension of the work presented here. Although the Drucker-Prager model with $k = 0$ is directly applicable to these soils, some preliminary analyses by the author yielded very poor results. It may well be that finer finite element meshes and a different numerical integration scheme are required for such materials.

Although some analyses using Cambridge type strain hardening models (64) have been briefly reported in the literature (71)(82)(83), it is felt that more extensive studies using these models could be extremely interesting.

Since strain softening is characteristic of many natural soils, analyses using strain softening stress-strain models would be extremely enlightening. In particular the effect of strain softening

on the maximum load should be investigated. This kind of work is particularly necessary for sensitive clays which exhibit dramatic softening. Hoeg (34) and Zienkiewicz and Nayak (81) have done some preliminary work in this area.

Table 1 Elastic Contact Stresses Beneath Rough Rigid Footing

$q = 10{,}000$ psf, $\nu = .3$

Distance from Centerline ft.	σ_x (psf)		σ_y (psf)	
	Halfspace (Exact)	Finite Element	Halfspace (Exact)	Finite Element
0	2,850	2,820	6,640	6,330
.5	2,900	2,910	6,780	6,520
1.0	3,100	3,140	7,230	6,980
1.4	3,410	3,510	7,960	7,710
1.8	4,040	4,120	9,430	9,000
2.1	5,110	5,220	11,930	11,200
2.3	6,950	6,220	16,210	14,650
2.5	---	13,380	---	18,660

Table 2 Elastic Stress Distribution Below Centerline of Rough Rigid Footing, $q = 10{,}000$ psf, $\nu = .3$

Distance Below Footing ft.	σ_x (psf)		σ_y (psf)	
	Halfspace (Exact)	Finite Element	Halfspace (Exact)	Finite Element
0	2850	2820	6640	6330
1.03	3040	2630	6400	6360
2.50	1640	1380	6130	6030
3.90	795	491	5380	5260
5.60	362	140	4440	4400
7.80	158	-36	3510	3490
10.70	67	-102	2710	2630
14.8	27	-68	2030	2060
20.8	10	-51	1480	1520
29.2	4	30	1070	1130
37.4	2	111	837	925
50.0	1	270	629	825

Table 3 Elastic Stress Distribution Below Corner of Rough Rigid Footing, $q = 10{,}000$ psf, $\nu = .3$

Distance Below Footing ft.	σ_x (psf)		σ_y (psf)	
	Halfspace (Exact)	Finite Element	Halfspace (Exact)	Finite Element
0	---	13,380	---	18,660
.2	7480	6770	17,180	17,350
.4	4730	4250	12,340	12,650
.7	3310	2940	9,460	9,470
1.1	2570	2200	7,650	7,750
1.5	2100	1770	6,640	6,610
2.0	1760	1440	5,840	5,790
2.7	1430	1120	5,160	5,110
3.6	1100	816	4,570	4,520
4.7	787	521	4,050	3,990
6.2	505	286	3,520	3,480
8.1	304	92	3,020	2,960
11.0	152	-8	2,450	2,420
15.0	69	-37	1,910	1,950

Table 4 Elastic Contact Stresses Beneath Rough Rigid Footing

q = 10,000 psf

Distance From Centerline ft.	σ_x (psf)			σ_y (psf)		
	Halfspace (Exact) $\nu = .5$	Halfspace (Exact) $\nu = .48$	Finite Element $\nu = .48$	Halfspace (Exact) $\nu = .5$	Halfspace (Exact) $\nu = .48$	Finite Element $\nu = .48$
0	6,370	5,880	5,580	6,370	6,370	6,280
.5	6,500	6,000	5,840	6,500	6,500	6,600
1.0	6,950	6,420	6,370	6,950	6,950	7,040
1.4	7,680	7,100	7,030	7,680	7,690	7,740
1.8	9,170	8,470	8,220	9,170	9,180	8,990
2.1	11,730	10,830	9,780	11,730	11,740	10,990
2.3	16,240	14,990	13,180	16,240	16,240	14,700
2.5	---	---	14,720	---	---	21,670

Table 5 Elastic Stress Distribution Beneath Corner of Rough Rigid Footing, q = 10,000 psf

Distance Below Footing ft.	σ_x (psf)			σ_y (psf)		
	Halfspace (Exact) $\nu = .5$	Halfspace (Exact) $\nu = .48$	Finite Element $\nu = .48$	Halfspace (Exact) $\nu = .5$	Halfspace (Exact) $\nu = .48$	Finite Element $\nu = .48$
0	---	---	14,720	---	---	21,670
.2	5,950	6,130	6,260	17,000	17,220	18,650
.4	4,400	4,430	4,610	12,110	12,240	13,170
.7	3,510	3,480	3,420	9,260	9,340	9,570
1.1	2,930	2,870	2,870	7,520	7,570	7,810
1.5	2,560	2,490	2,420	6,570	6,590	6,670
2.0	2,200	2,140	2,030	5,830	5,840	5,860
2.7	1,800	1,750	1,660	5,210	5,210	5,190
3.6	1,370	1,330	1,280	4,670	4,660	4,630
4.7	960	937	894	4,180	4,170	4,110
6.2	600	587	576	3,660	3,640	3,580
8.1	351	345	384	3,140	3,120	3,070
11.0	171	168	266	2,530	2,520	2,500
15.0	76	75	219	1,960	1,960	1,990

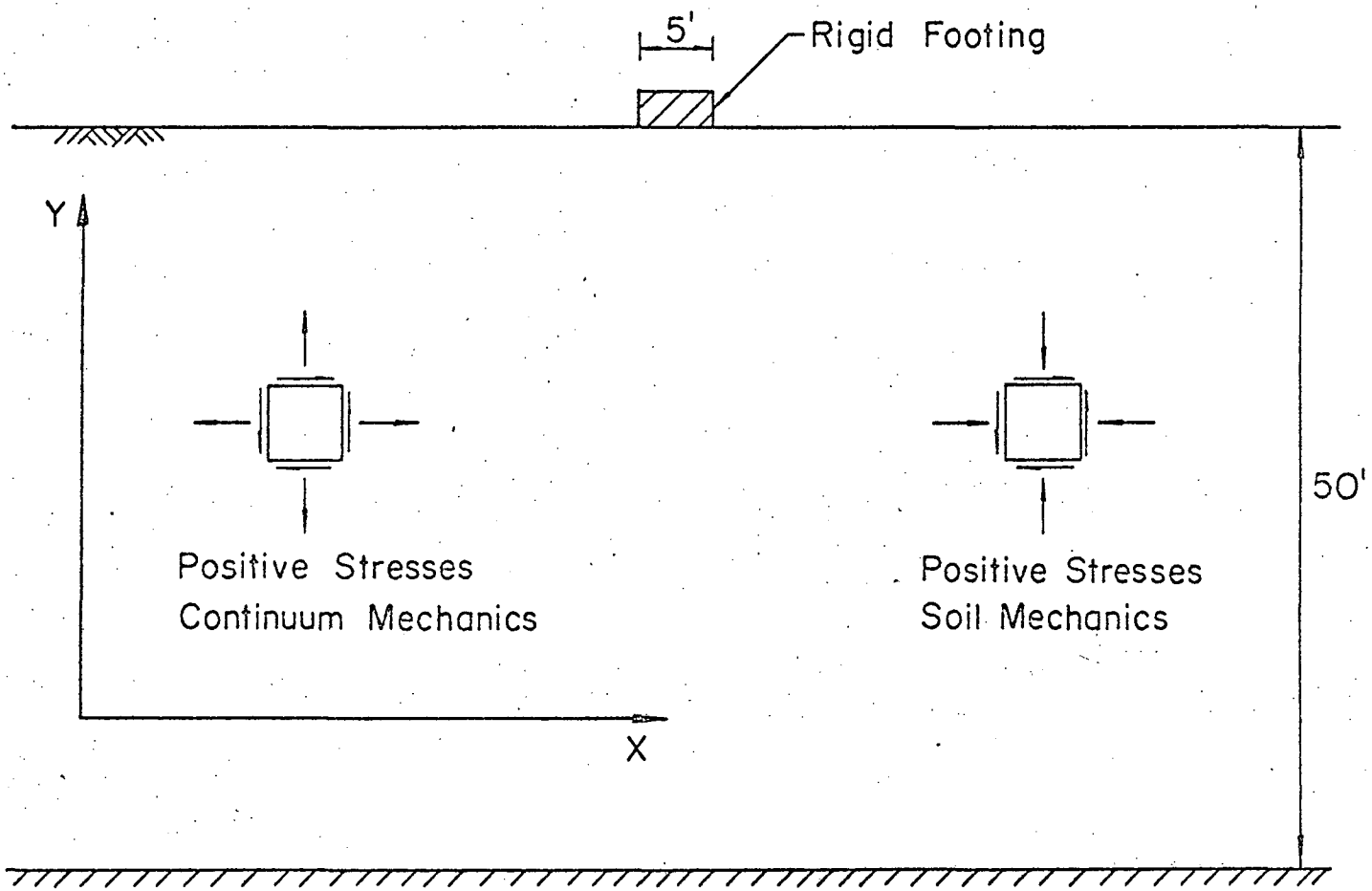

Fig. 1 Clay Stratum Loaded by Footing - Stress Sign Conventions

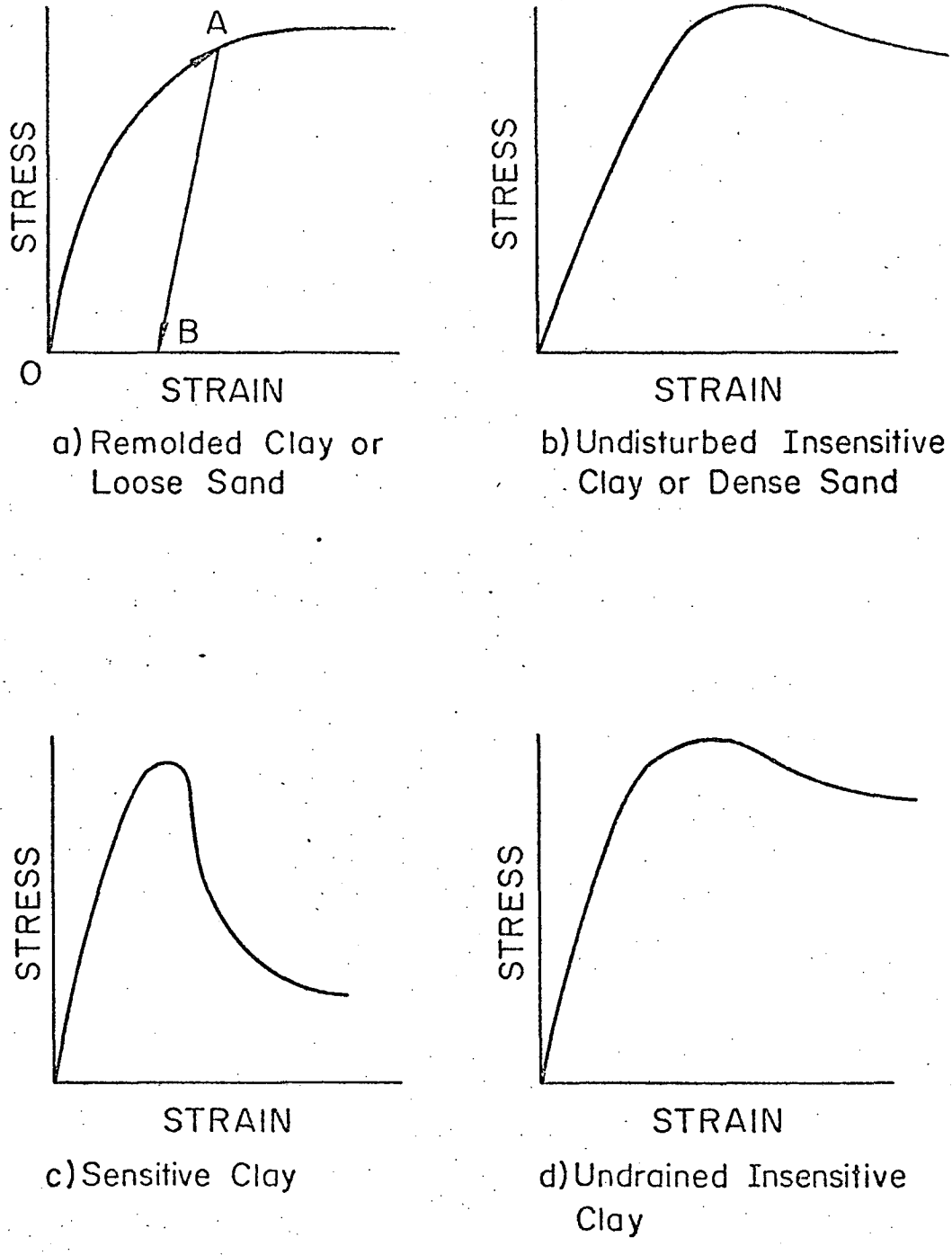

Fig. 2 Typical Soil Stress-Strain Curves

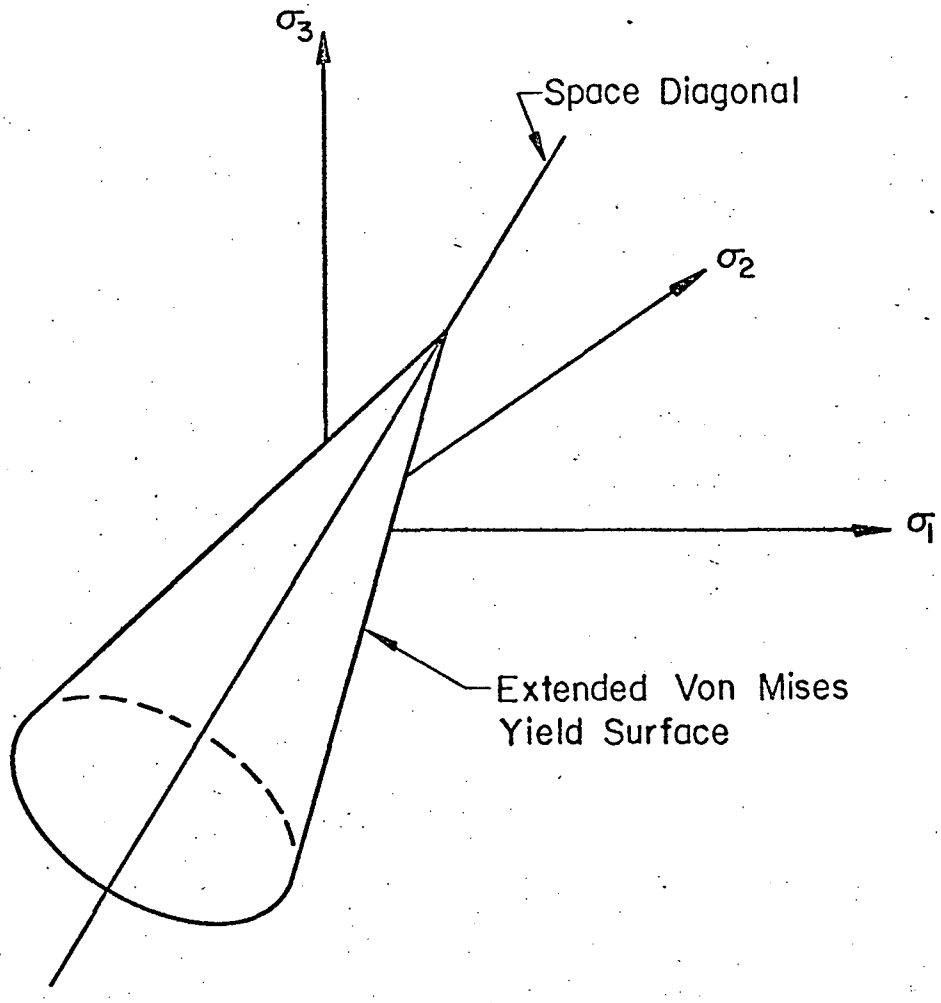

Fig. 3 Extended von Mises Yield Surface in Principal Stress Space

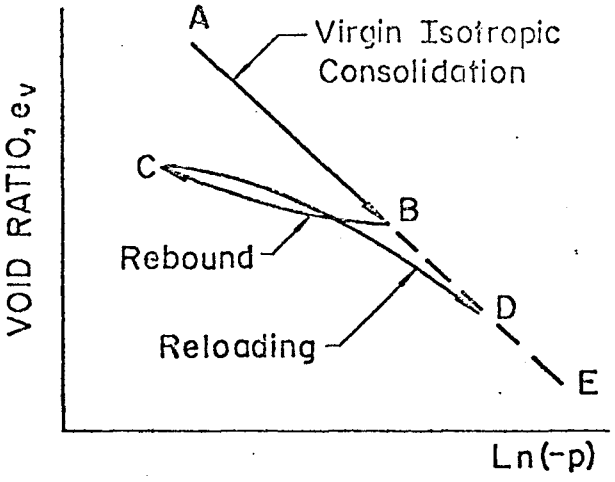

Fig. 4 Response of Real Soil to Hydrostatic Stress

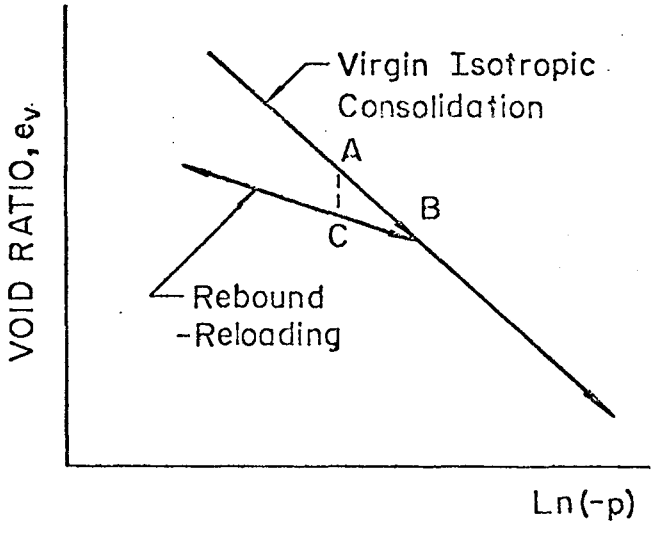

Fig. 5 Response of Idealized Soil to Hydrostatic Stress

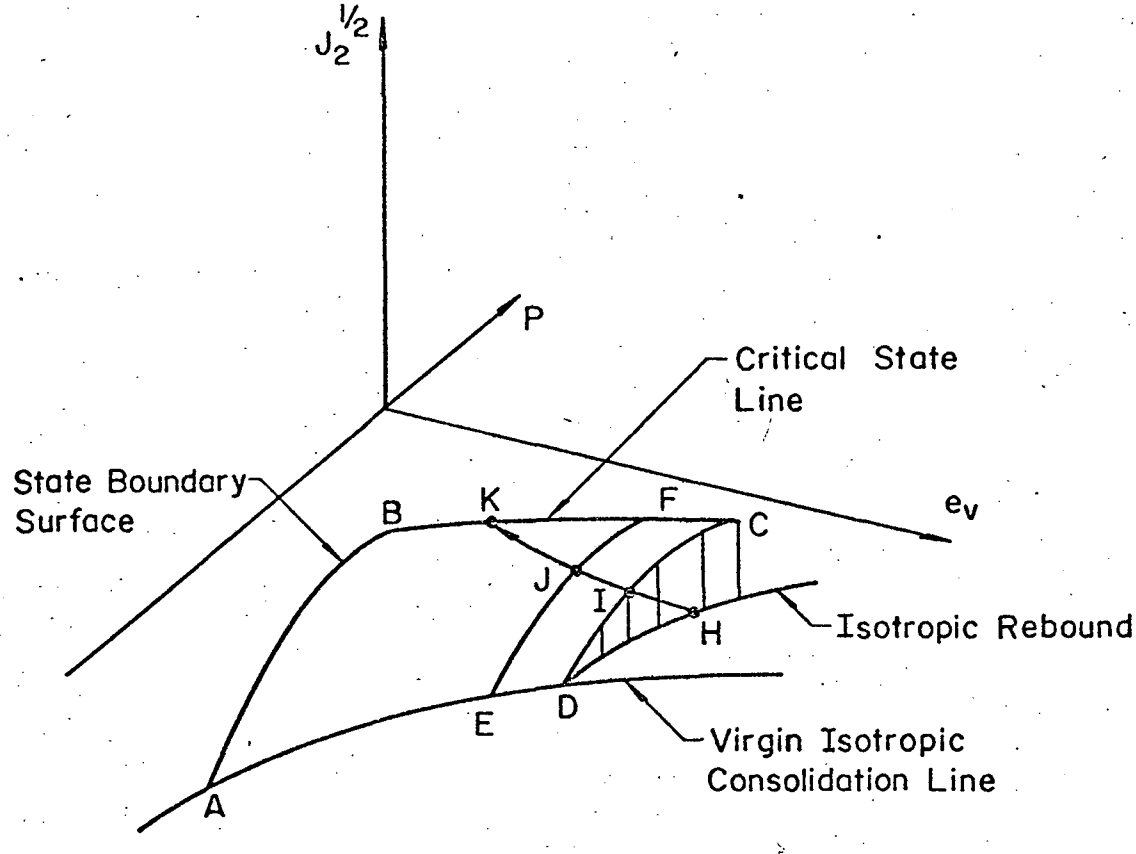

Fig. 6 Part of "State Boundary Surface"

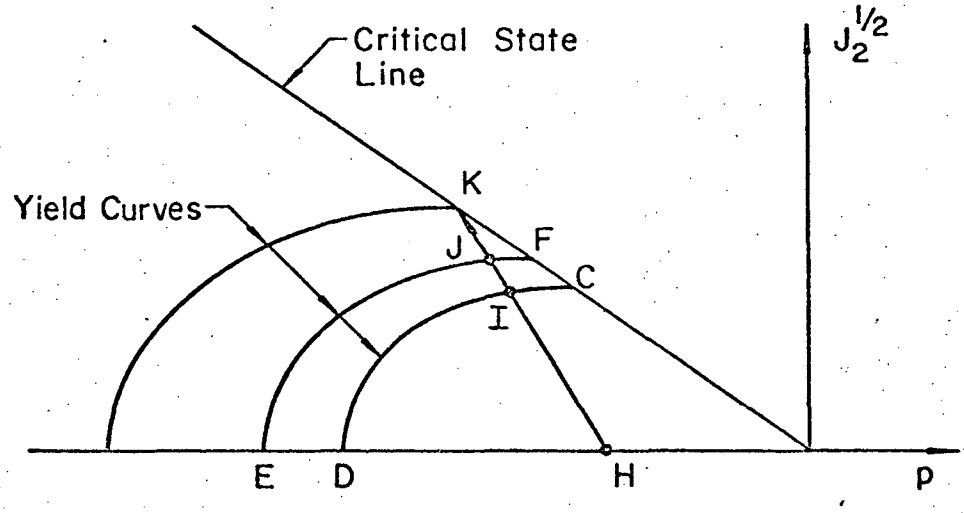

Fig. 7 Stress Path

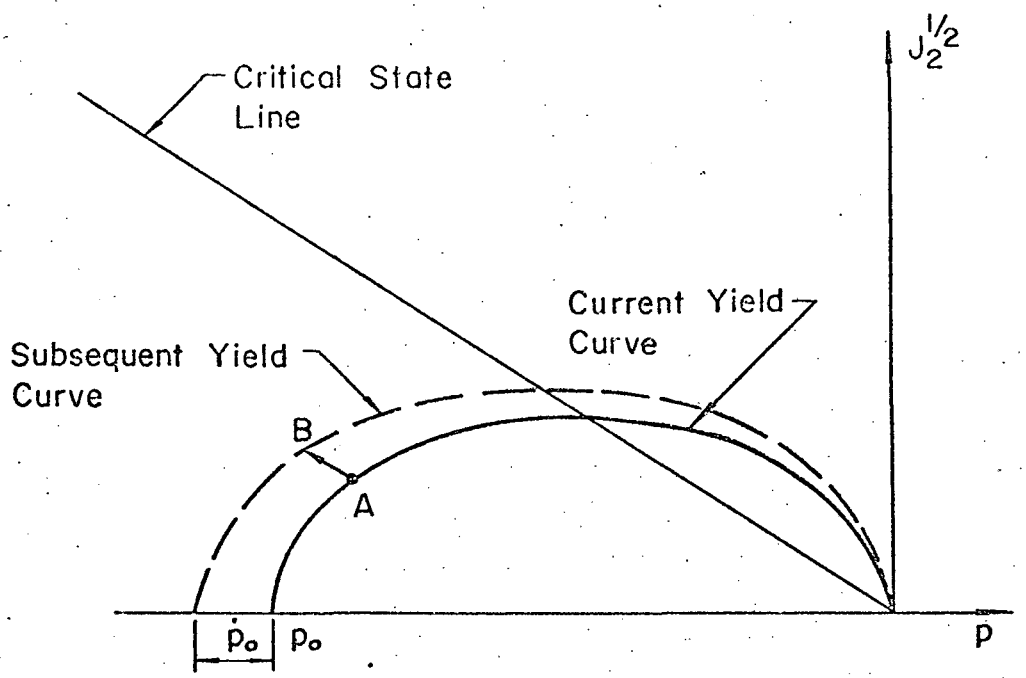

Fig. 8 Modified Cam-Clay Yield Curves

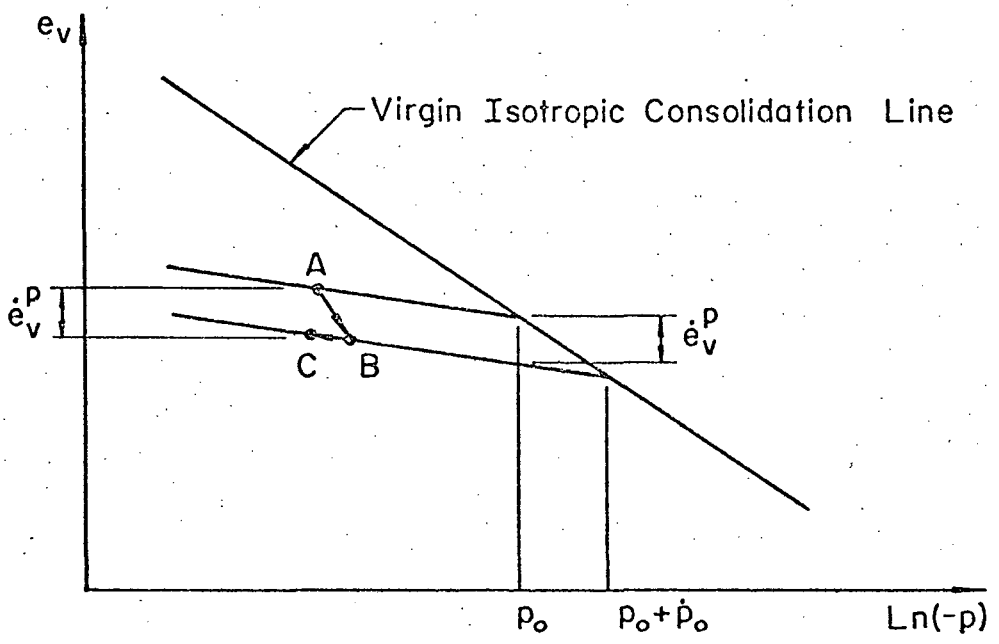

Fig. 9 Relationship Between Strain Hardening Parameter Increment and Void Ratio Increment

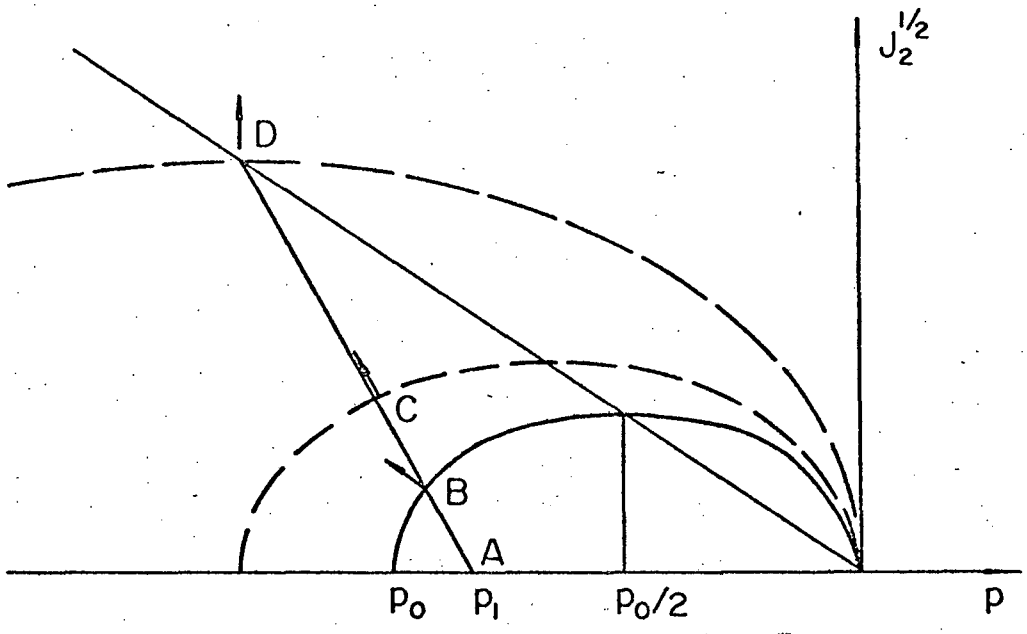

Fig. 10 Strain Hardening Stress Path

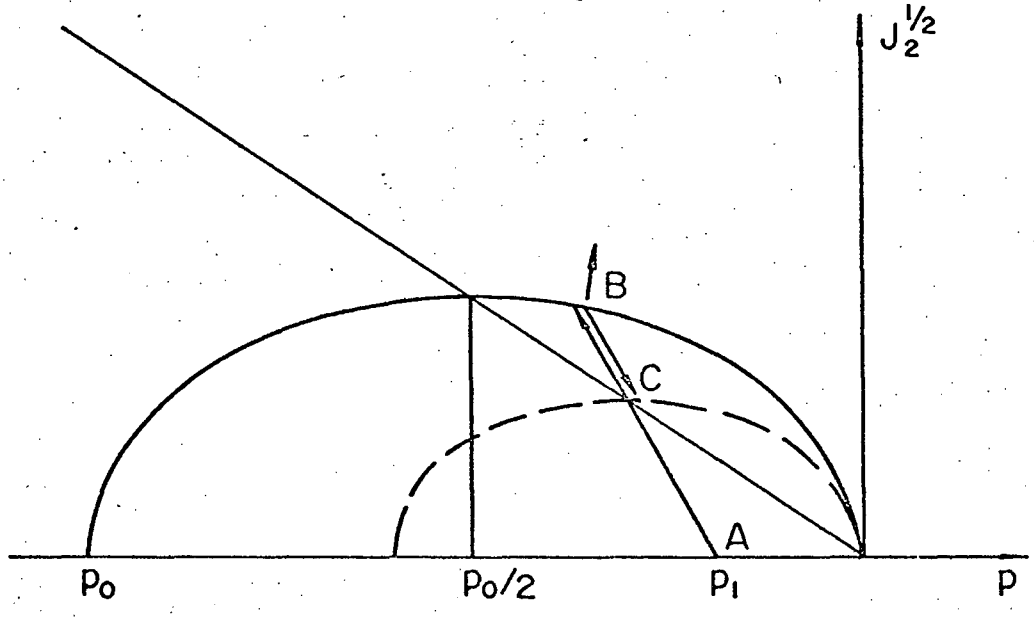

Fig. 11 Strain Softening Stress Path

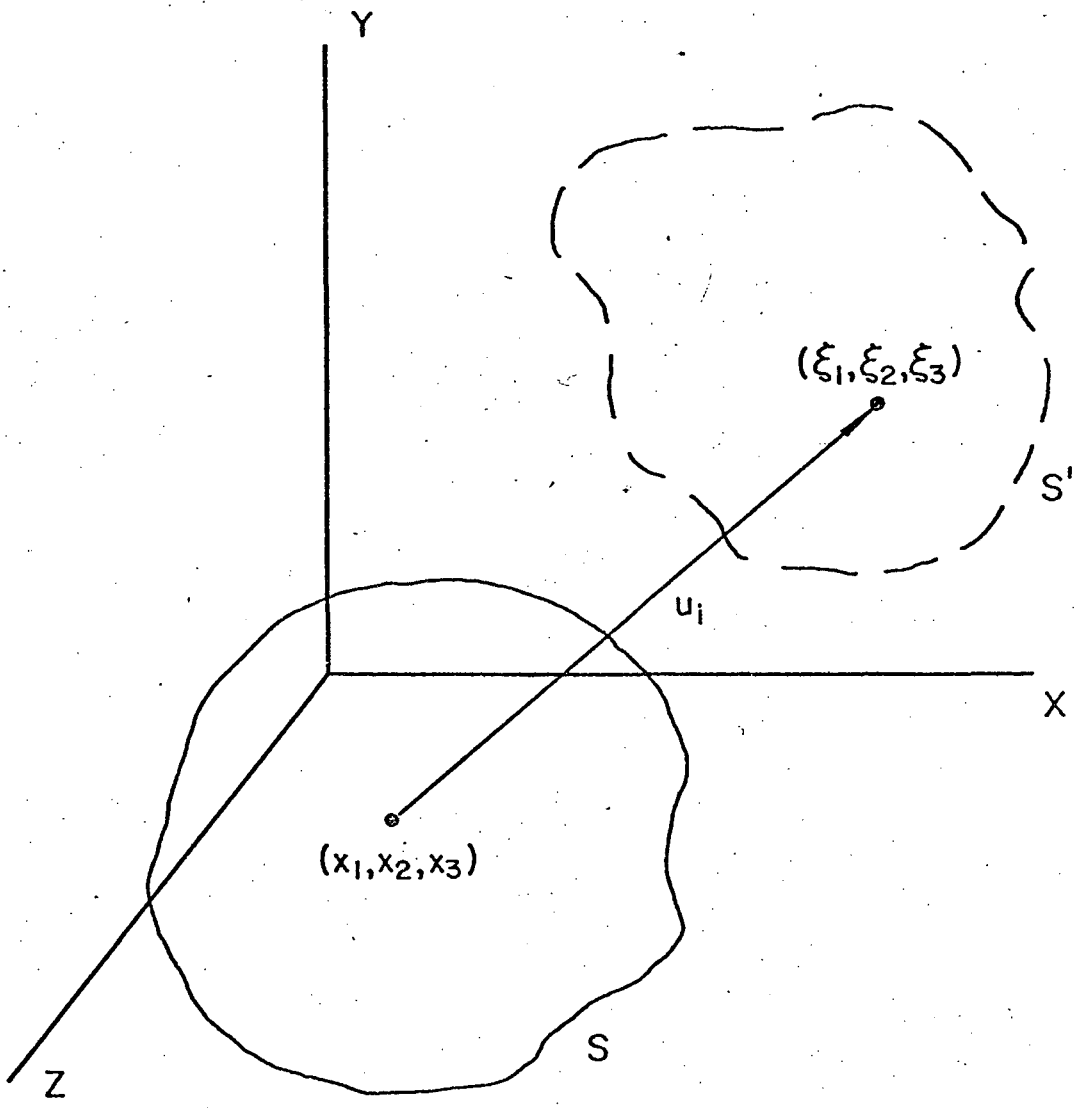

Fig. 12 Initial and Subsequent Configurations

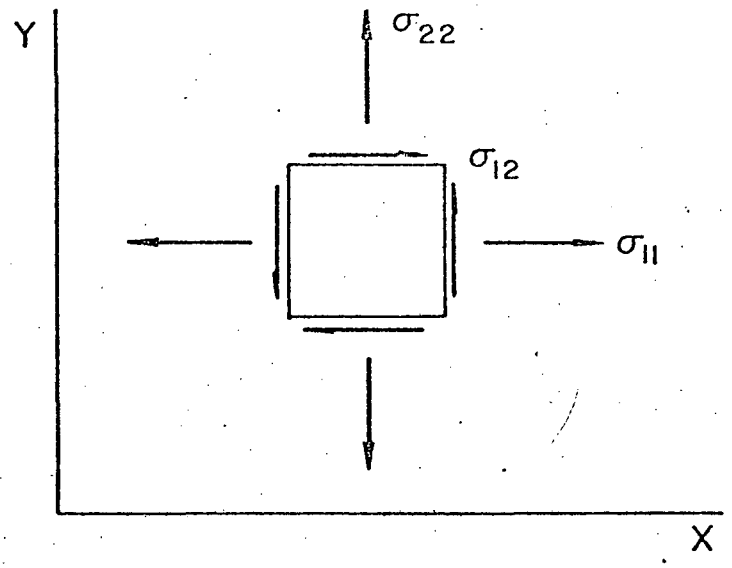

Fig. 13 Stress Components in Initial Configuration

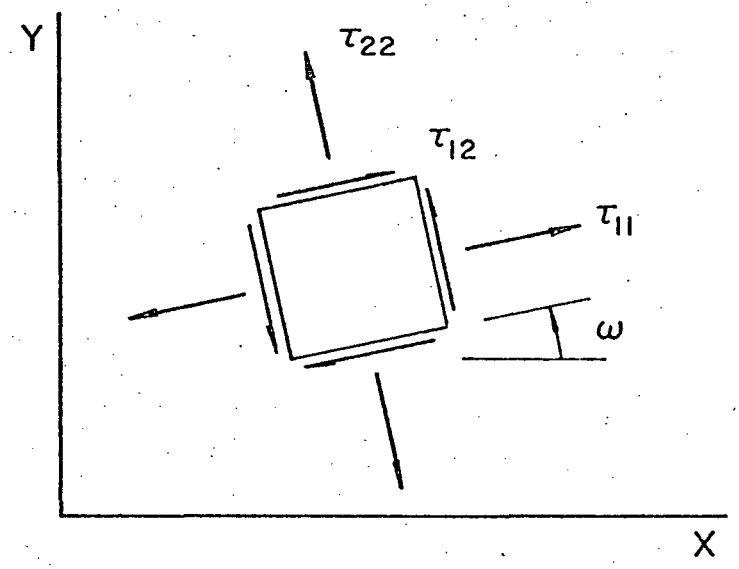

Fig. 14 Locally Defined Stress Components in Subsequent Configuration

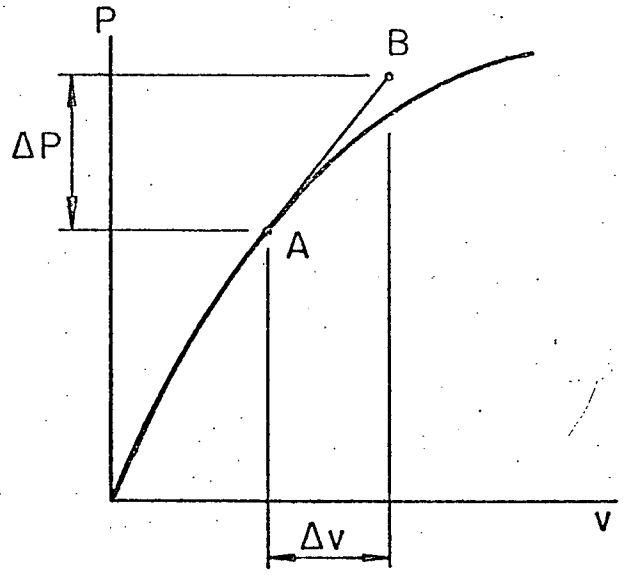

(a) One Euler Increment

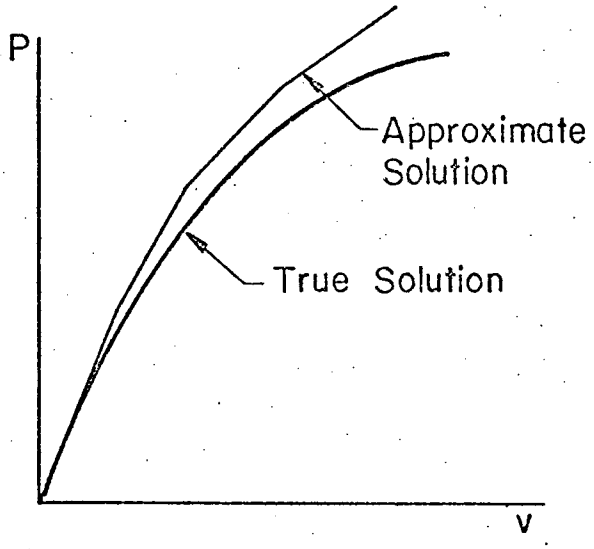

(b) Error Build-Up Associated With Euler Intergration

Fig. 15 Euler Integration

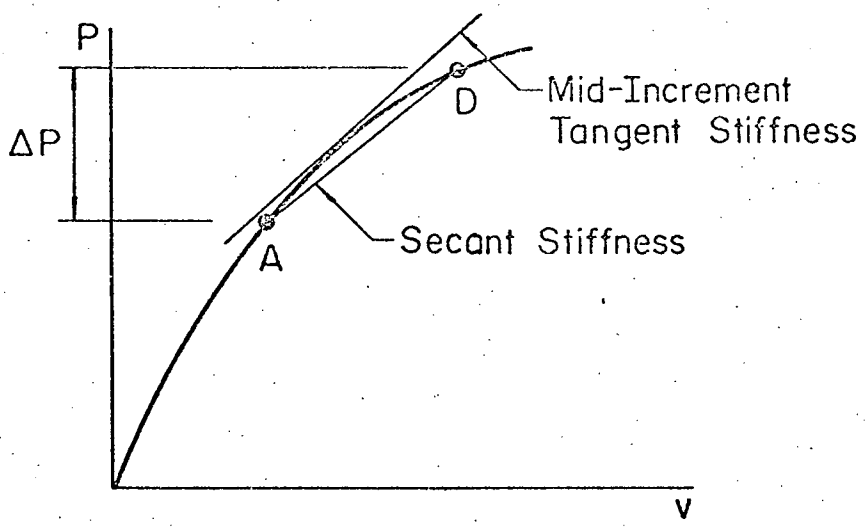

a) Comparison of Mid-Increment Tangent Stiffness and Secant Stiffness

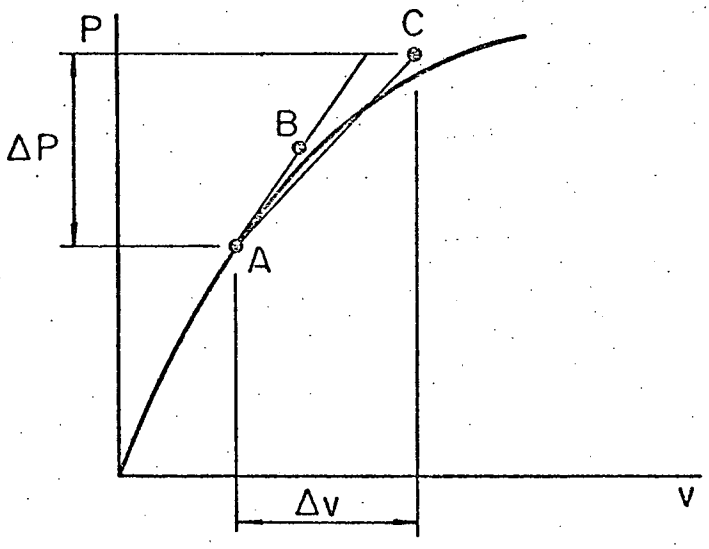

b) One Increment

Fig. 16 Mid-Point Integration Rule

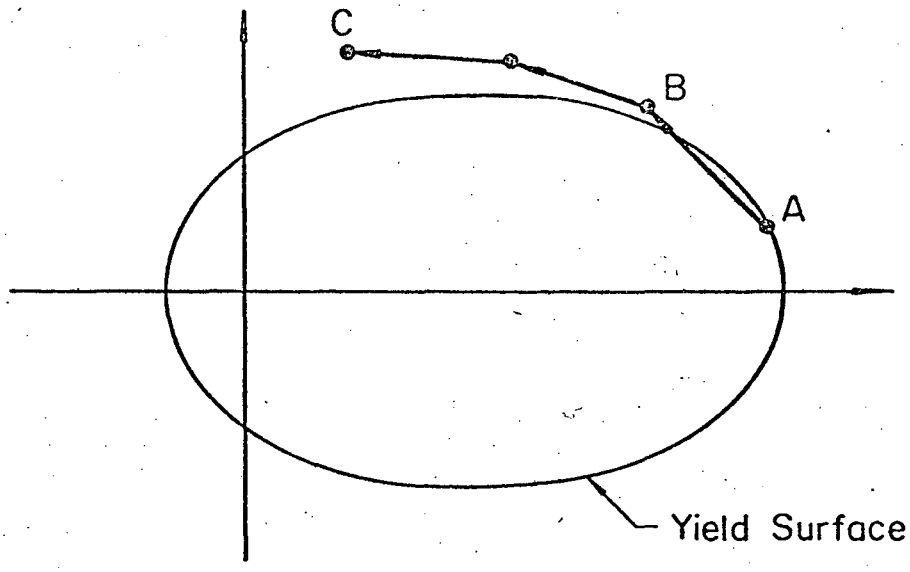

a) Stress Path with no Scaling

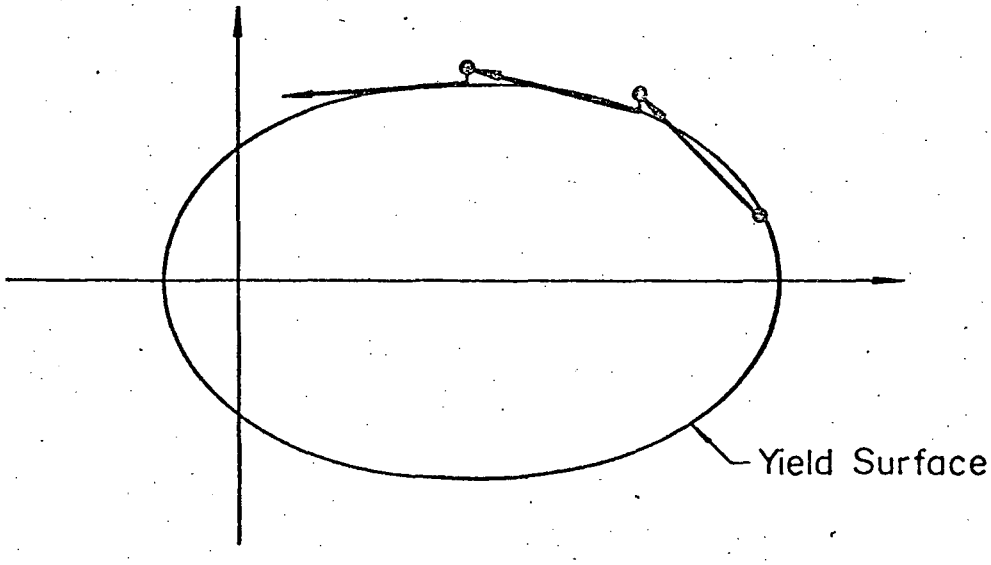

b) Stress Path with Stress Scaling

Fig. 17 Stress Scaling Back to Yield Surface

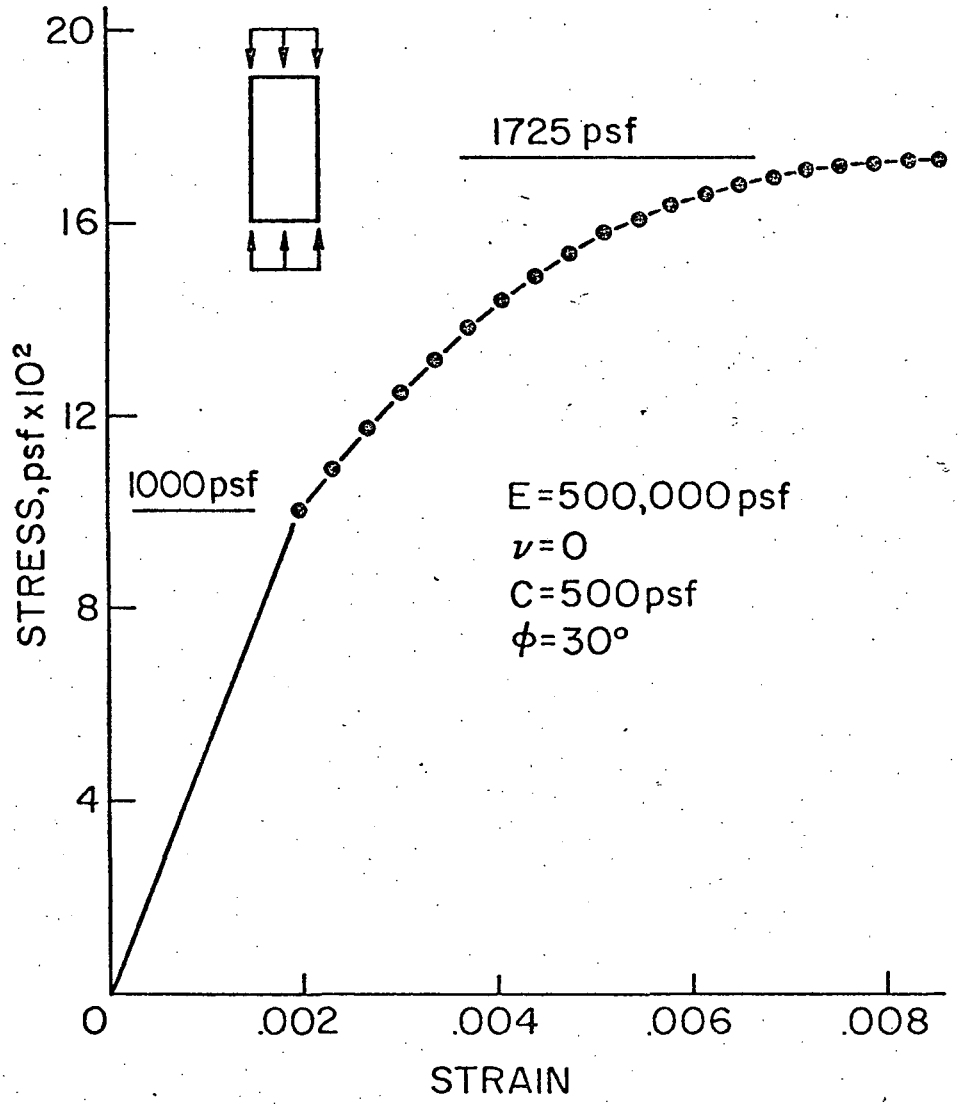

Fig. 18 Uniaxial Stress-Strain Behavior of Drucker-Prager Material (Plane Strain)

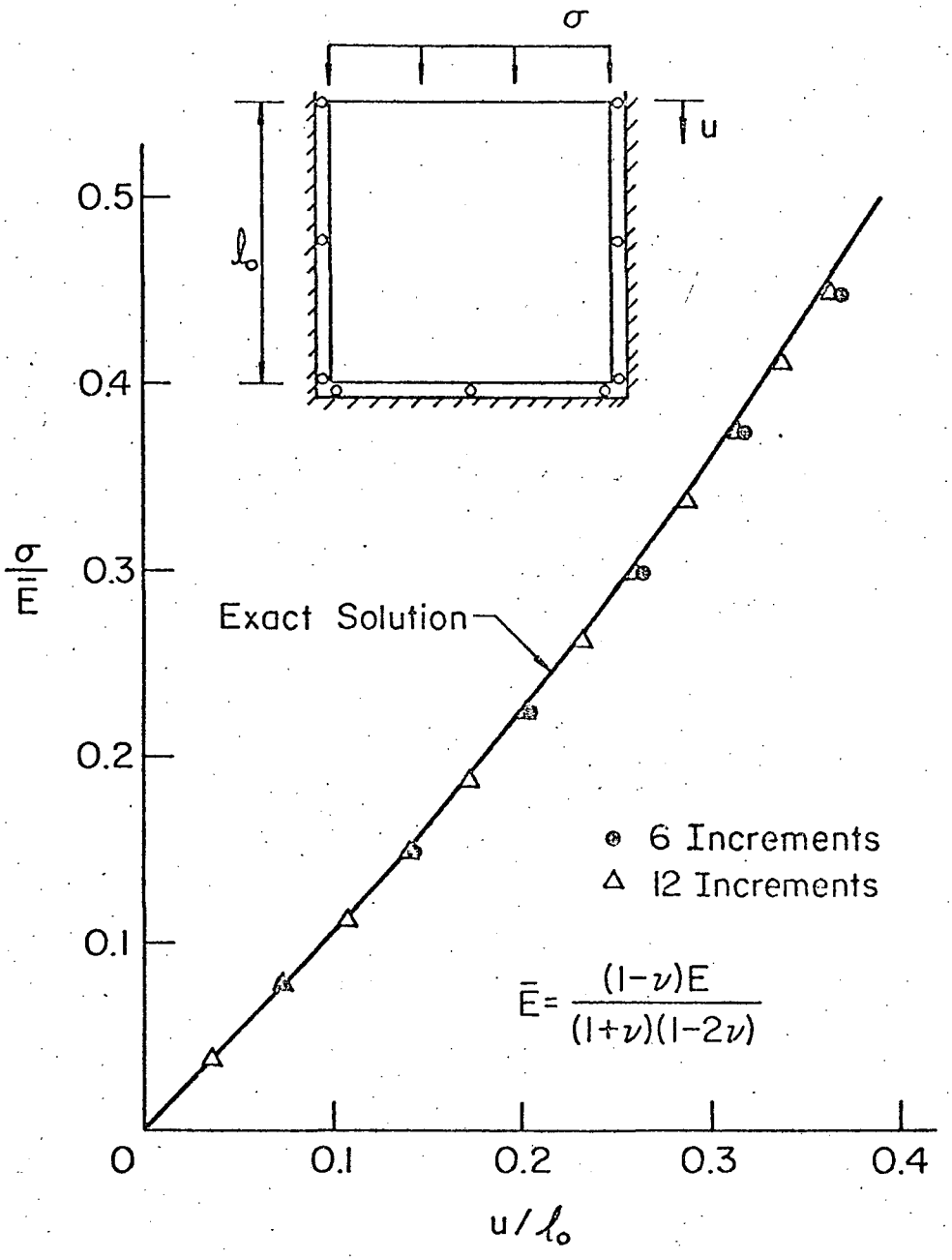

Fig. 19 Uniform Stress, Elastic Large Deformation Problem (Plane Strain)

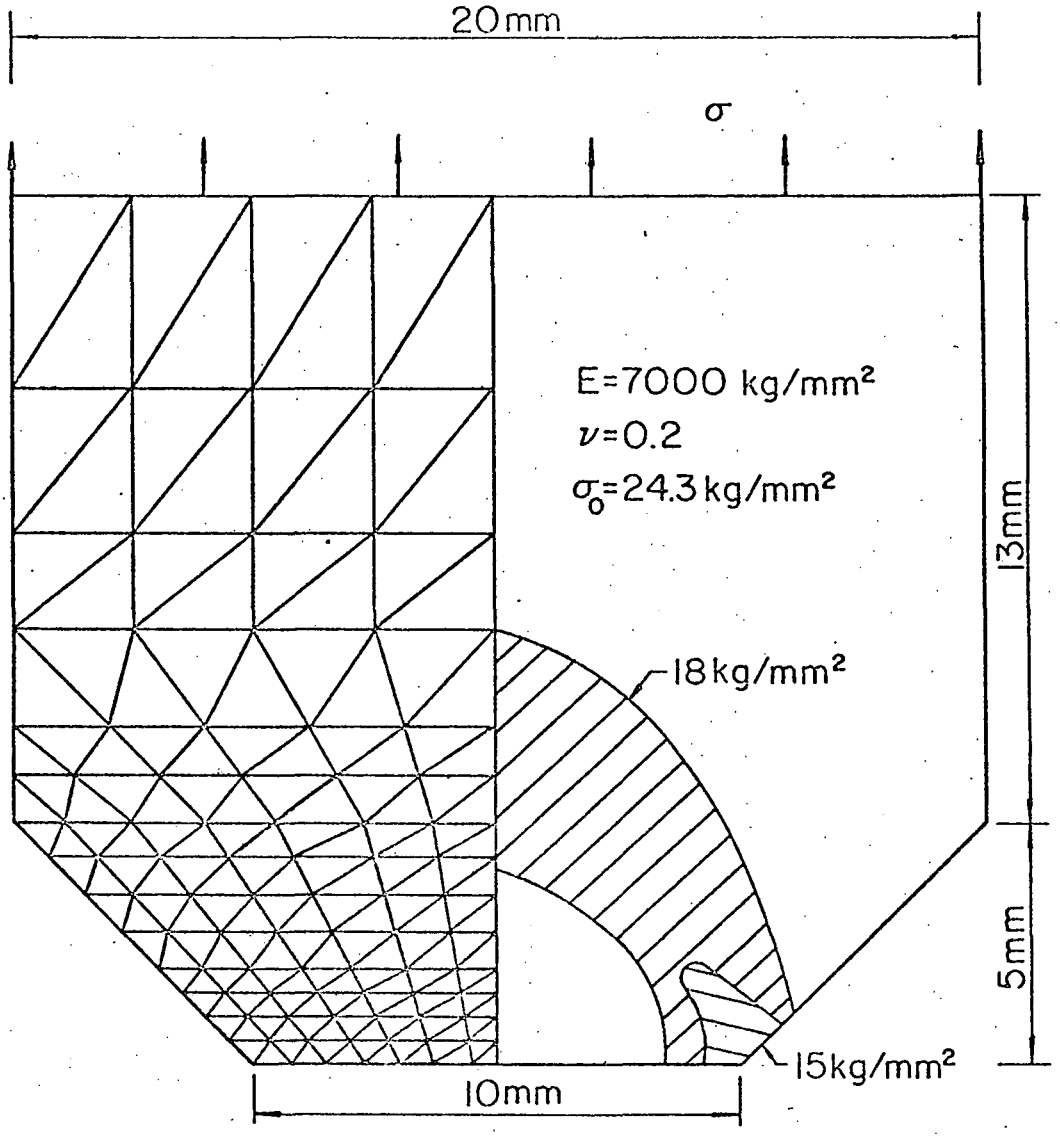

Fig. 20 Plane Strain Notched Tensile Specimen (von Mises Yield Condition)

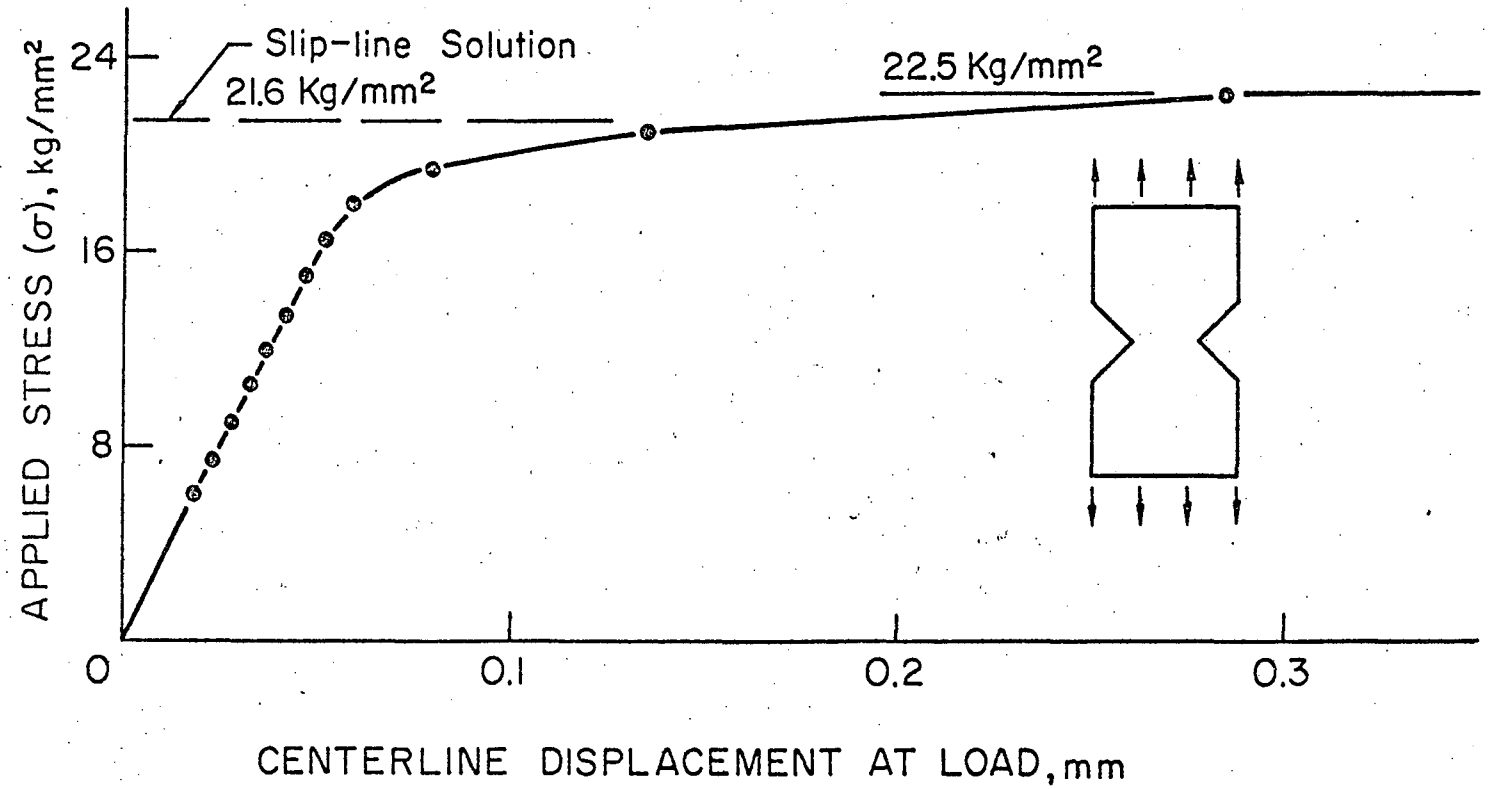

Fig. 21 Load Displacement Curve - Notched Tensile Specimen

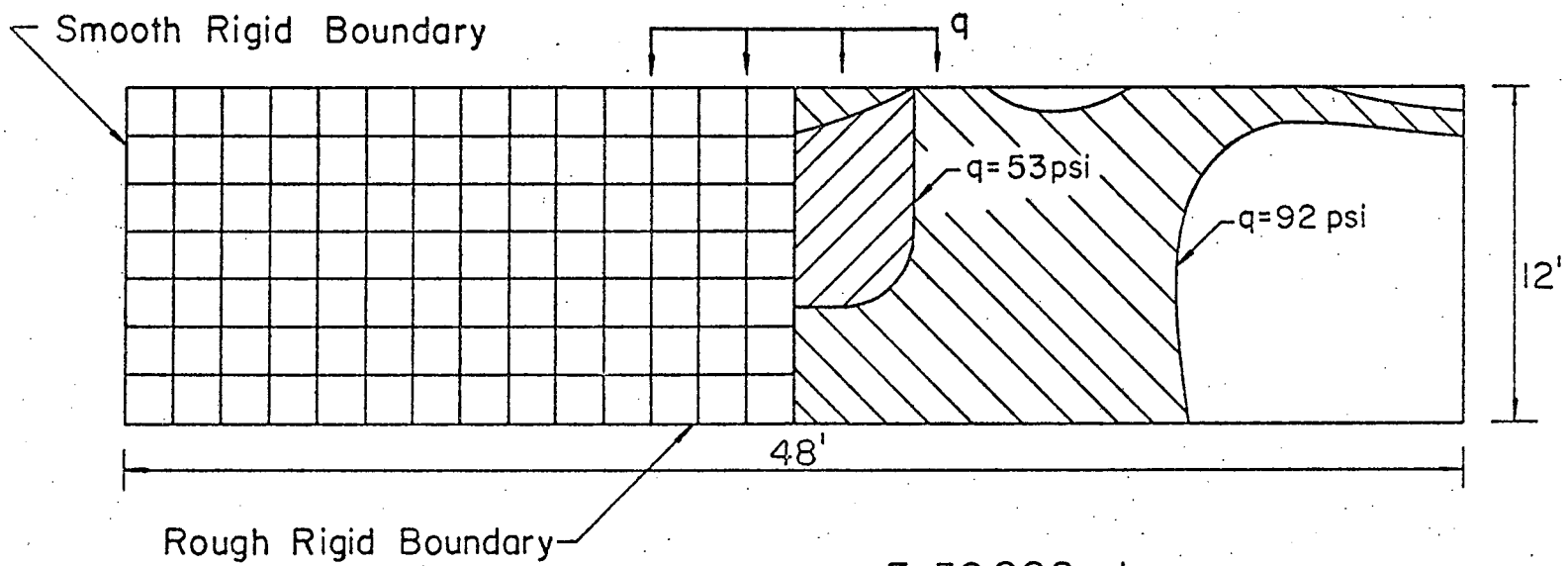

120 Nodes
98 Elements
a)Uniform Rectangular Mesh

E=30,000psi
ν=.3
C=17.5 psi
b) Zones of Yielding

Fig. 22 Shallow Stratum of Undrained Clay

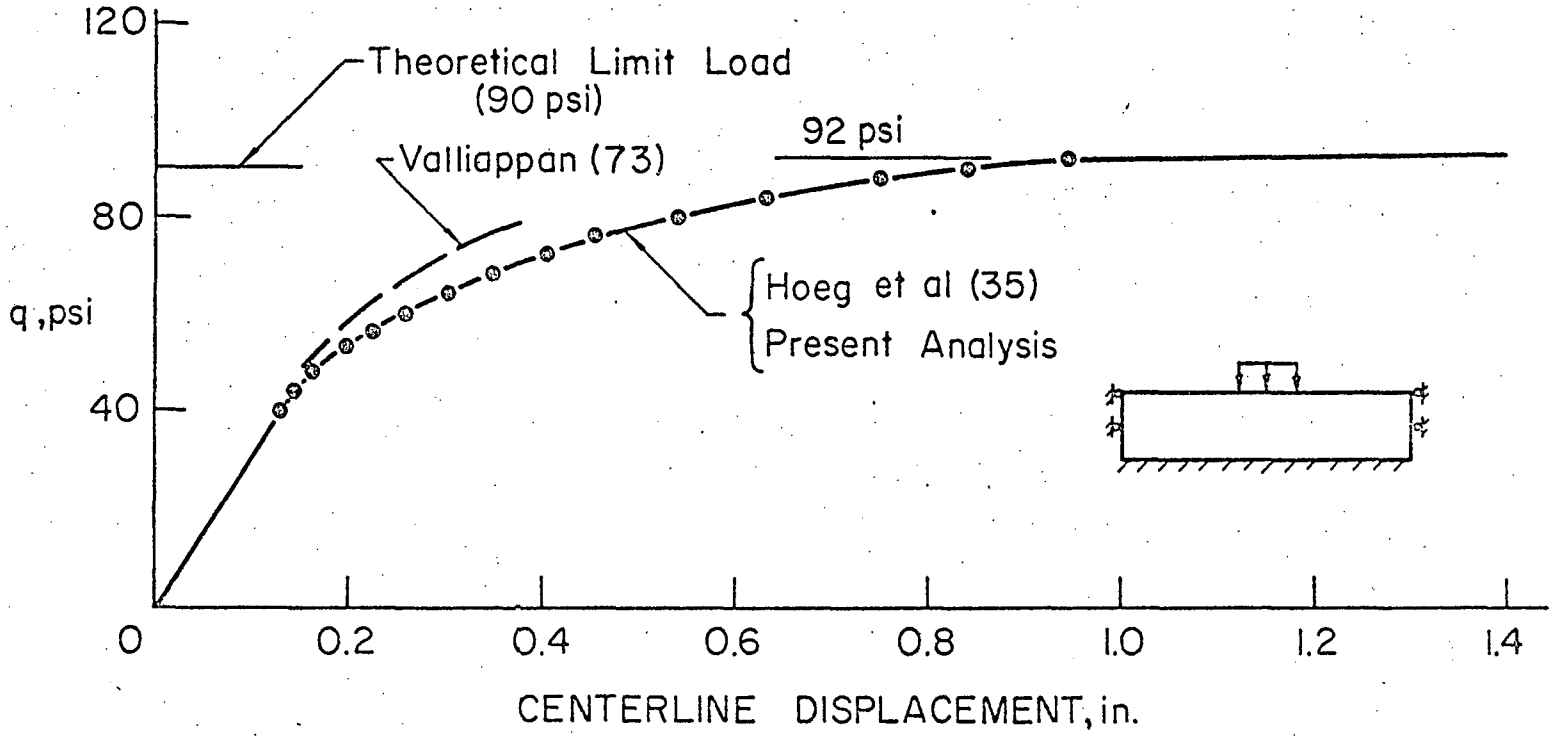

Fig. 23 Load-Displacement Curve for Shallow Undrained Clay Stratum - Uniform Rectangular Mesh (Plane Strain, von Mises Yield Condition)

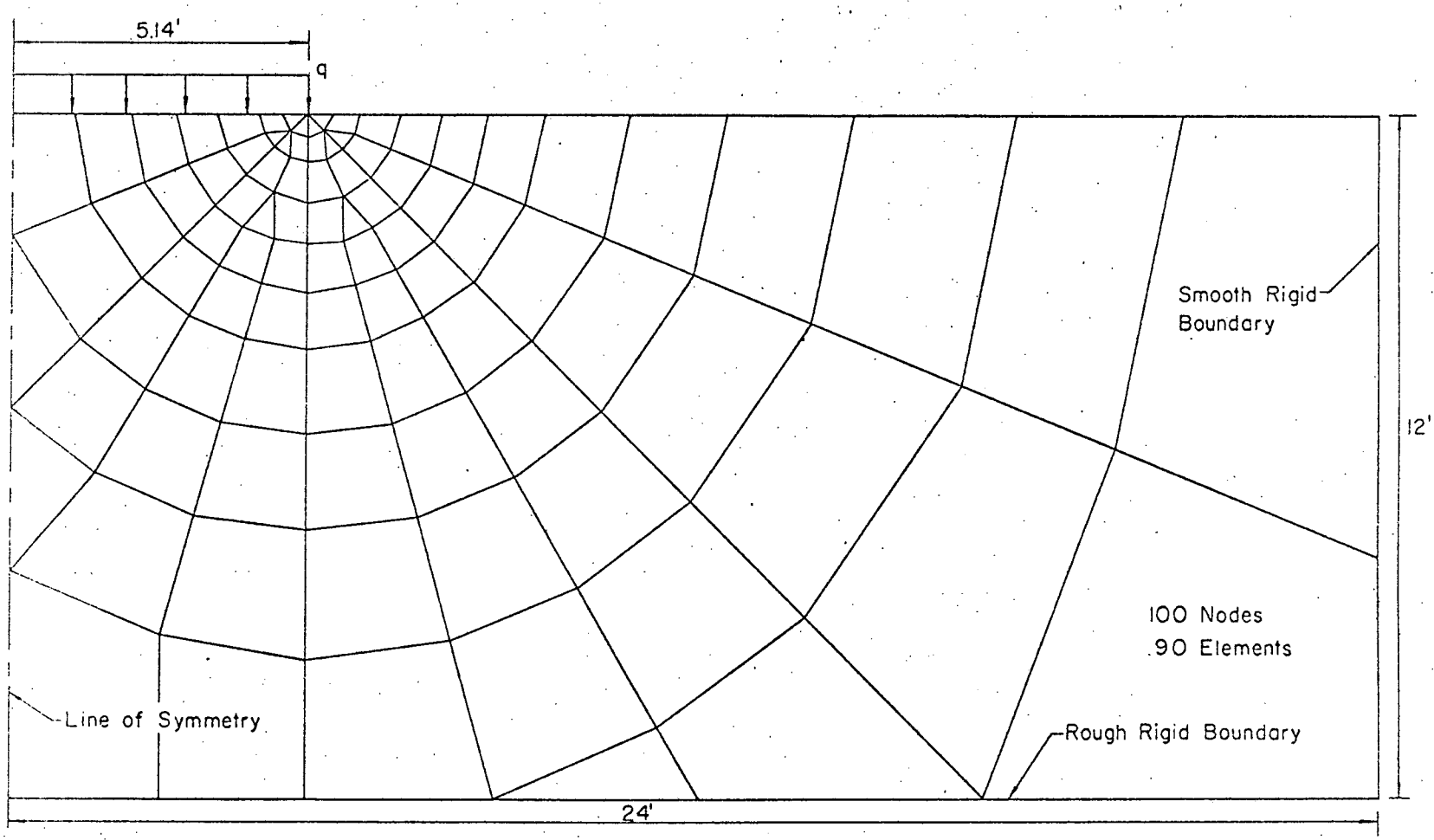

Fig. 24 Nonuniform Mesh for Shallow Undrained Clay Stratum

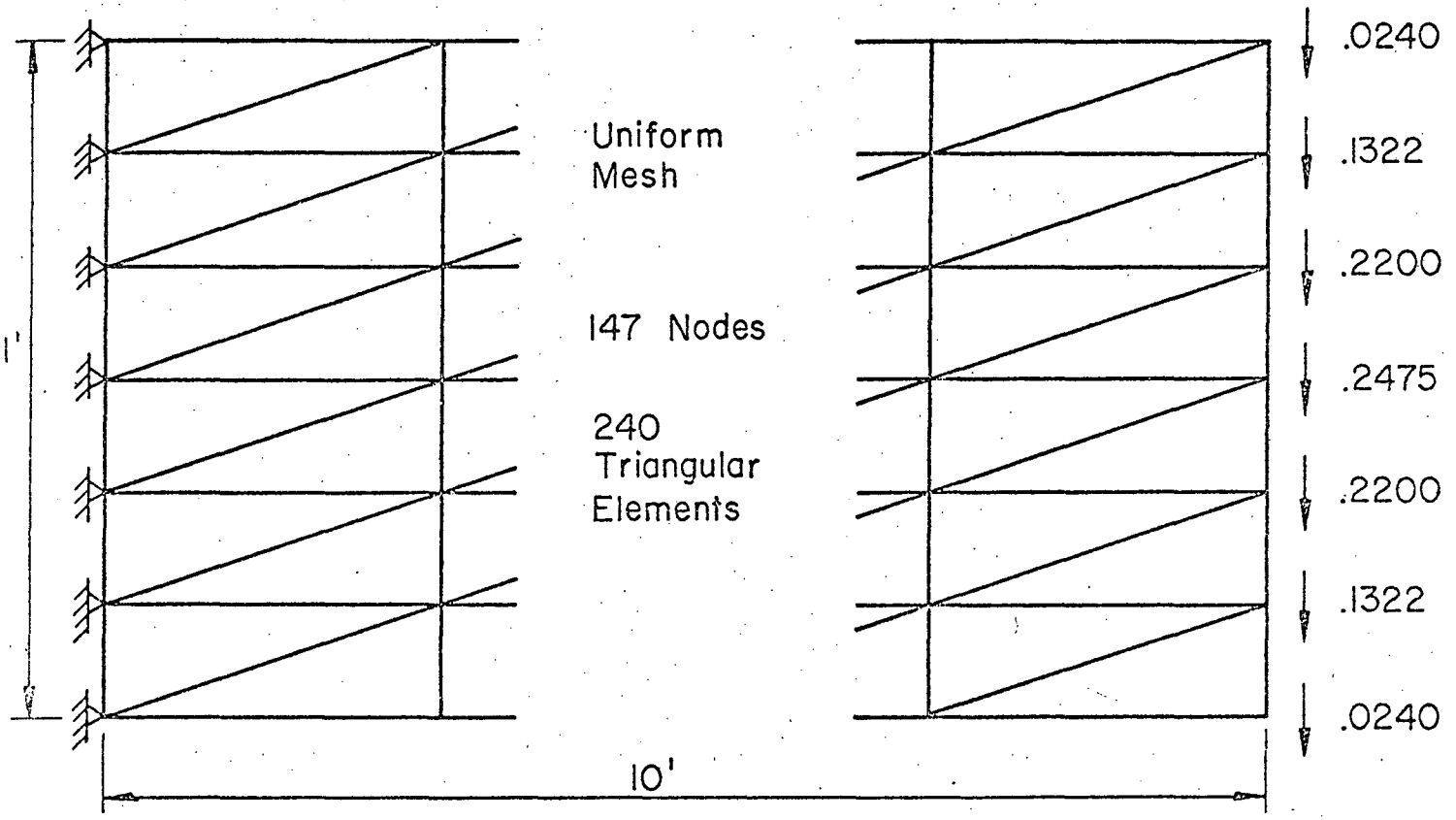

Fig. 25 Finite Element Mesh for Cantilever Beam

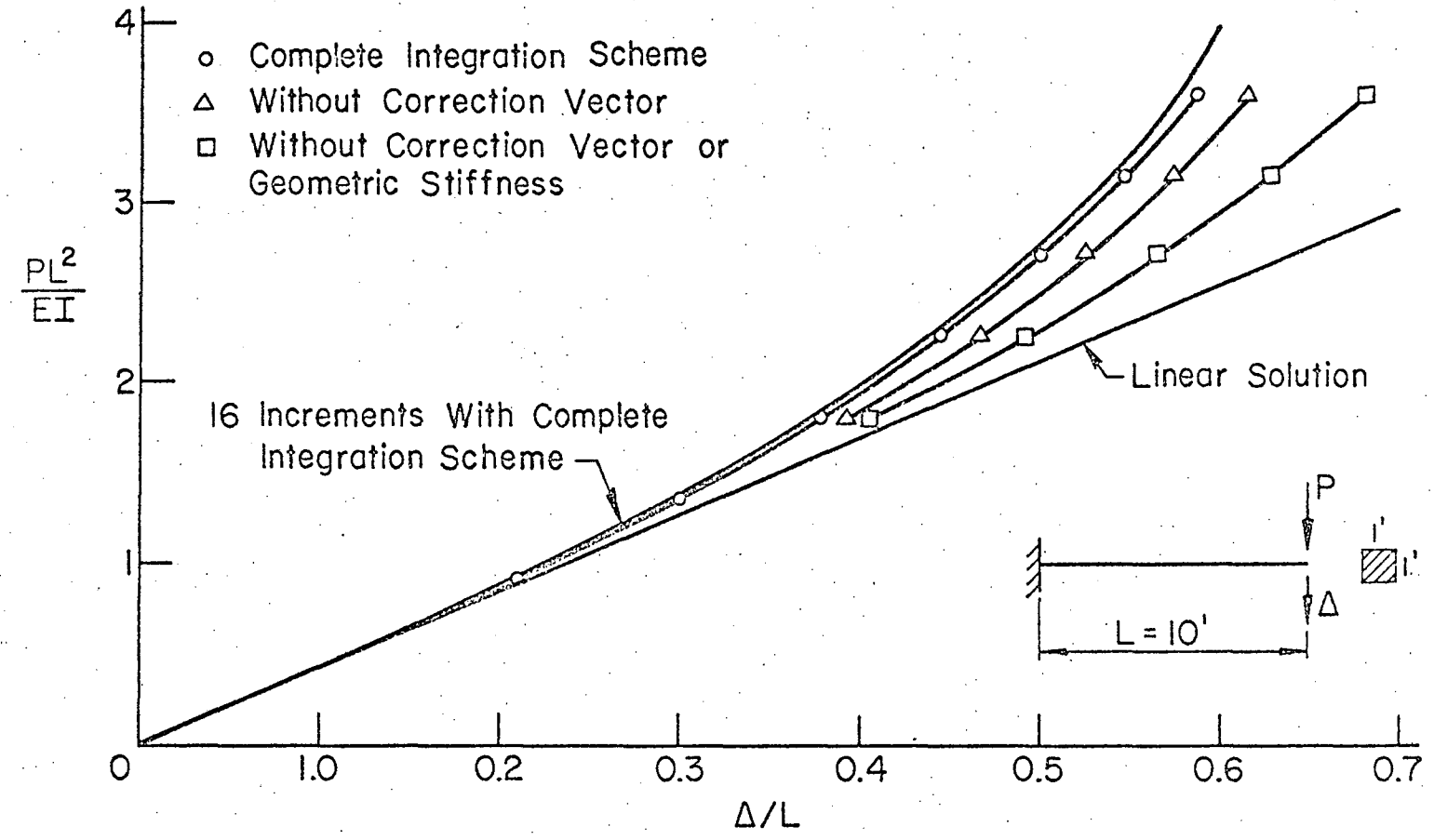

Fig. 26 Elastic Cantilever Beam Solutions

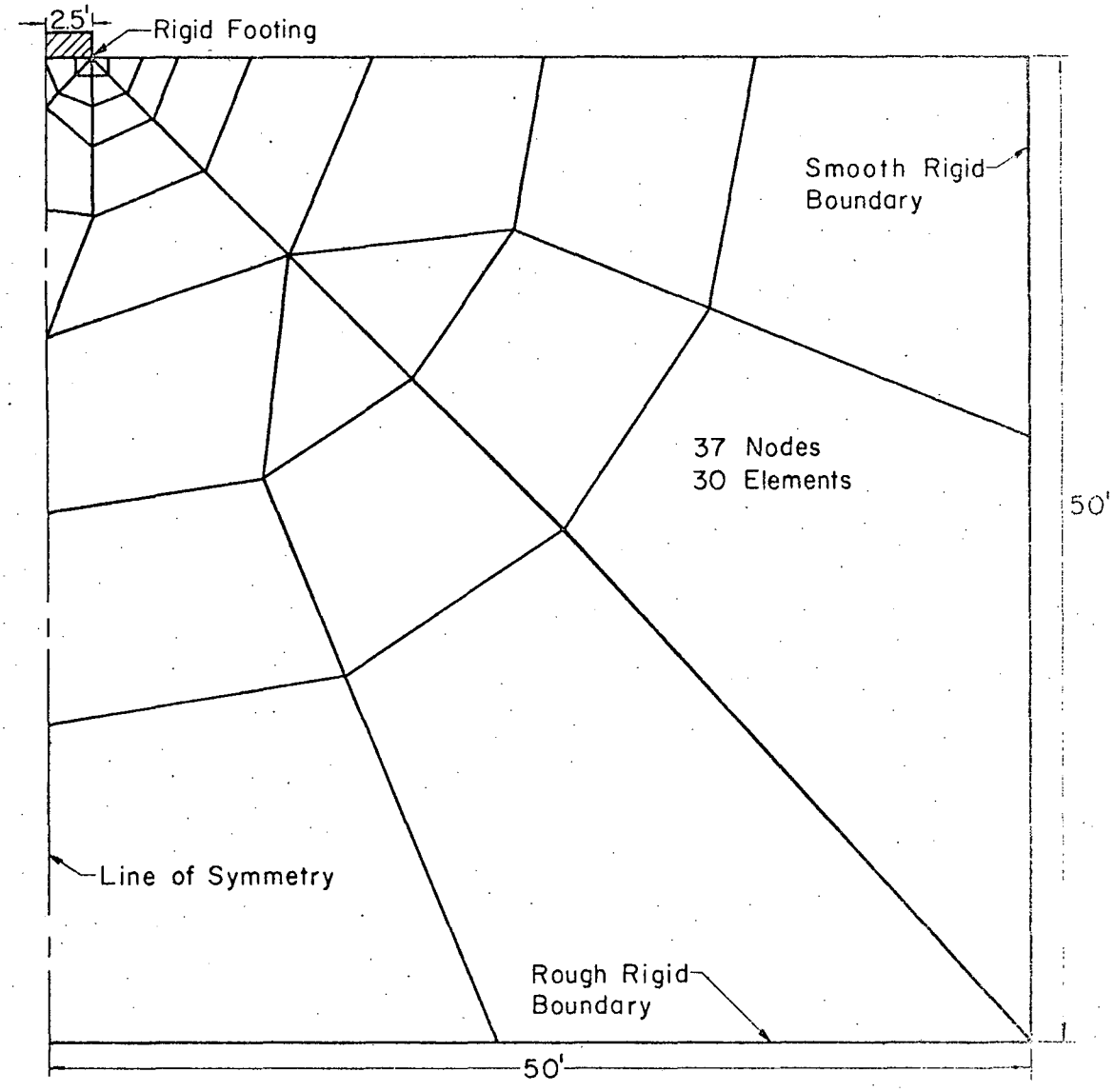

Fig. 27 Finite Element Mesh 1

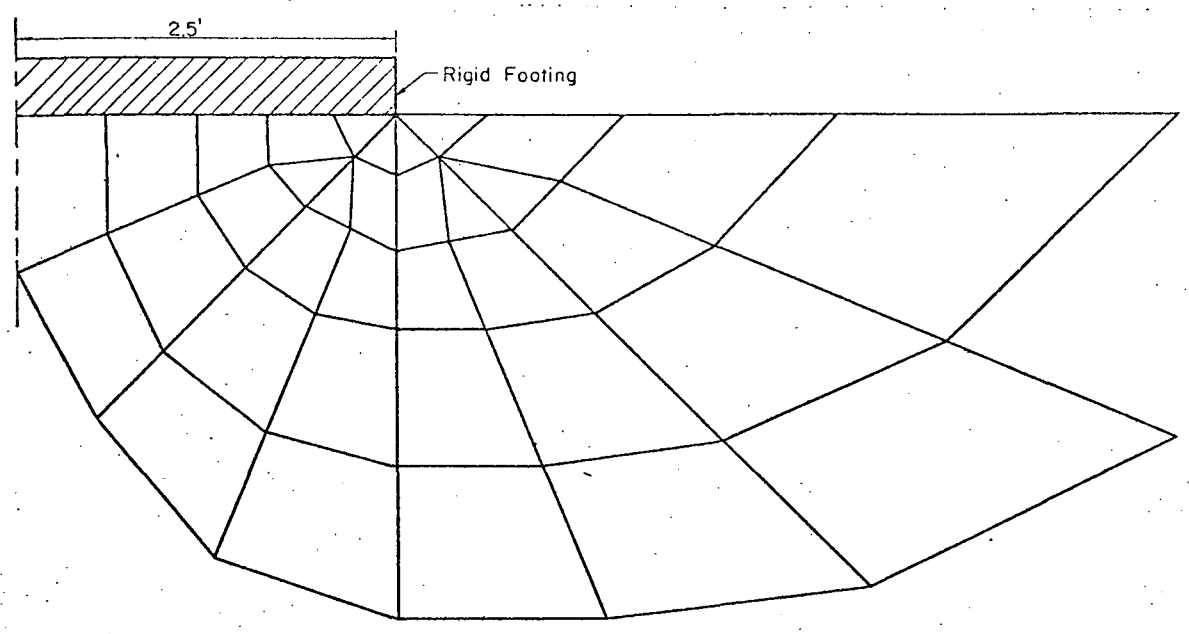

a) Mesh Detail Near Footing

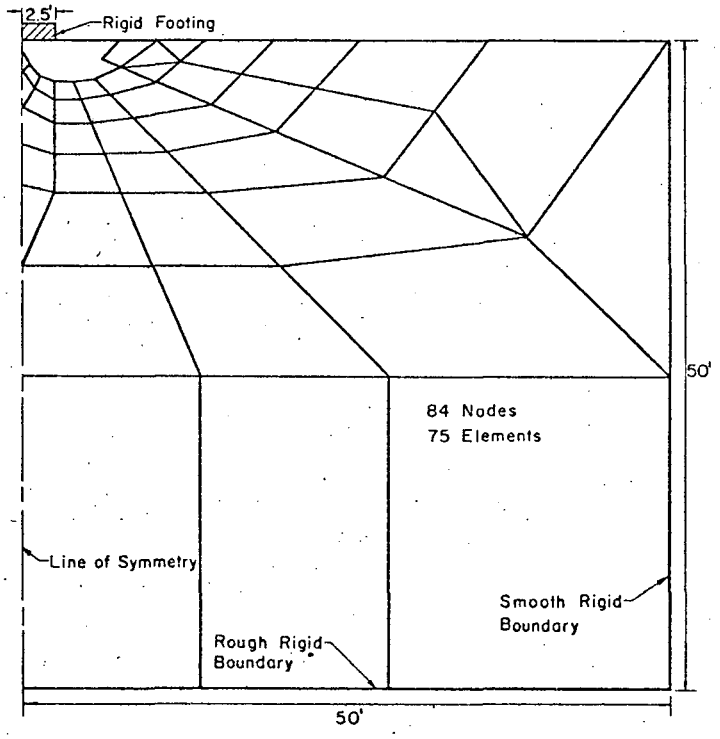

b) Mesh 2 Without Details Near Footing

Fig. 28 Finite Element Mesh 2

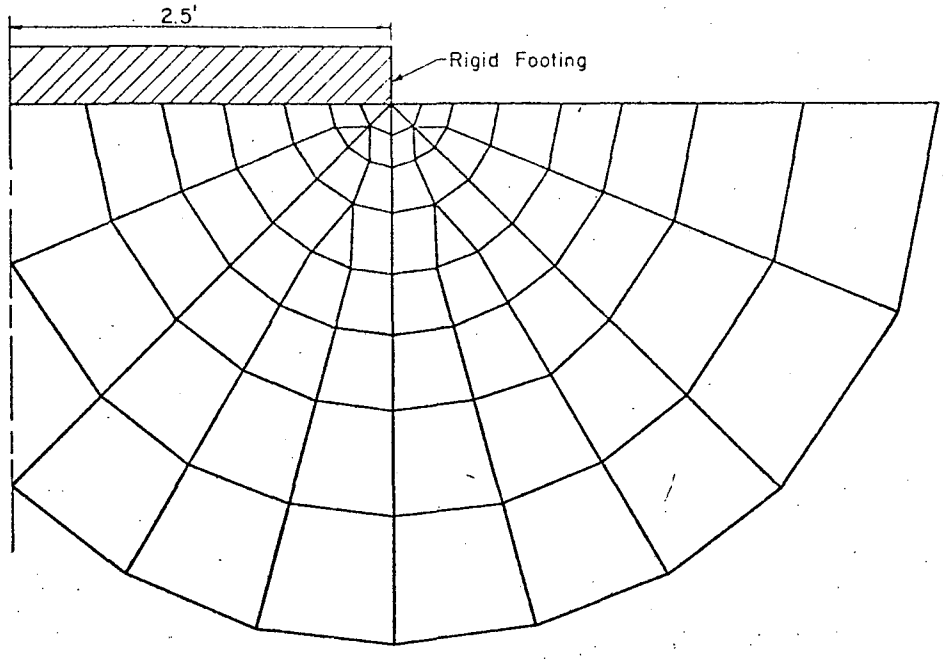

a) Mesh Detail Near Footing

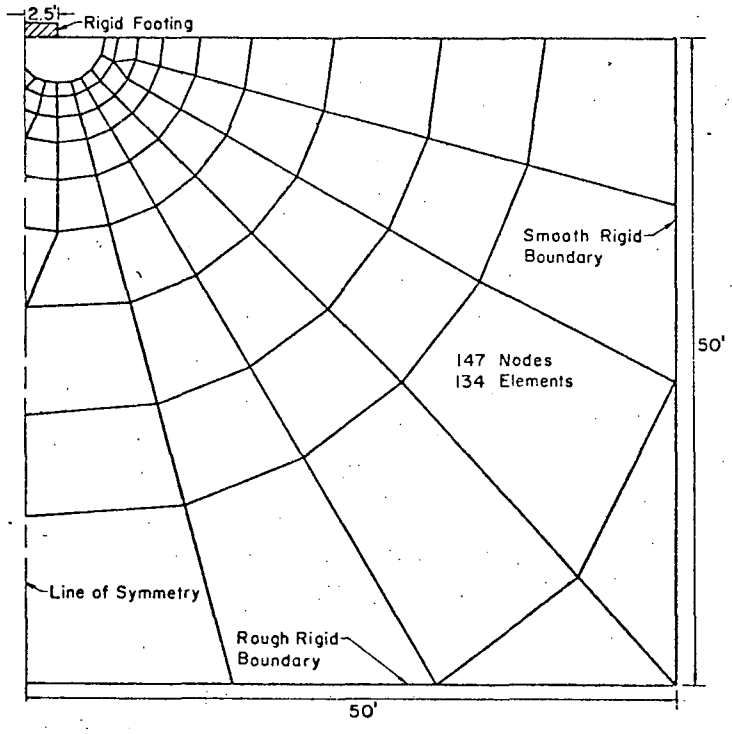

b) Mesh 3 Without Details Near Footing

Fig. 29 Finite Element Mesh 3

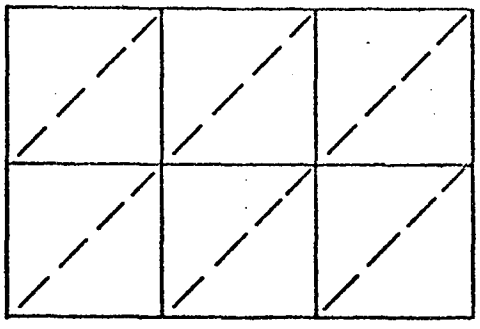

(a) Element Arrangement 1

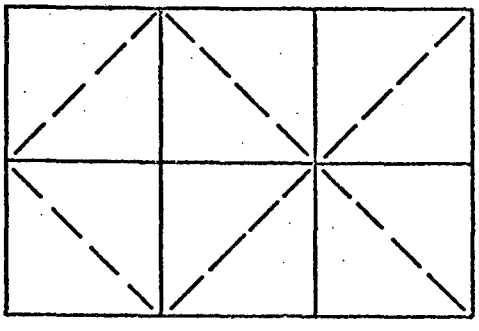

(b) Element Arrangement 2

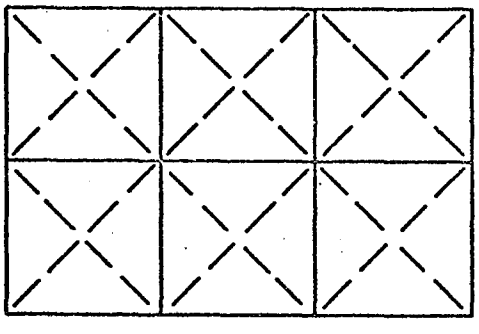

(c) Element Arrangement 3

Fig. 30 Three Element Arrangements

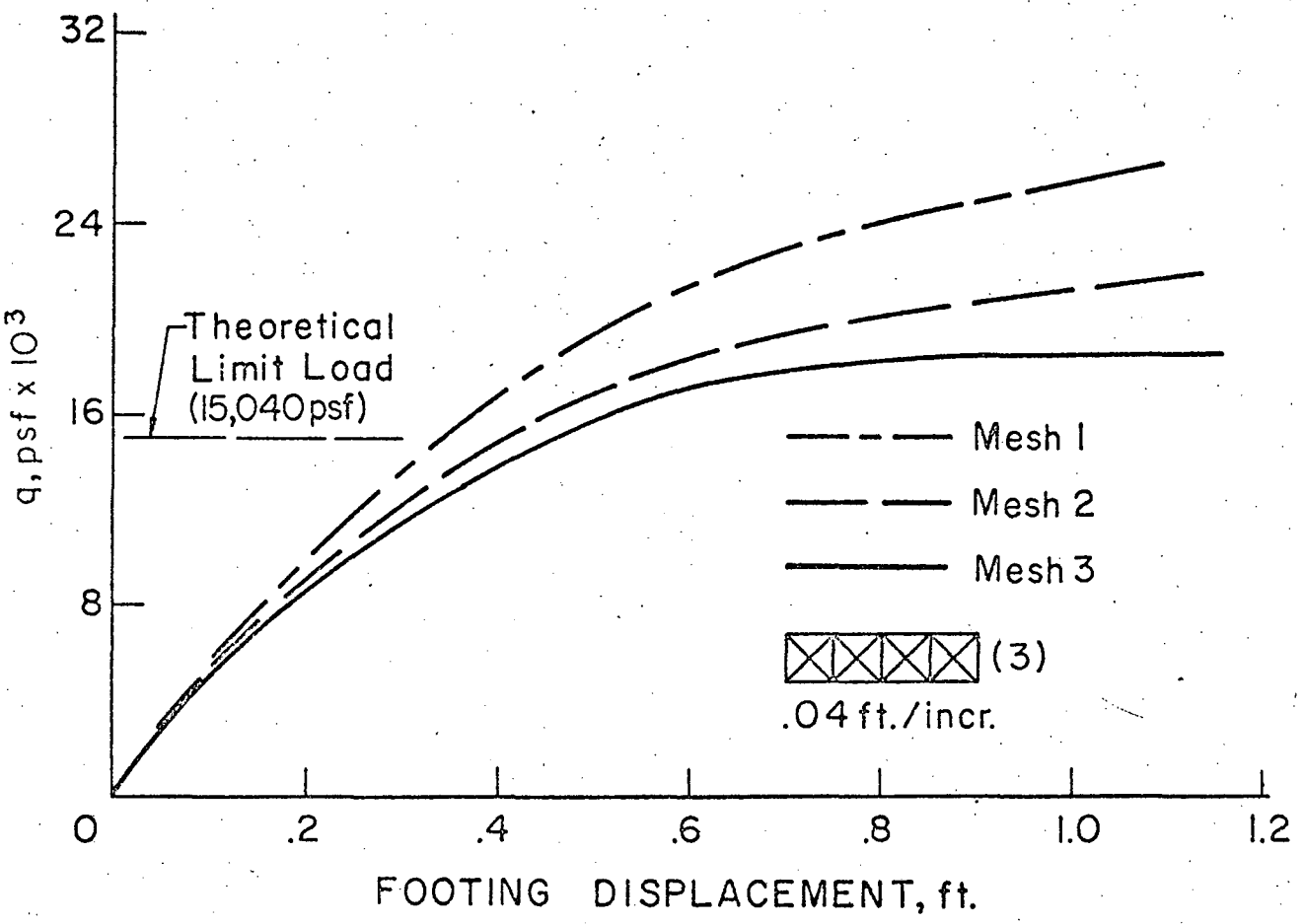

Fig. 31 Footing Load Displacement Curves - Effect of Mesh Size

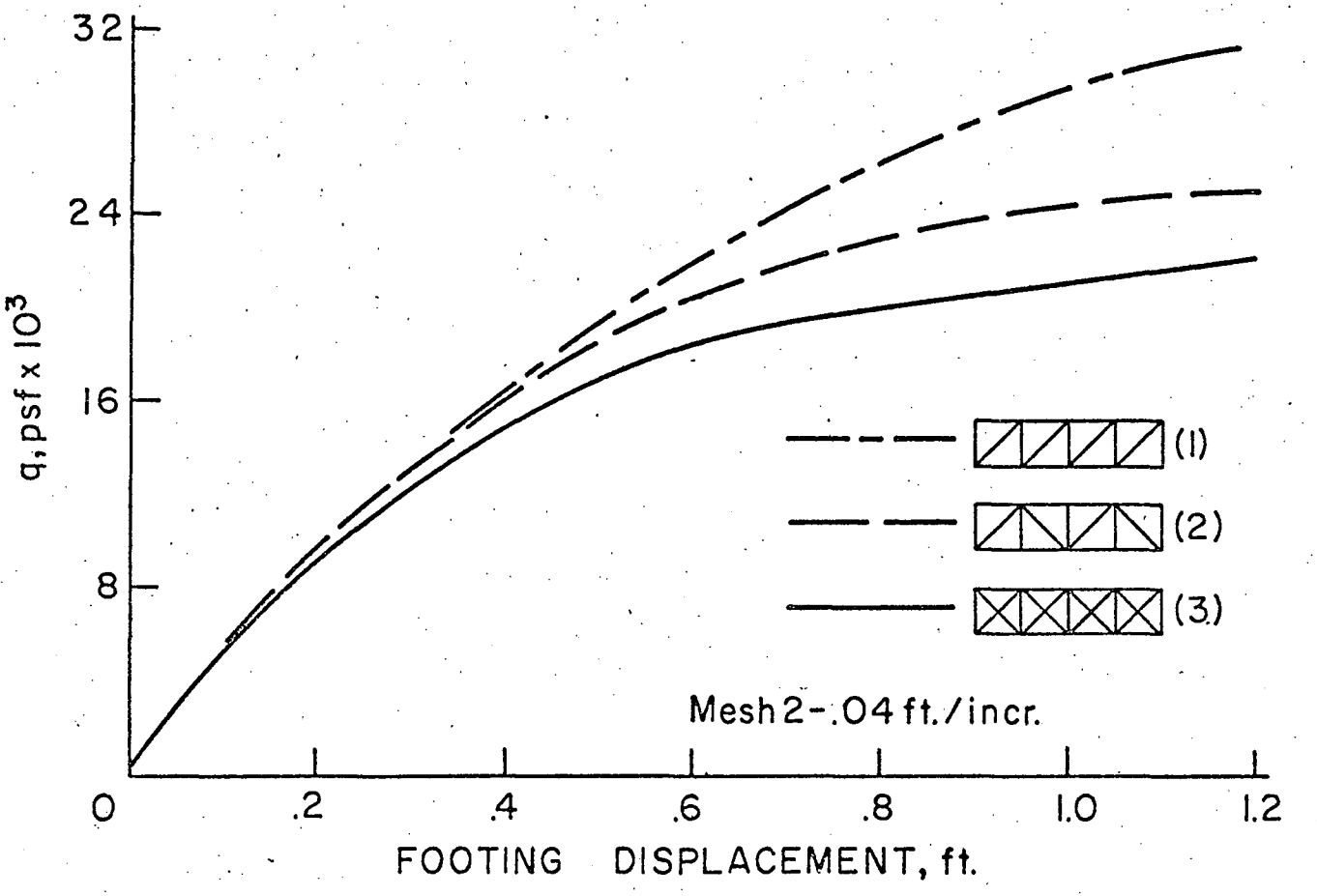

Fig. 32 Footing Load Displacement Curves - Effect of Element Arrangement

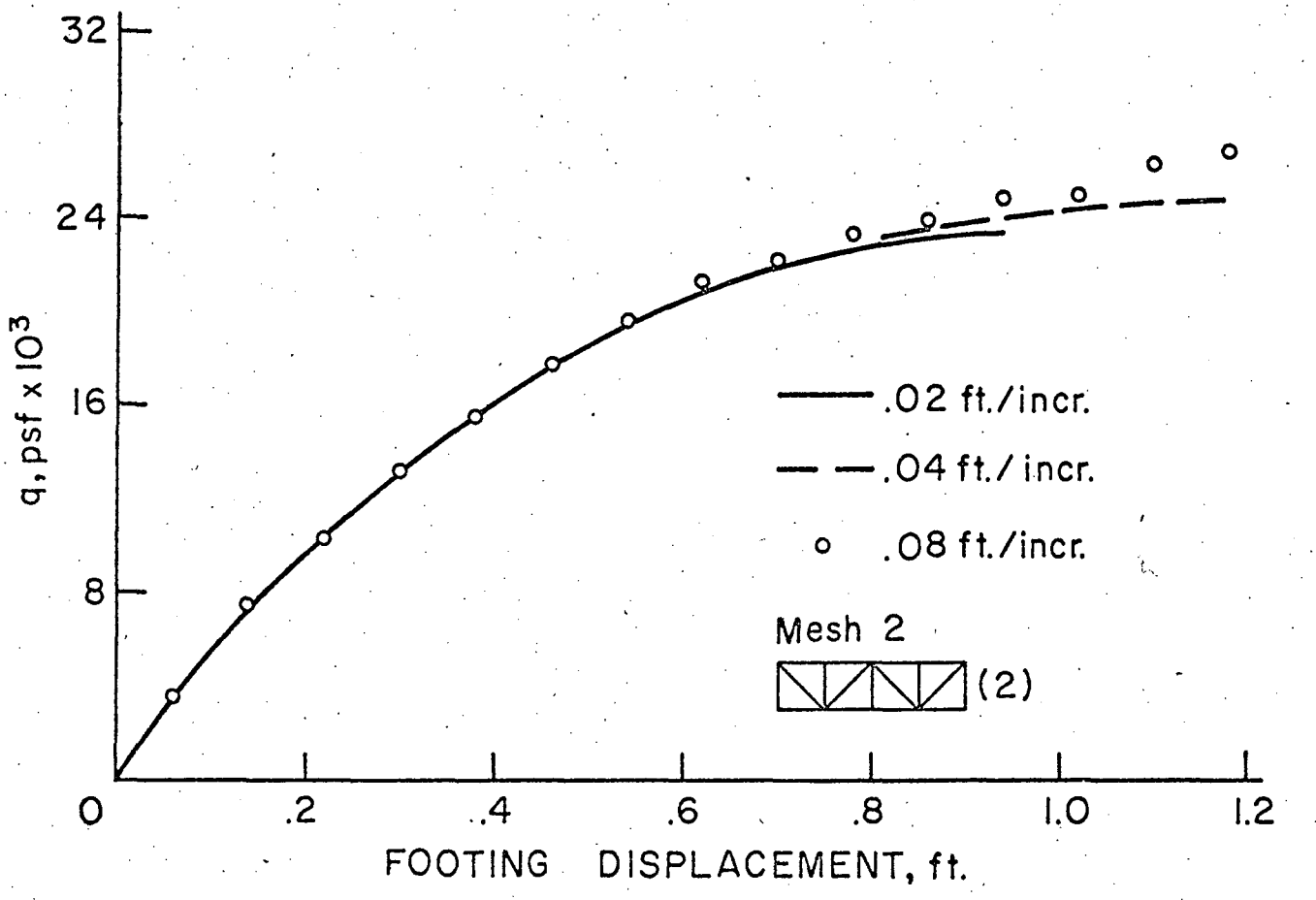

Fig. 33 Footing Load Displacement Curves - Effect of Increment Size

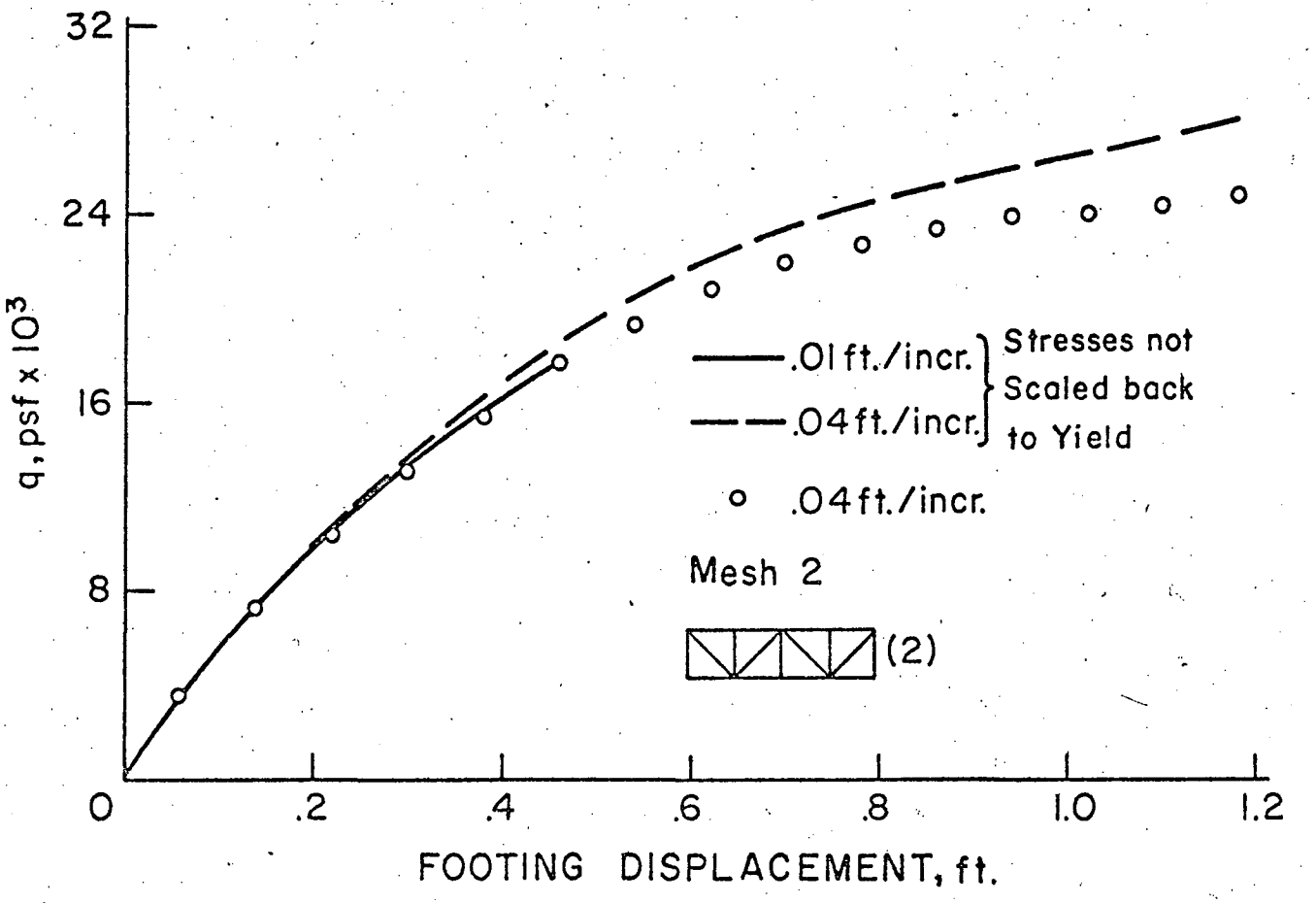

Fig. 34 Footing Load Displacement Curves - Effect of Stress Scaling

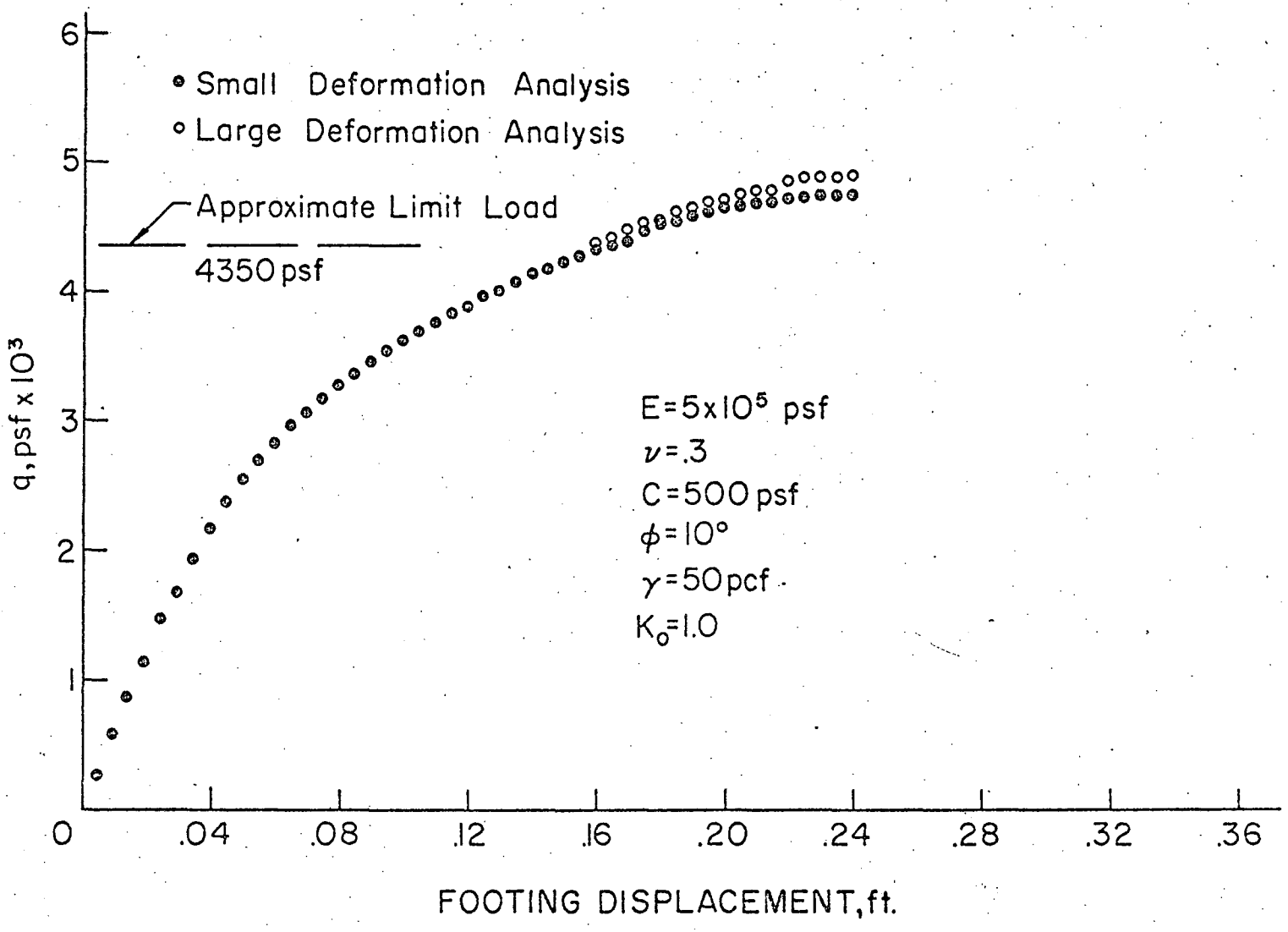

Fig. 35 Footing Load-Displacement Curves, $\varphi = 10^{\circ}$

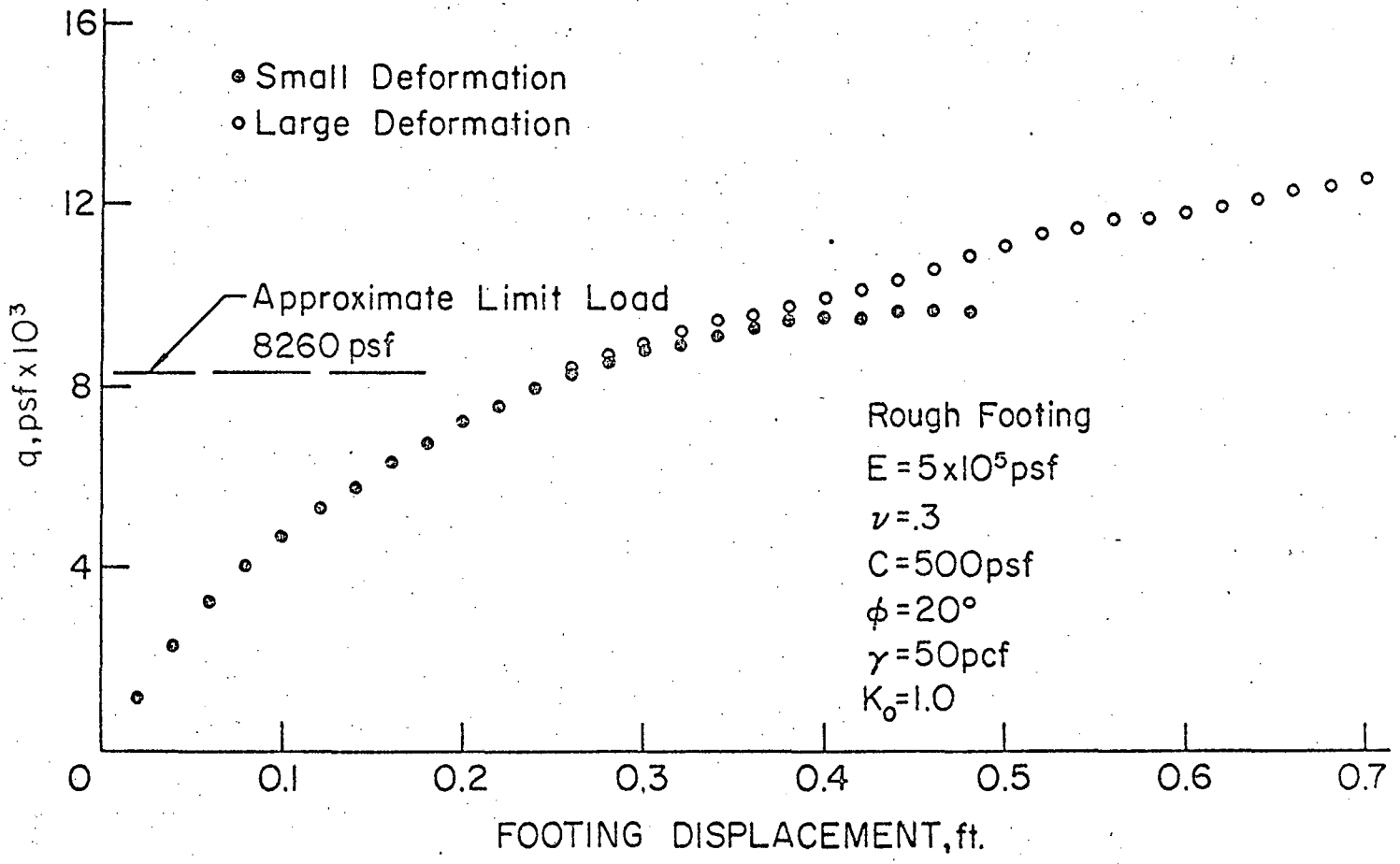

Fig. 36 Footing Load-Displacement Curves, $\varphi = 20^{\circ}$

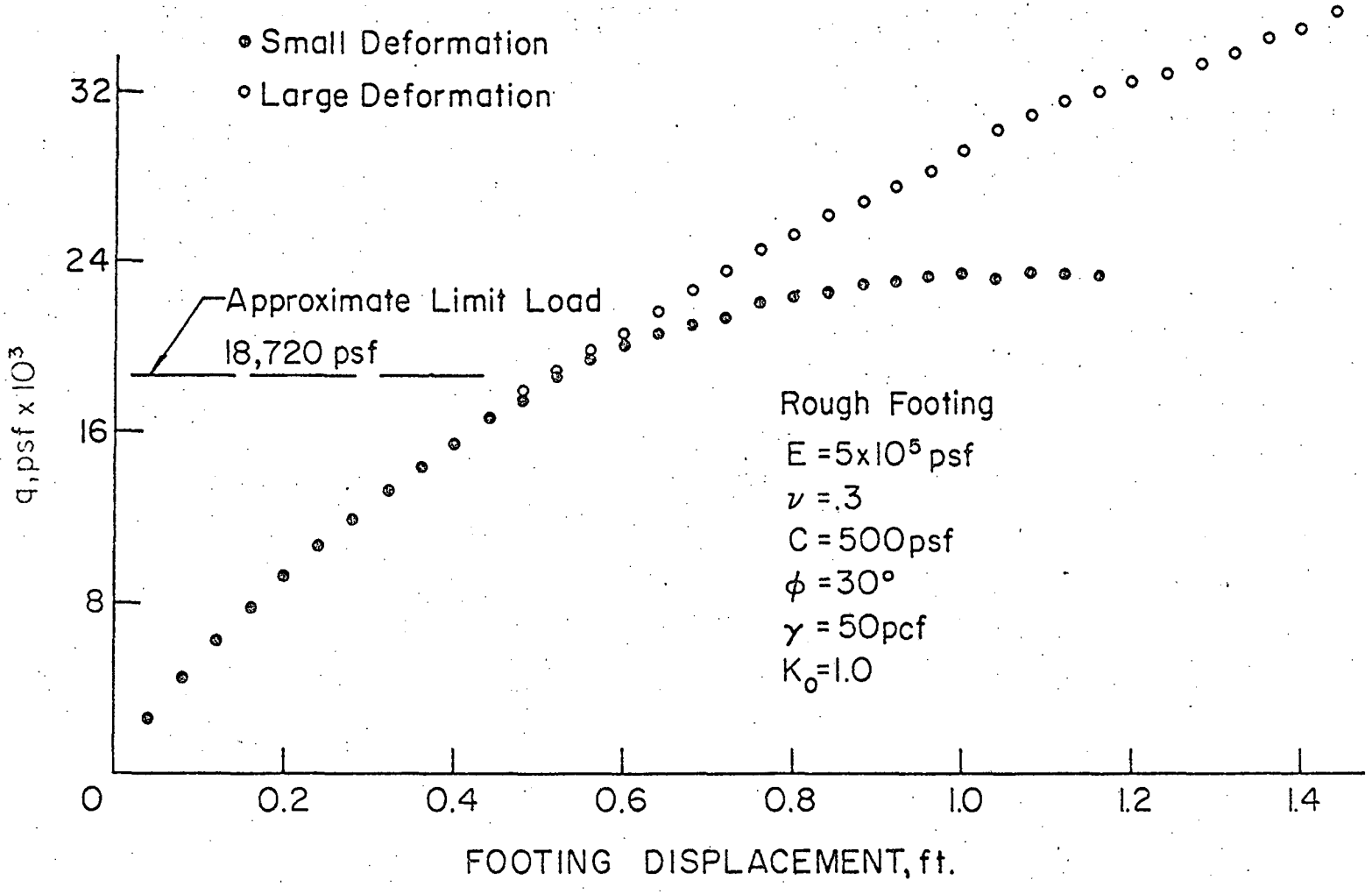

Fig. 37 Footing Load-Displacement Curves, $\varphi = 30^{\circ}$

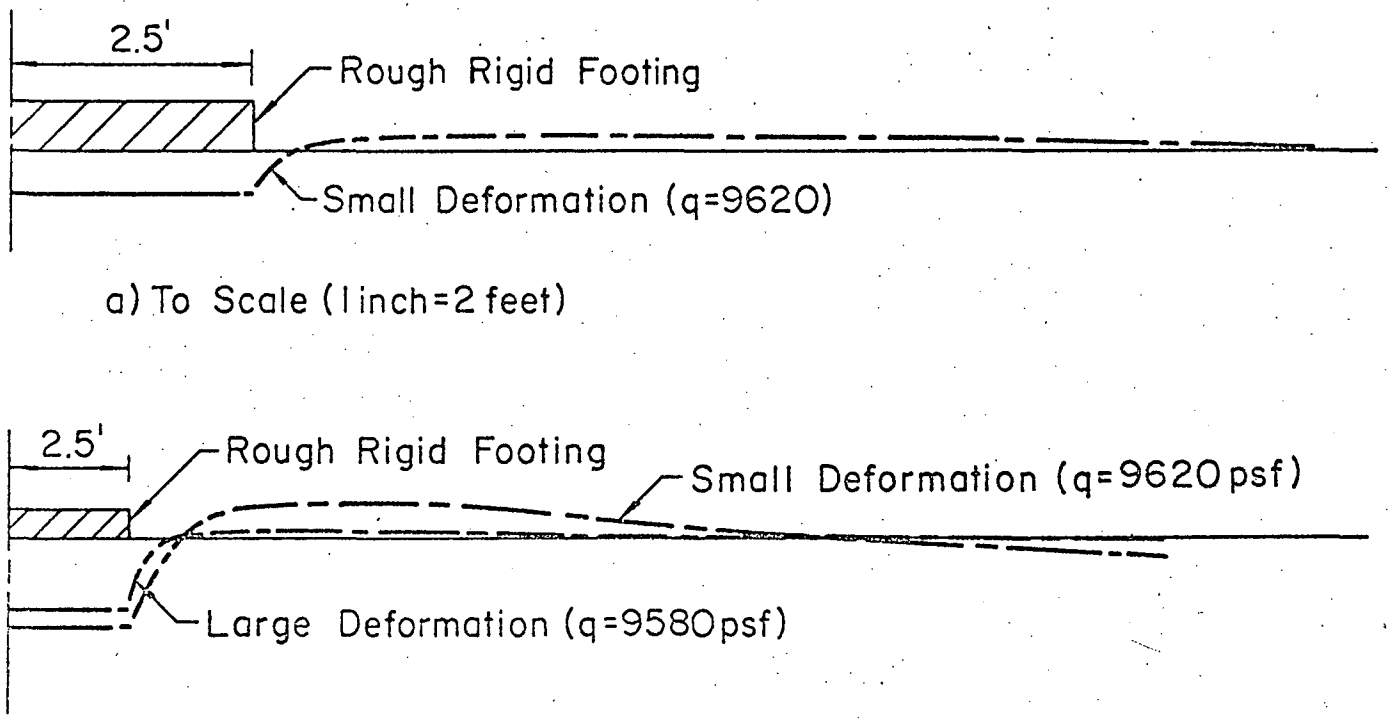

Fig. 38 Soil Surface Profile at the Numerical Limit Load ($\varphi = 20^{\circ}$, C = 500 psf)

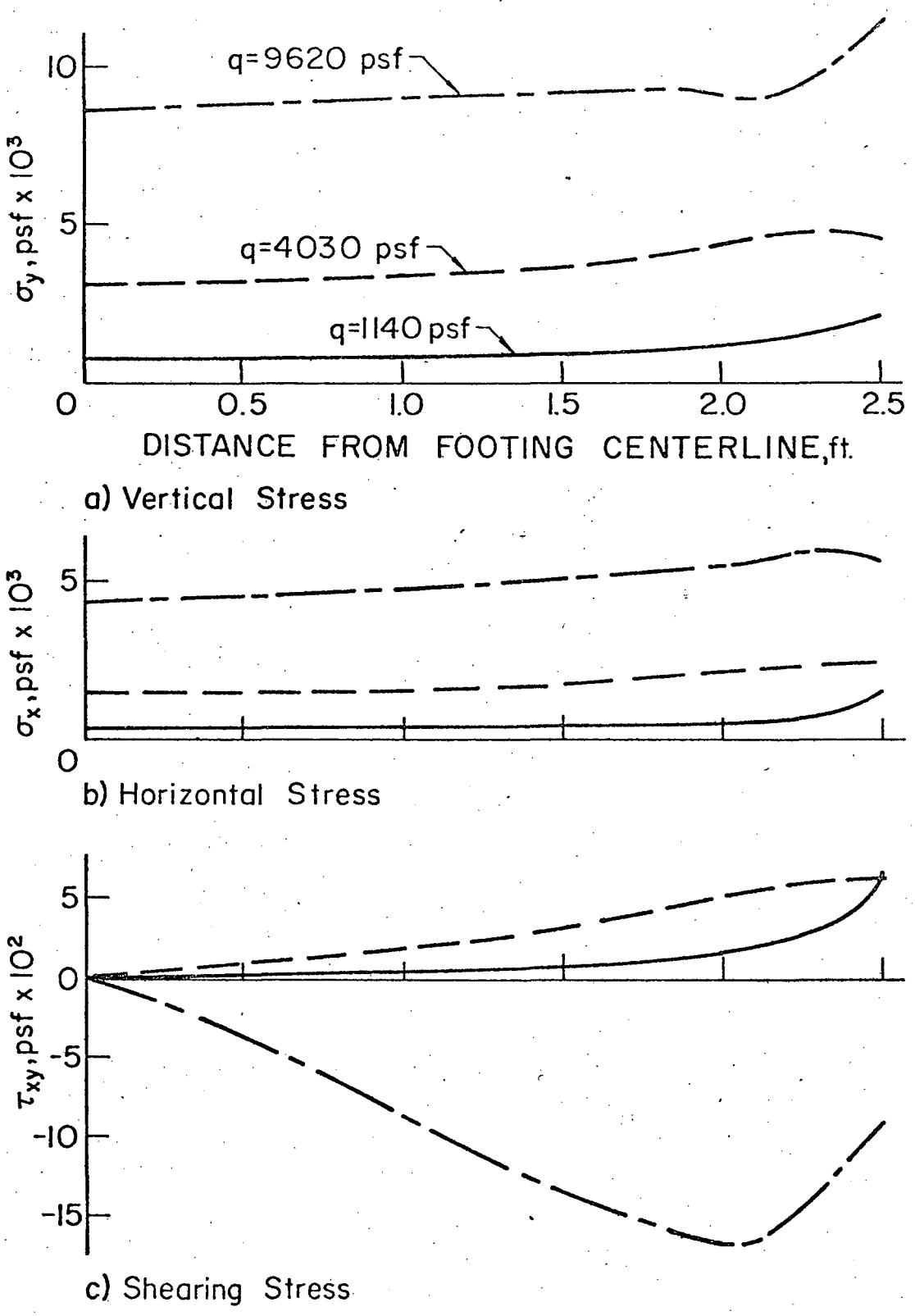

Fig. 39 Contact Stress Beneath Footing ($\varphi = 20^\circ$, C = 500 psf)

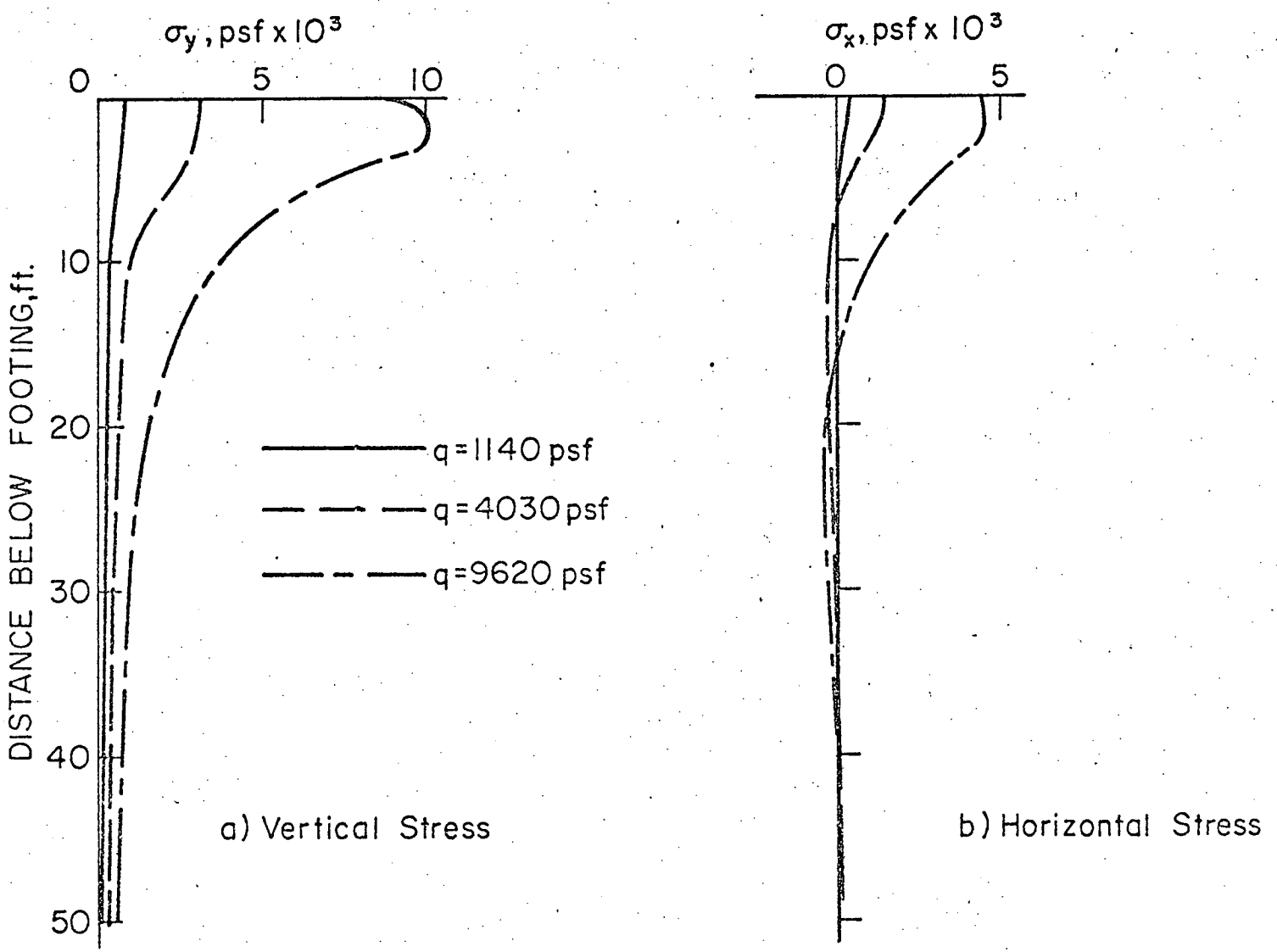

Fig. 40 Stress Distribution Below Footing Centerline (φ = 20°, C = 500 psf)

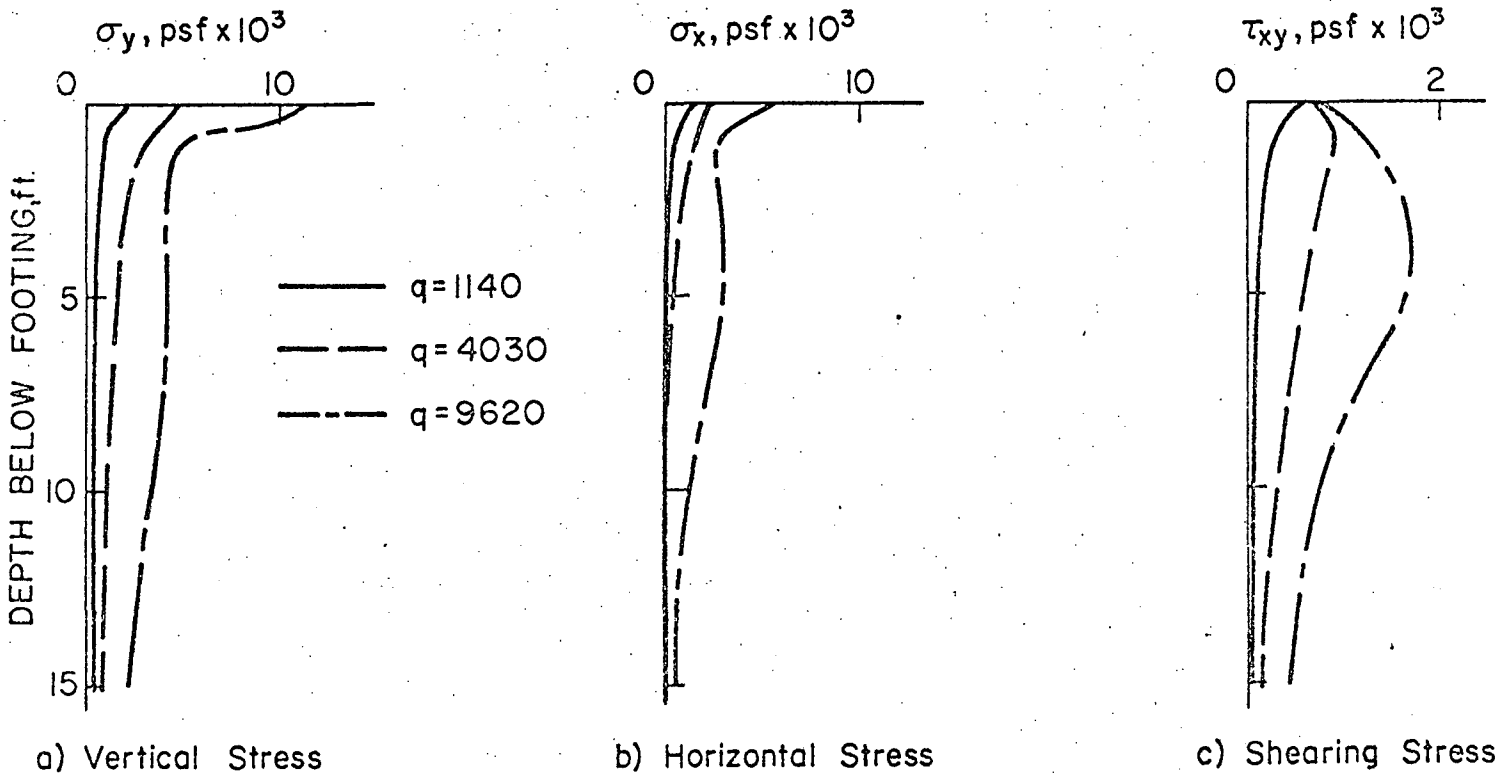

Fig. 41 Stress Distribution Below Footing Corner (φ = 20°, C = 500 psf)

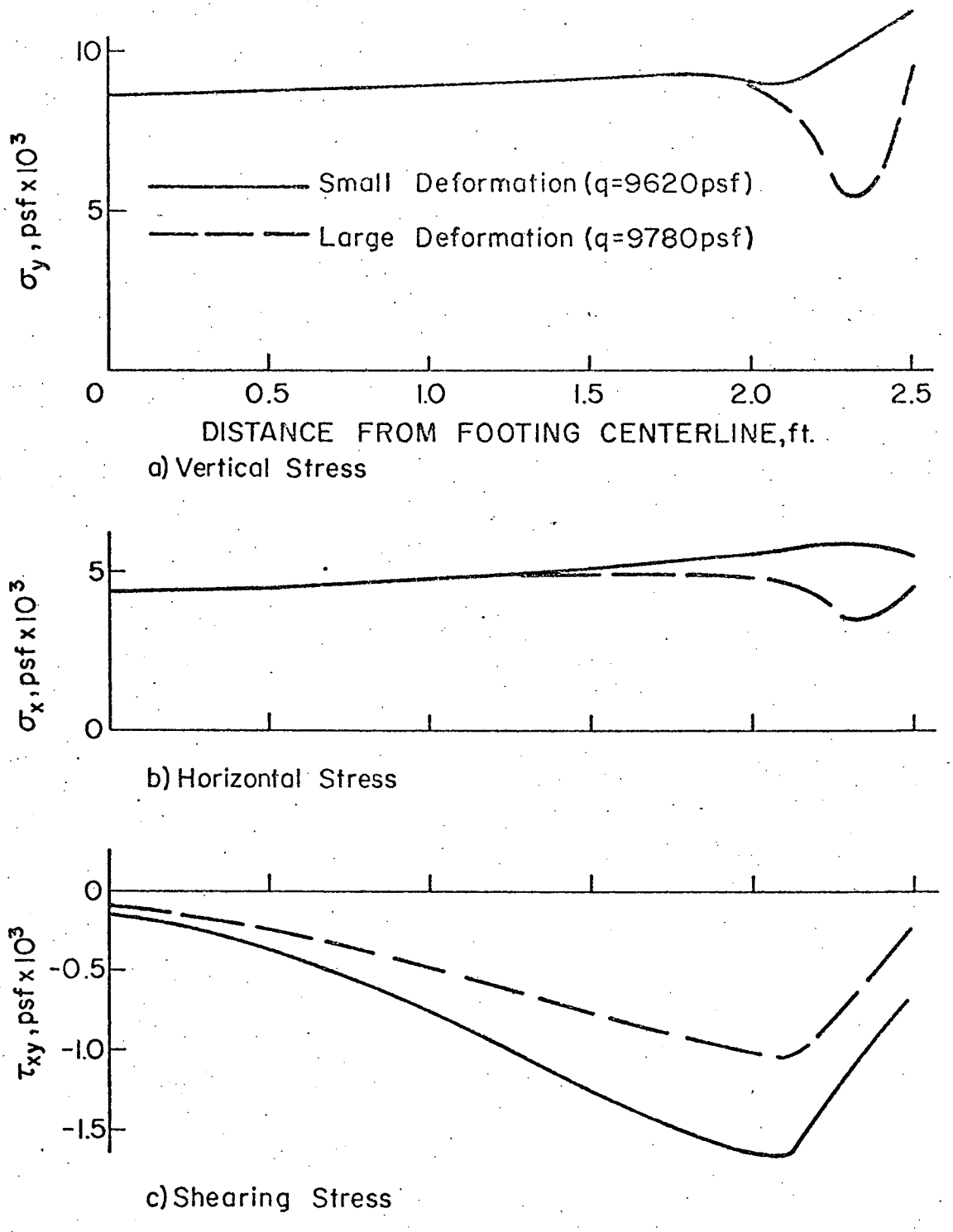

Fig. 42 Contact Stresses Beneath Footing at Limit Load - Small and Large Deformation ($\varphi = 20^\circ$, C = 500 psf)

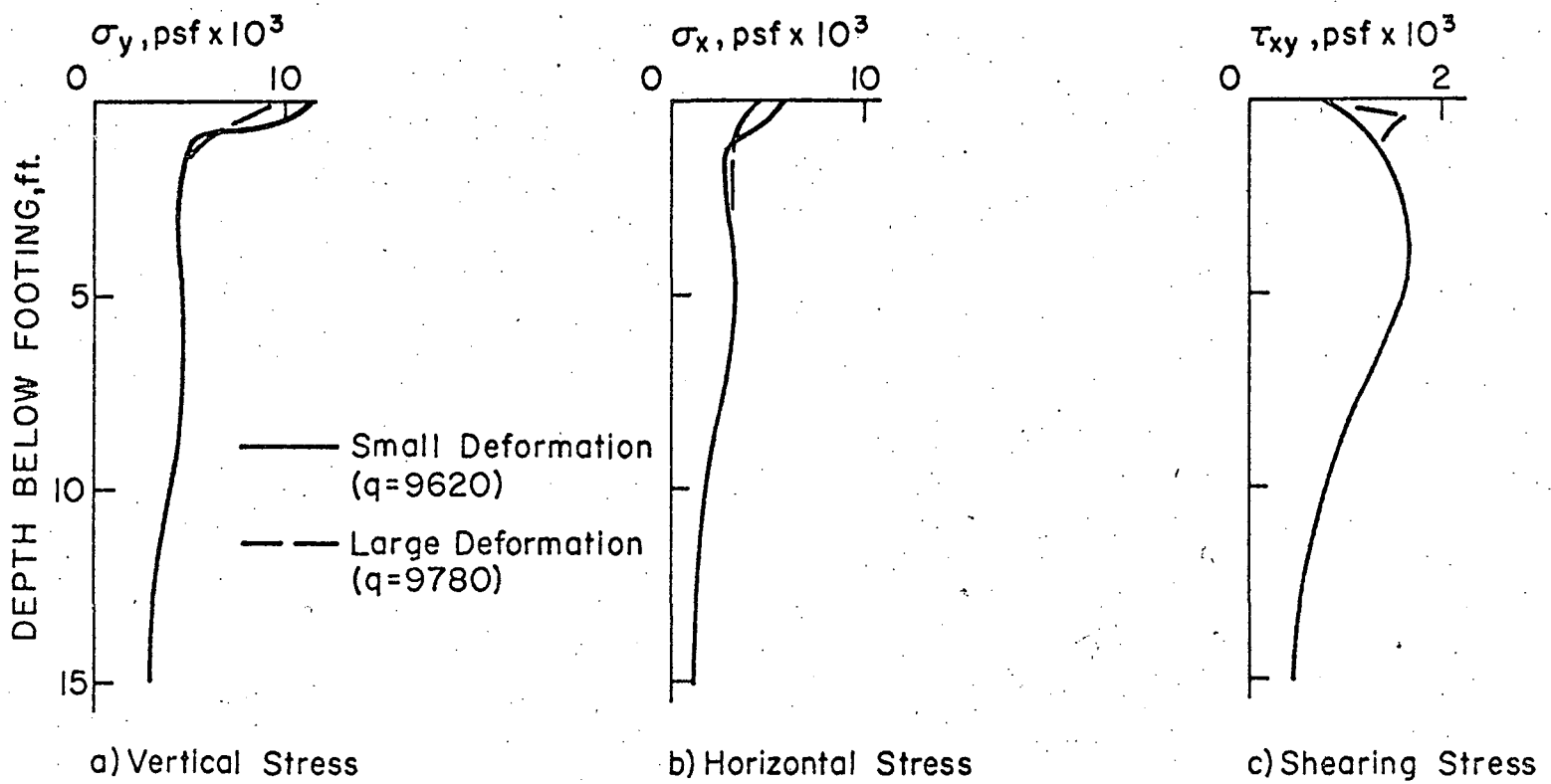

Fig. 43 Stress Distribution Below Footing Corner at Limit Load - Small and Large Deformation ($\varphi = 20^\circ$, C = 500 psf)

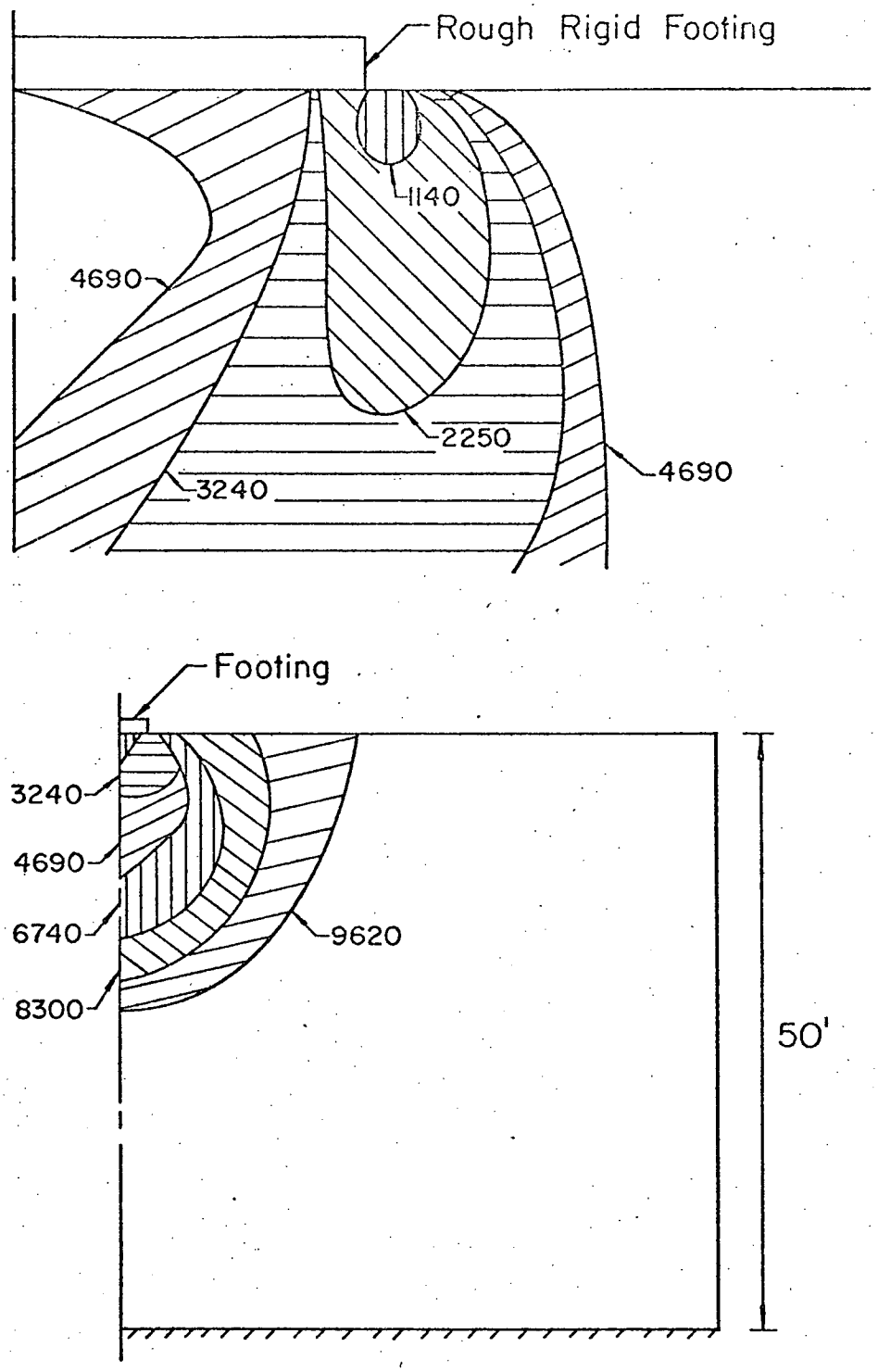

Fig. 44 Spread of Yield Zone ($\varphi = 20^{\circ}$, C = 500 psf)

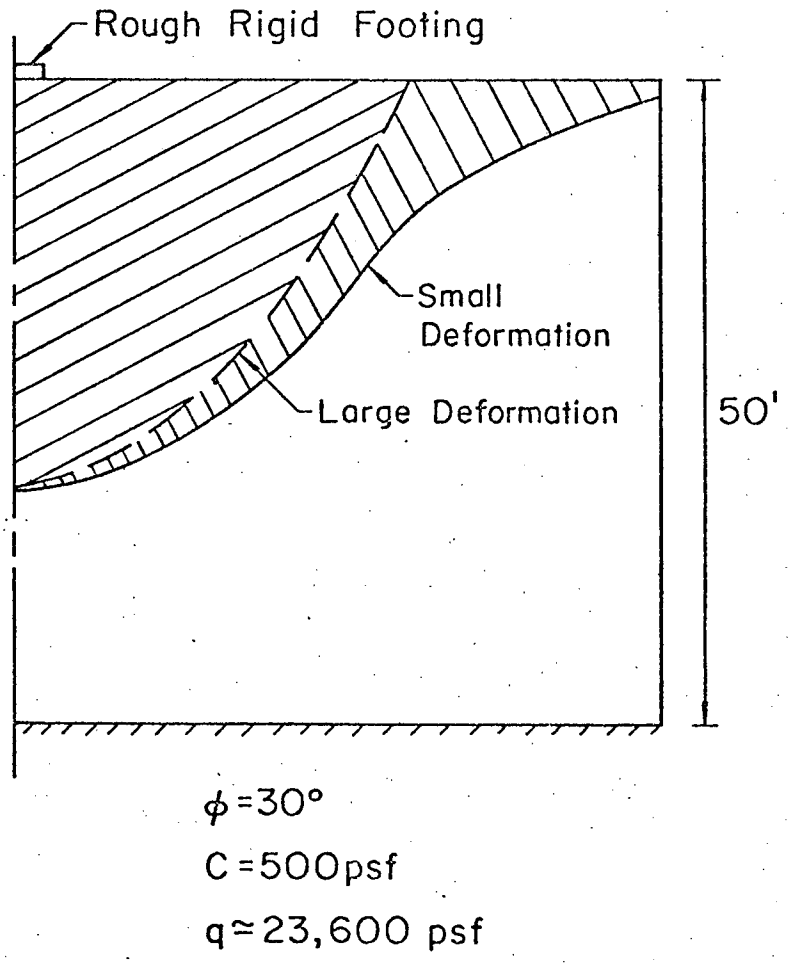

Fig. 45 Zones of Yielding at the Numerical Limit Load

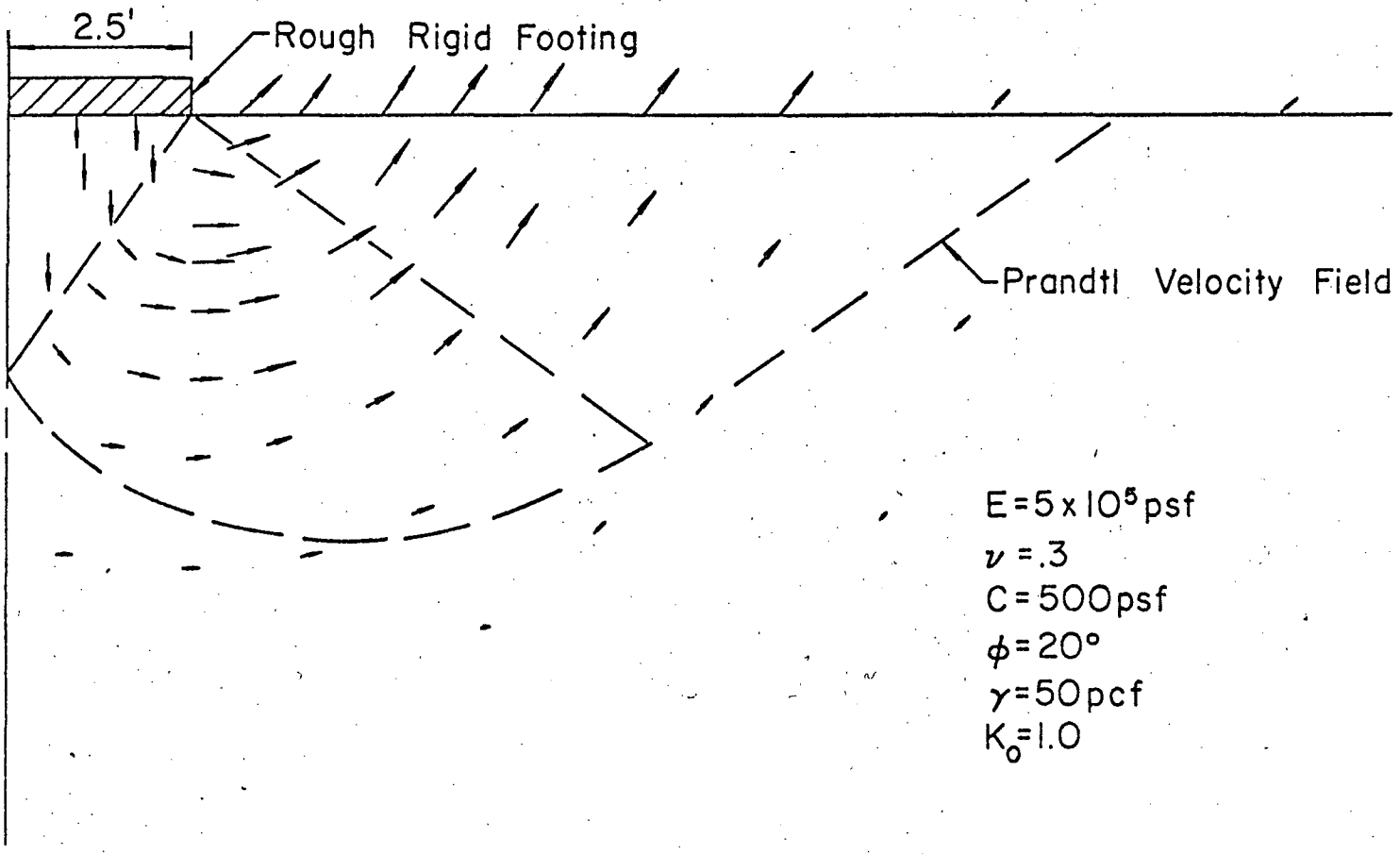

Fig. 46 Velocity Field at Numerical Limit Load (9620 psf) - Small Deformation

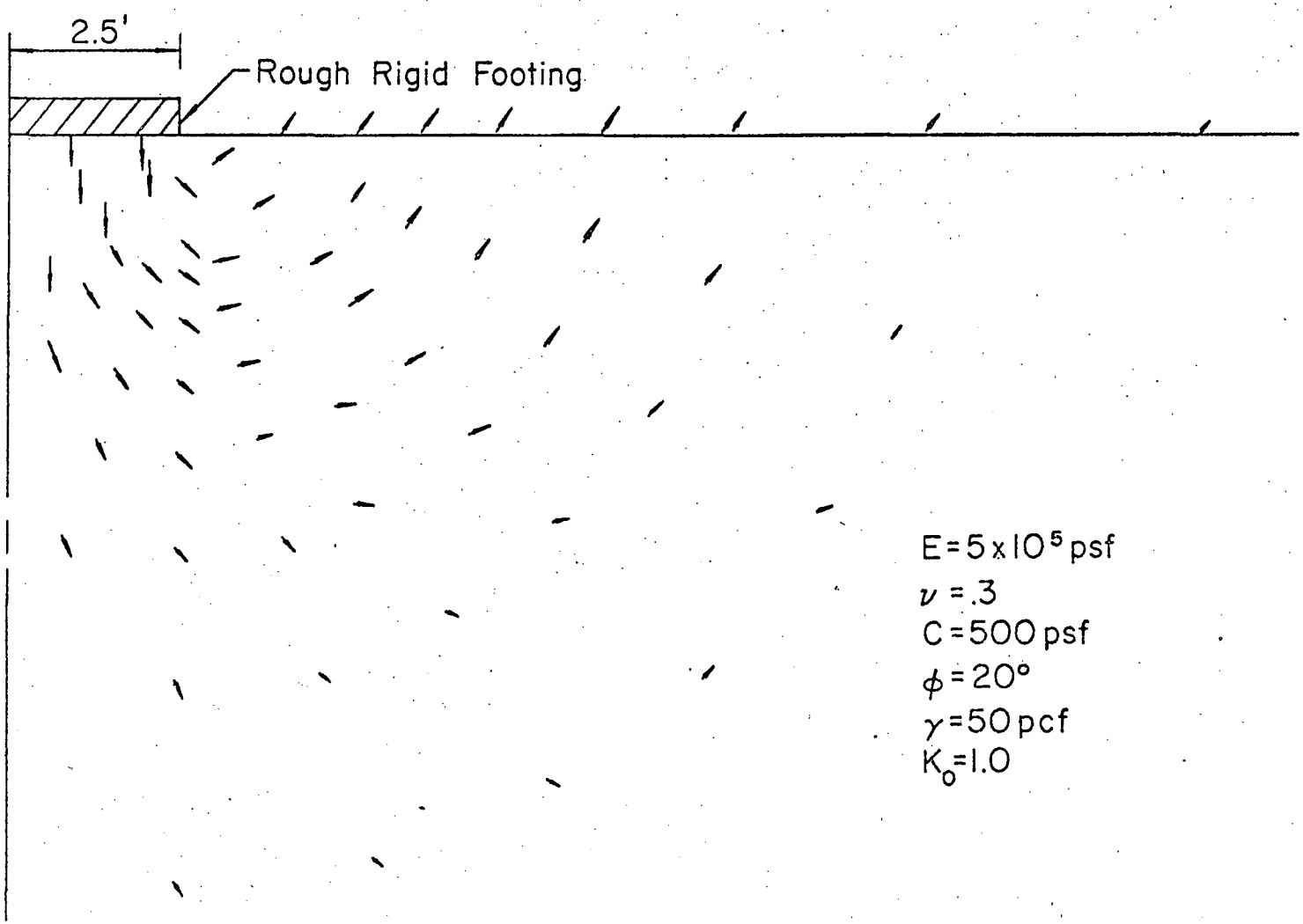

Fig. 47 Velocity Field at Numerical Limit Load (9620 psf) - Large Deformation

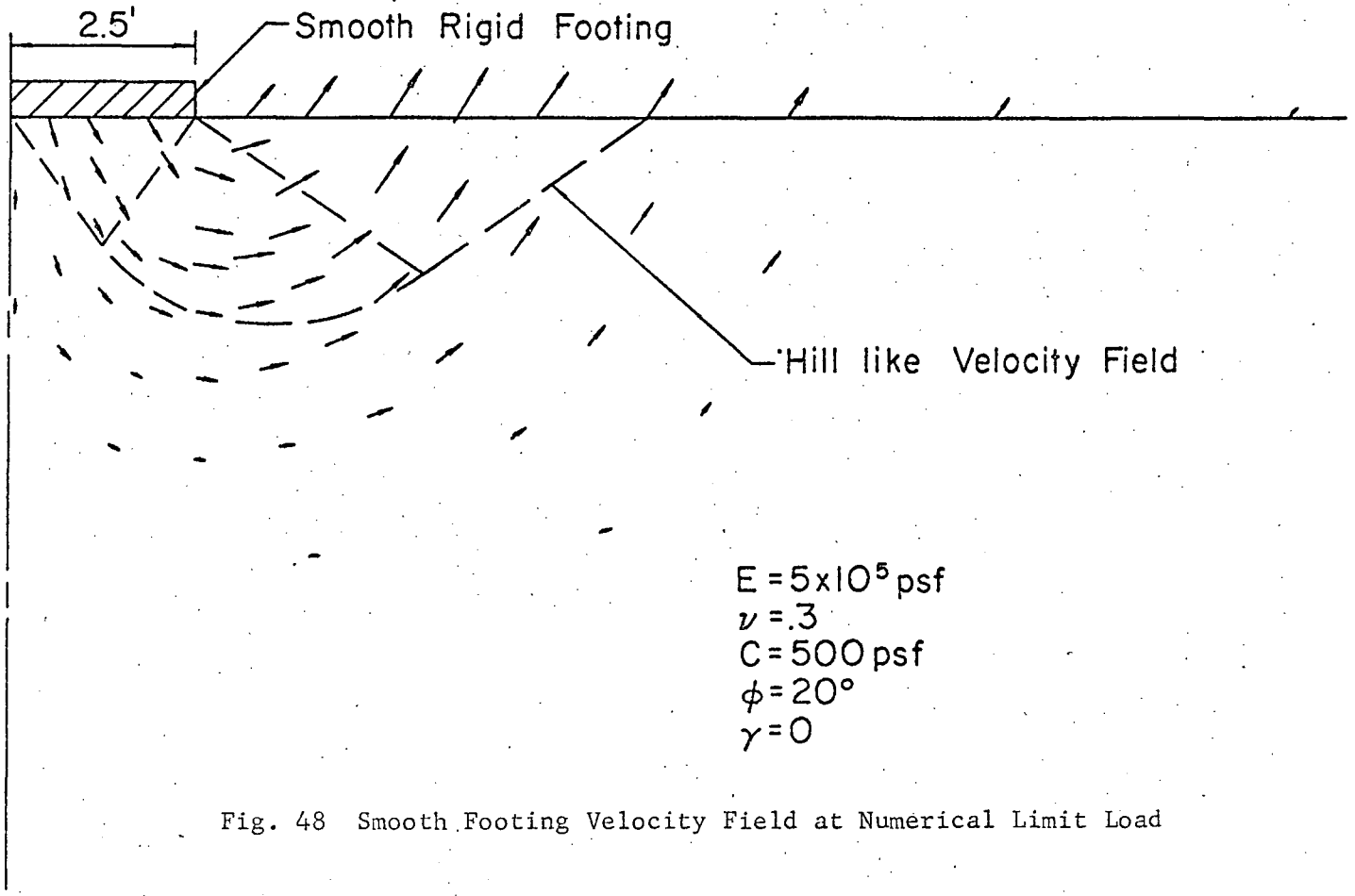

Fig. 48 Smooth Footing Velocity Field at Numerical Limit Load

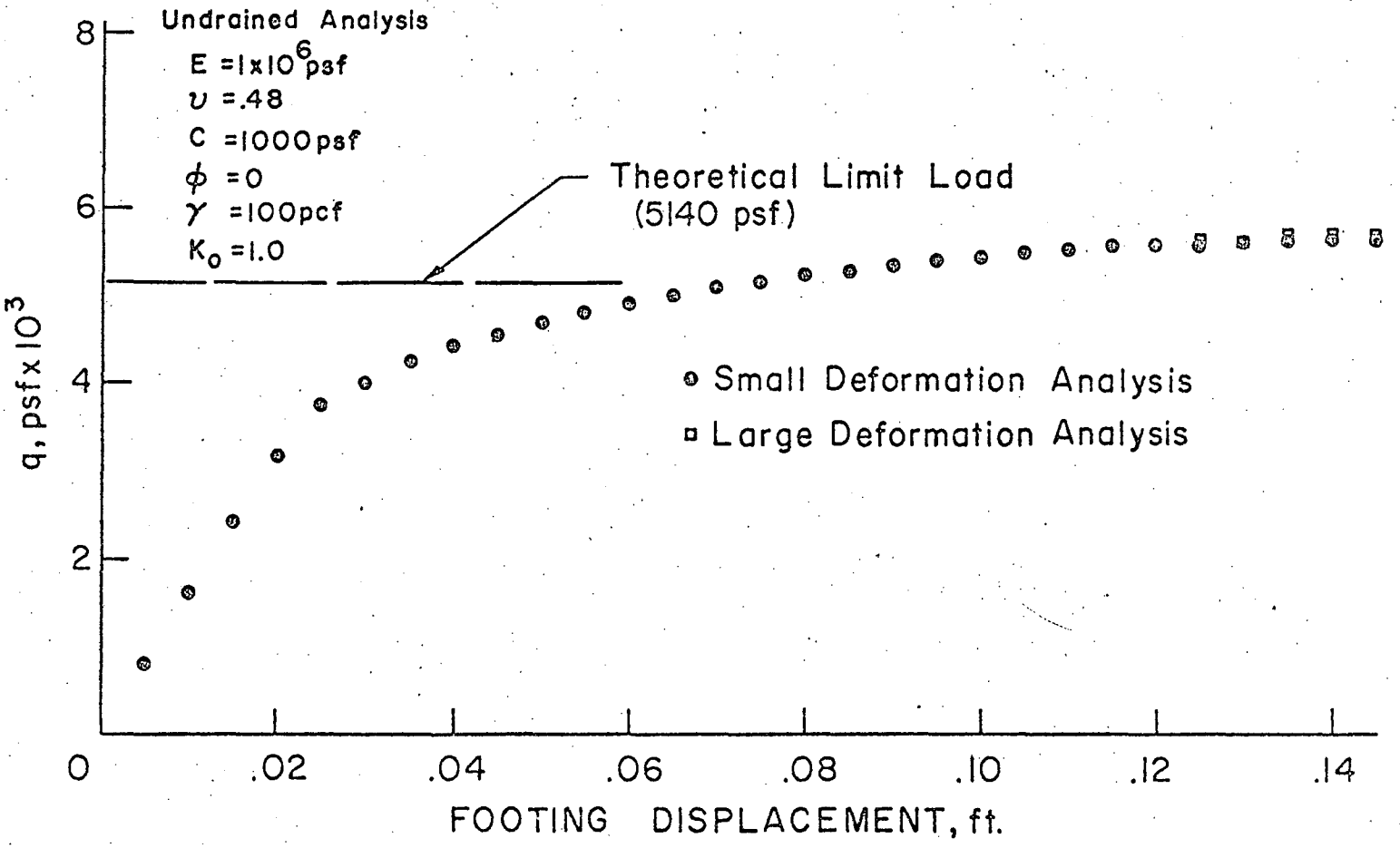

Fig. 49 Footing Load-Displacement Curves, E = $1x10^6$ psf

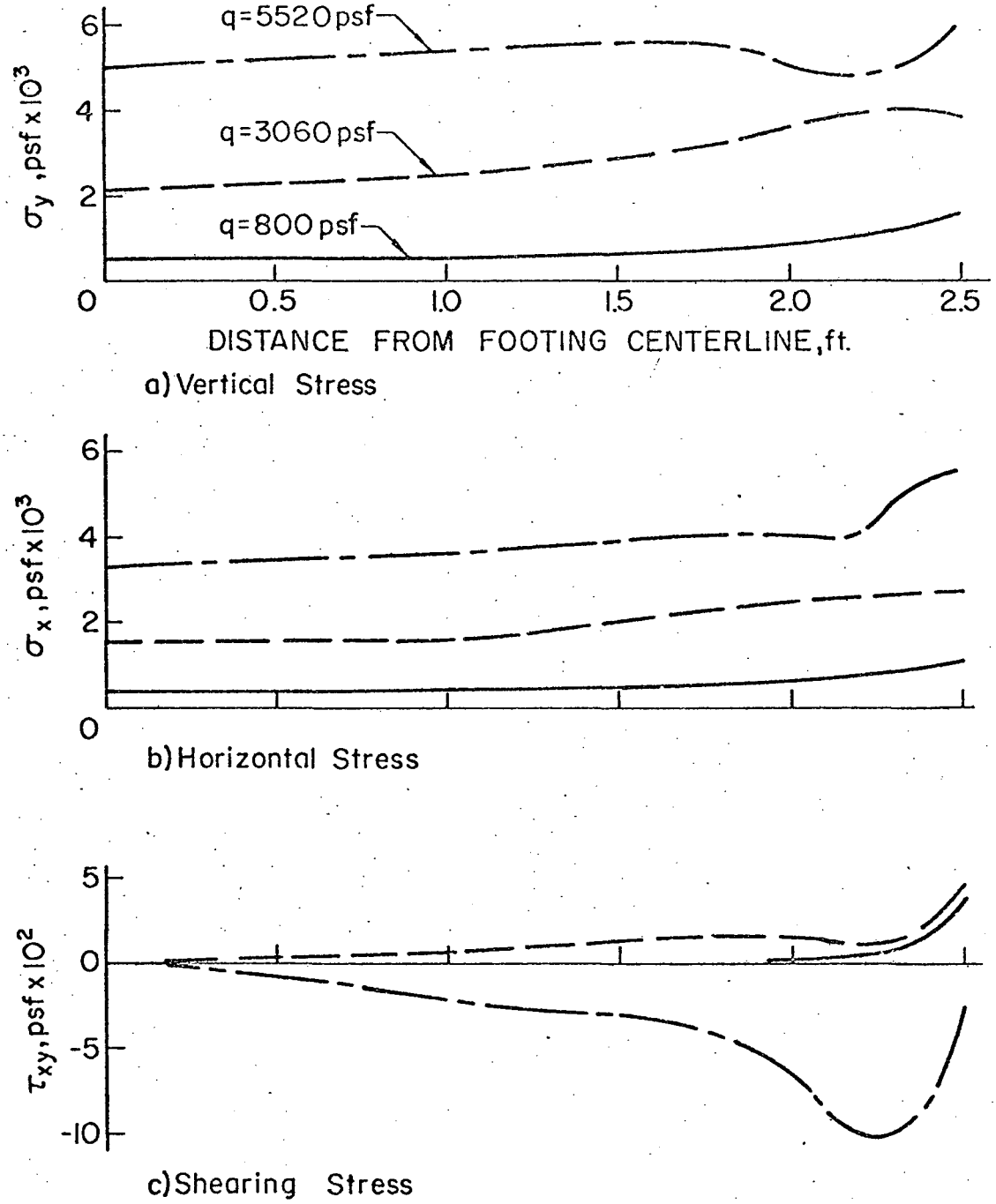

Fig. 50 Contact Stresses Beneath Footing (ω = 0, C = 1000 psf)

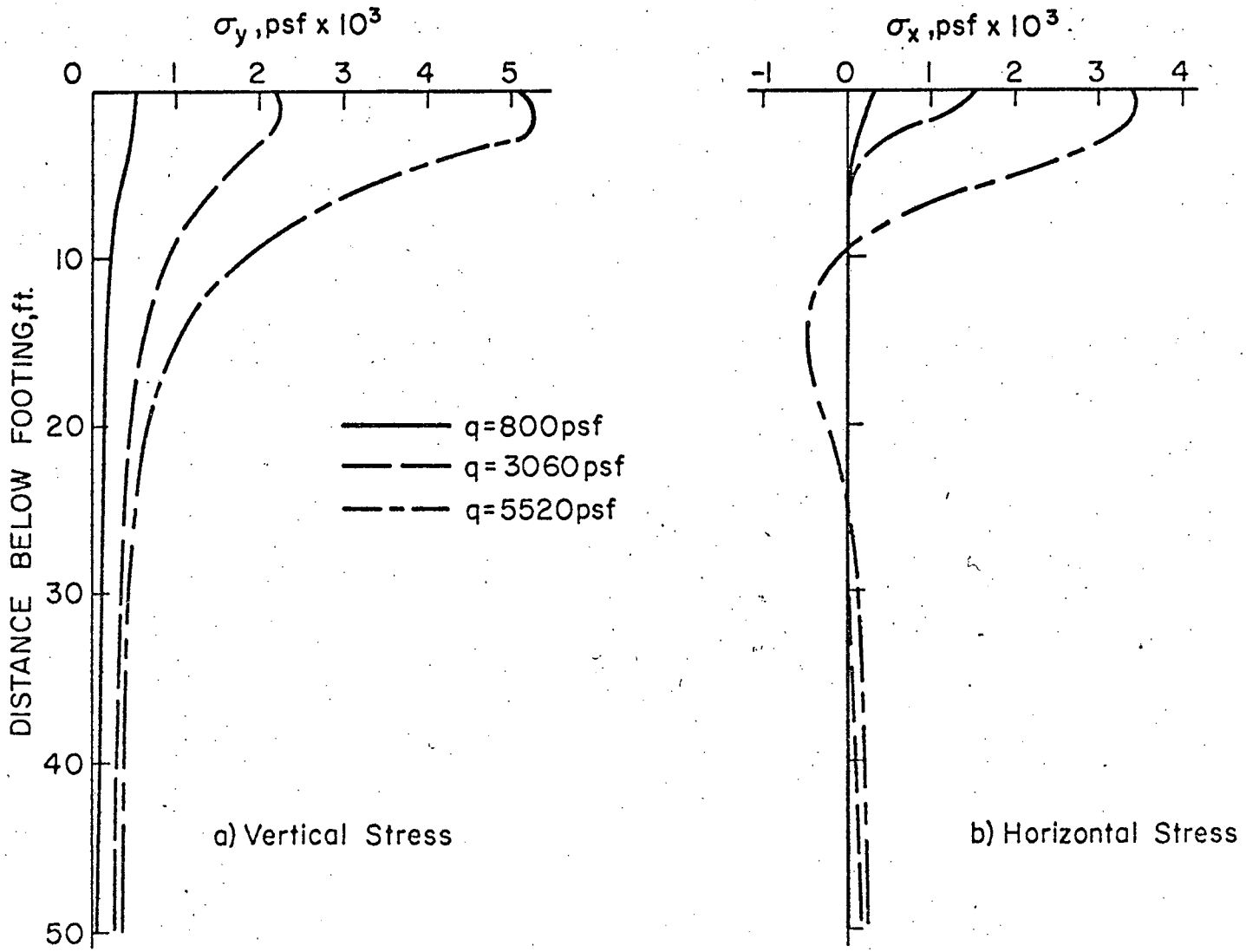

Fig. 51 Stress Distribution Below Footing Centerline (φ = 0, C = 1000 psf)

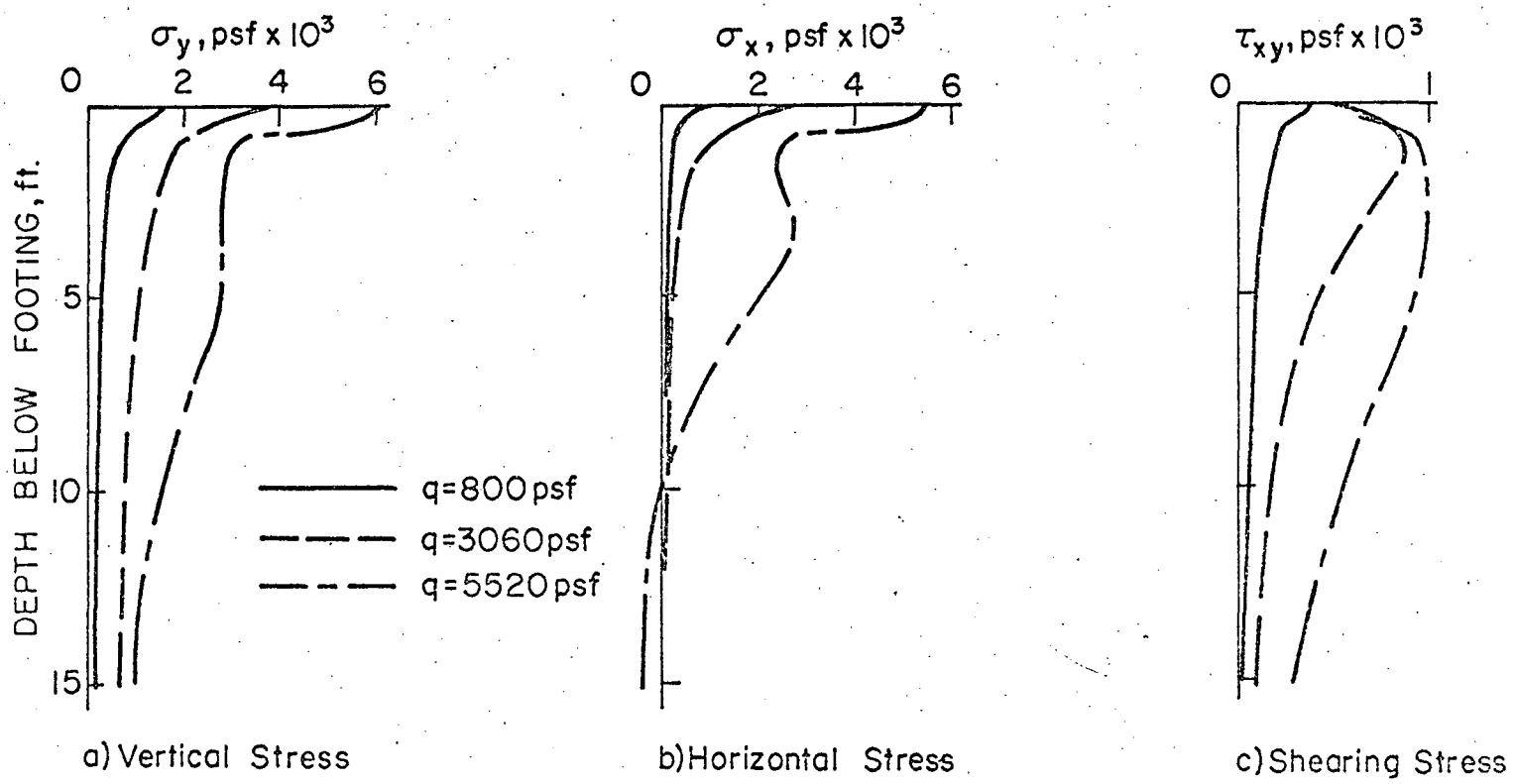

Fig. 52 Stress Distribution Below Footing Corner ($\varphi = 0$, C = 1000 psf)

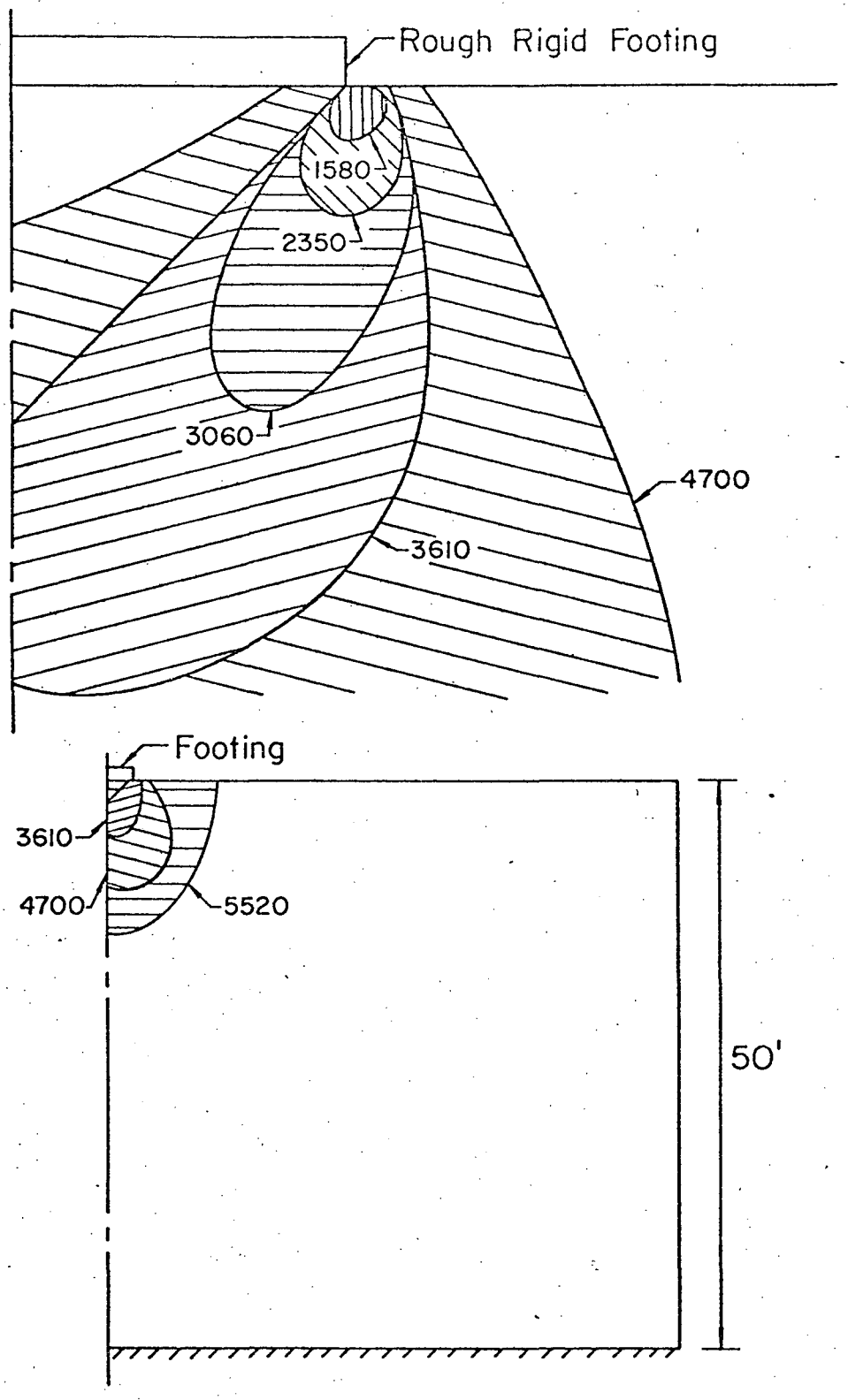

Fig. 53 Spread of Yield Zone (φ = 0, C = 1000 psf)

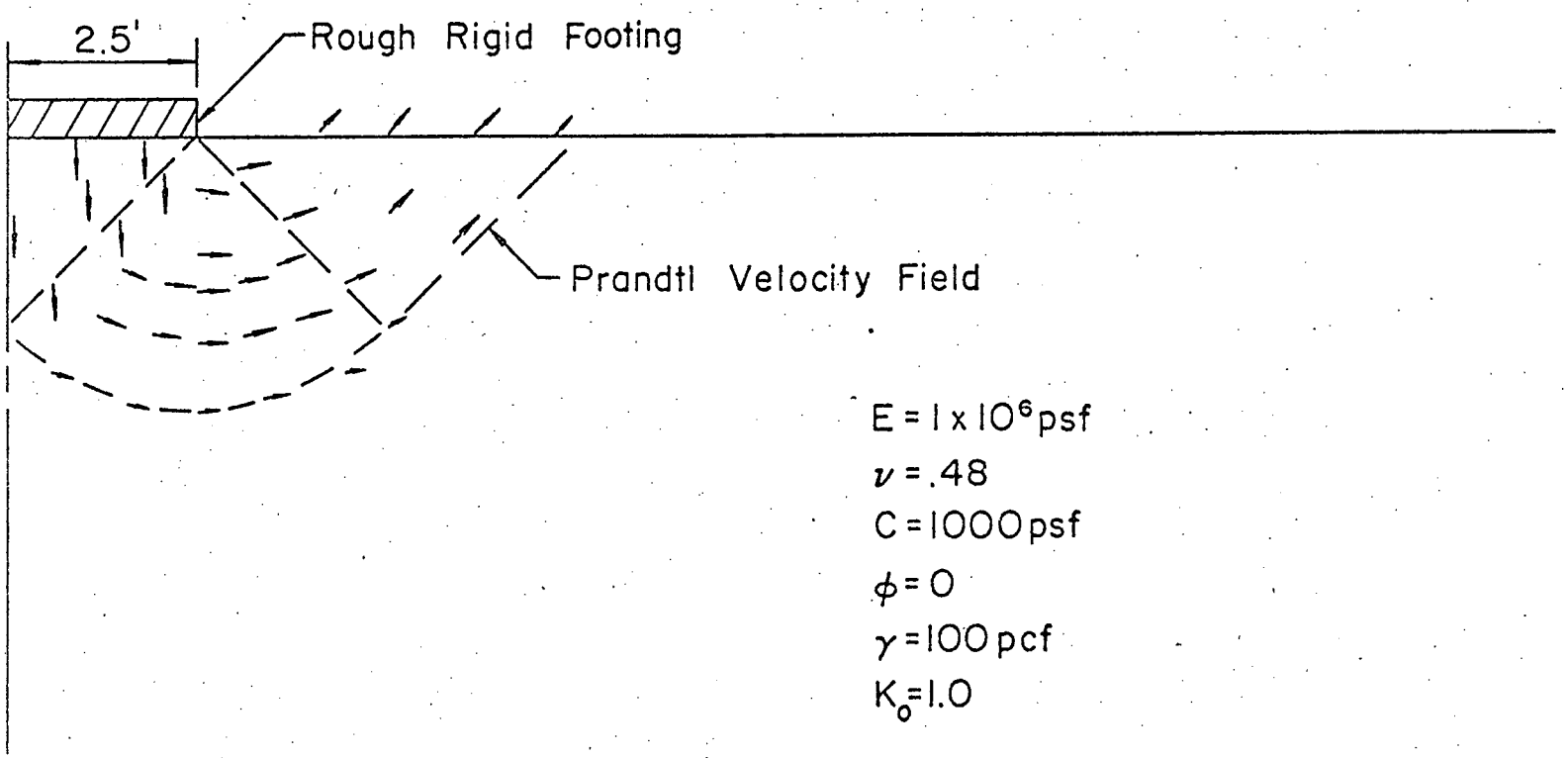

Fig. 54 Velocity Field at Numerical Limit Load (5520 psf) - Small Deformation

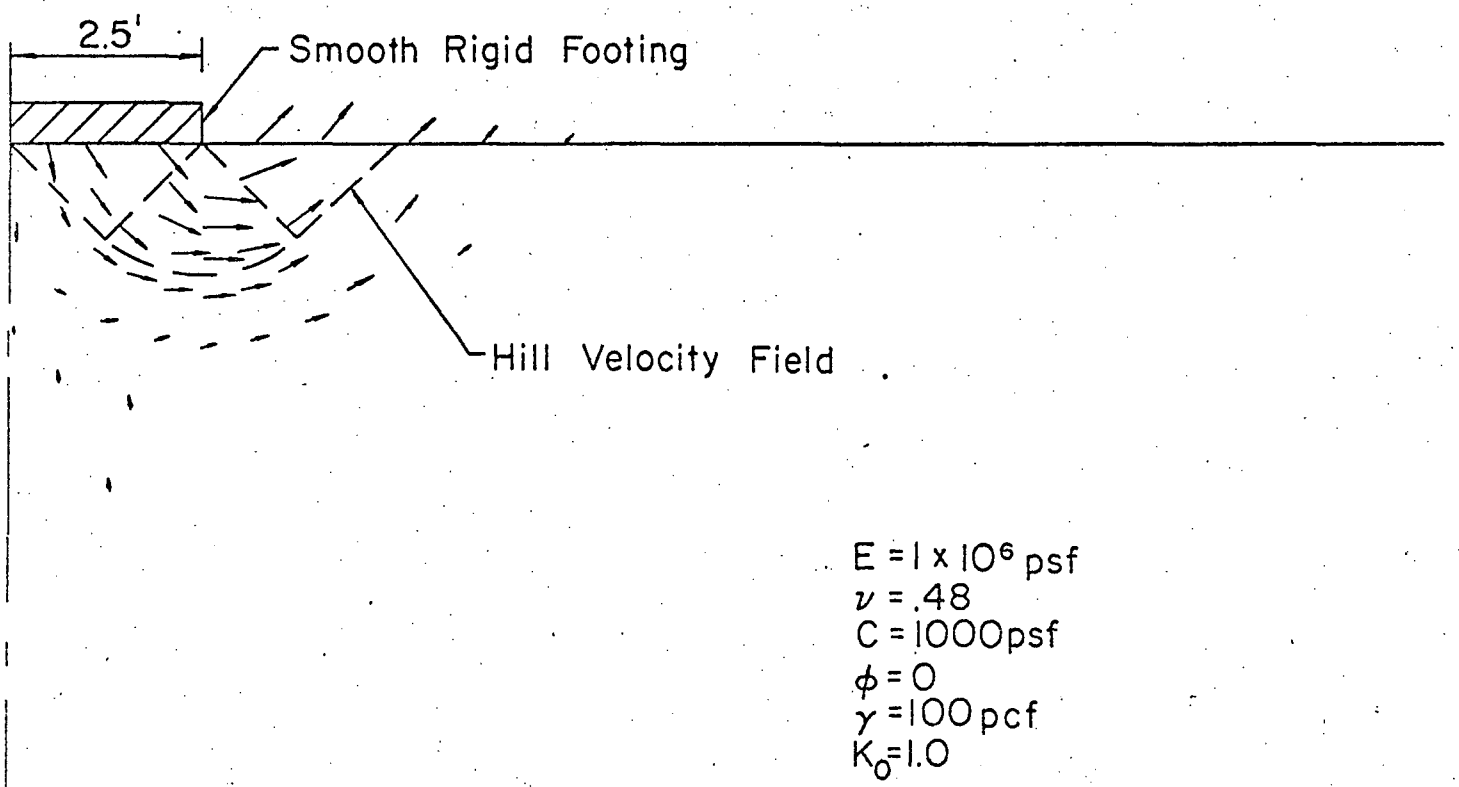

Fig. 55 Smooth Footing Velocity Field at Numerical Limit Load

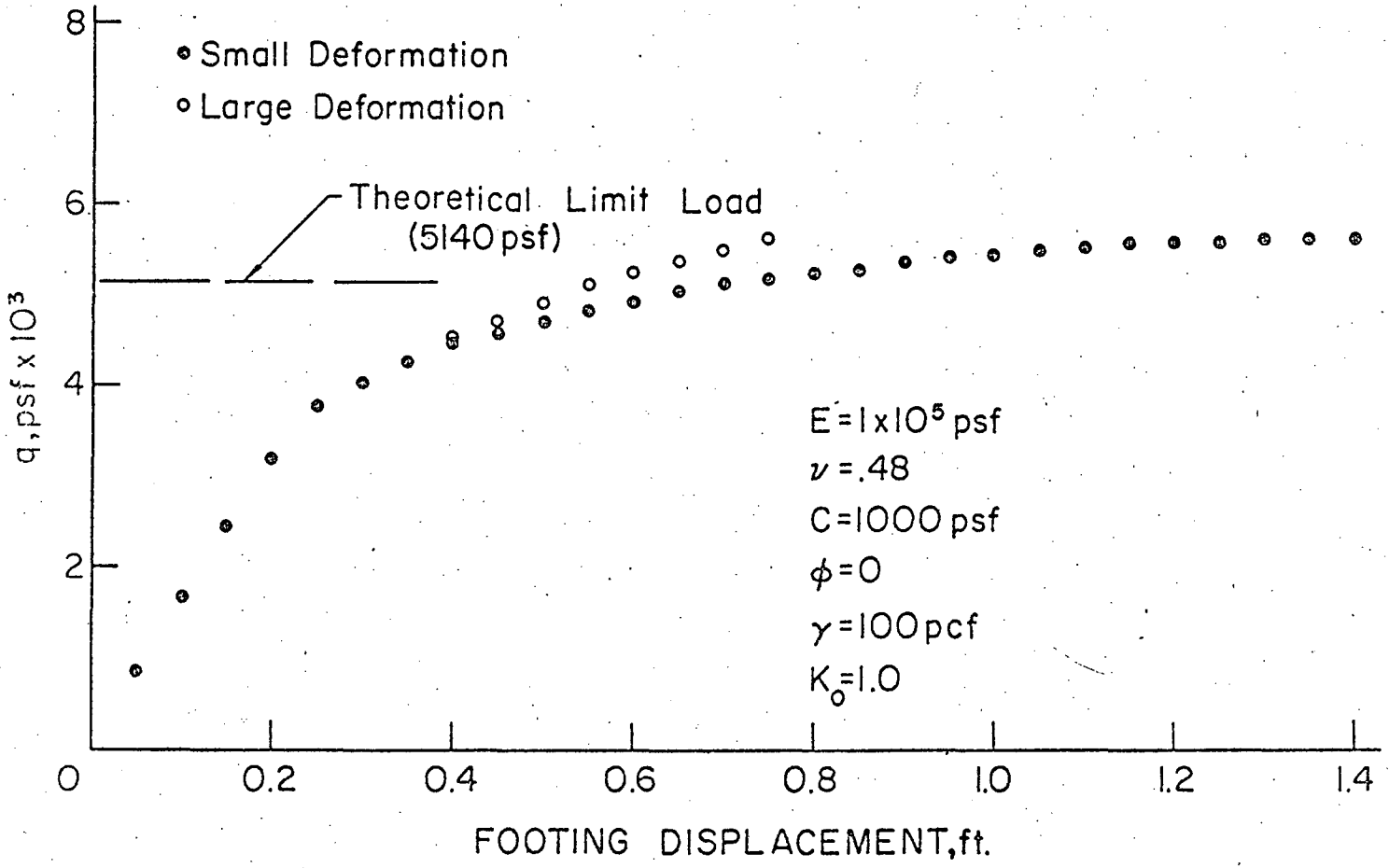

Fig. 56 Footing Load-Displacement Curves, E = $1x10^5$ psf

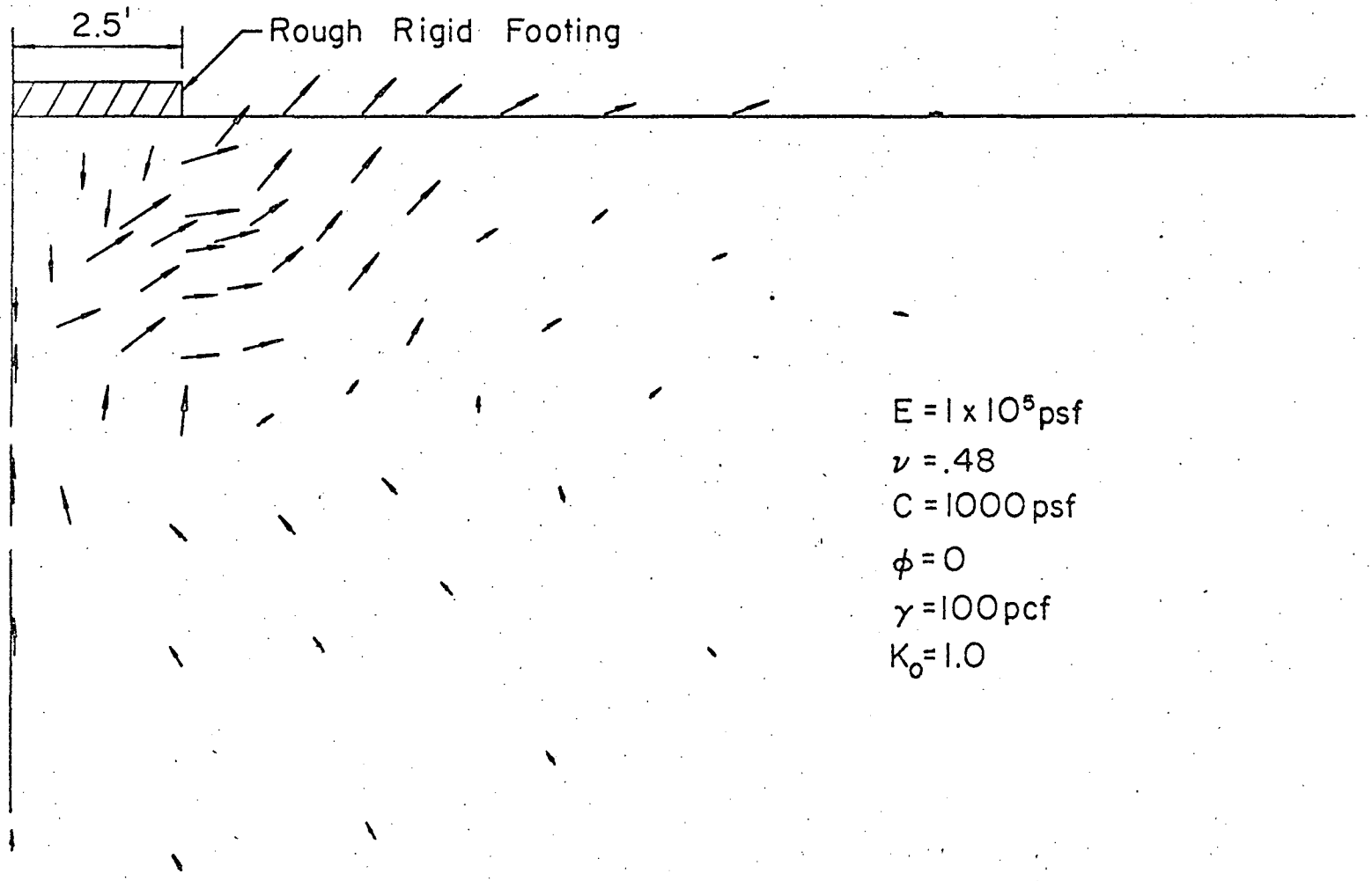

Fig. 57 Velocity Field at Maximum Load (5600 psf) - Large Deformation

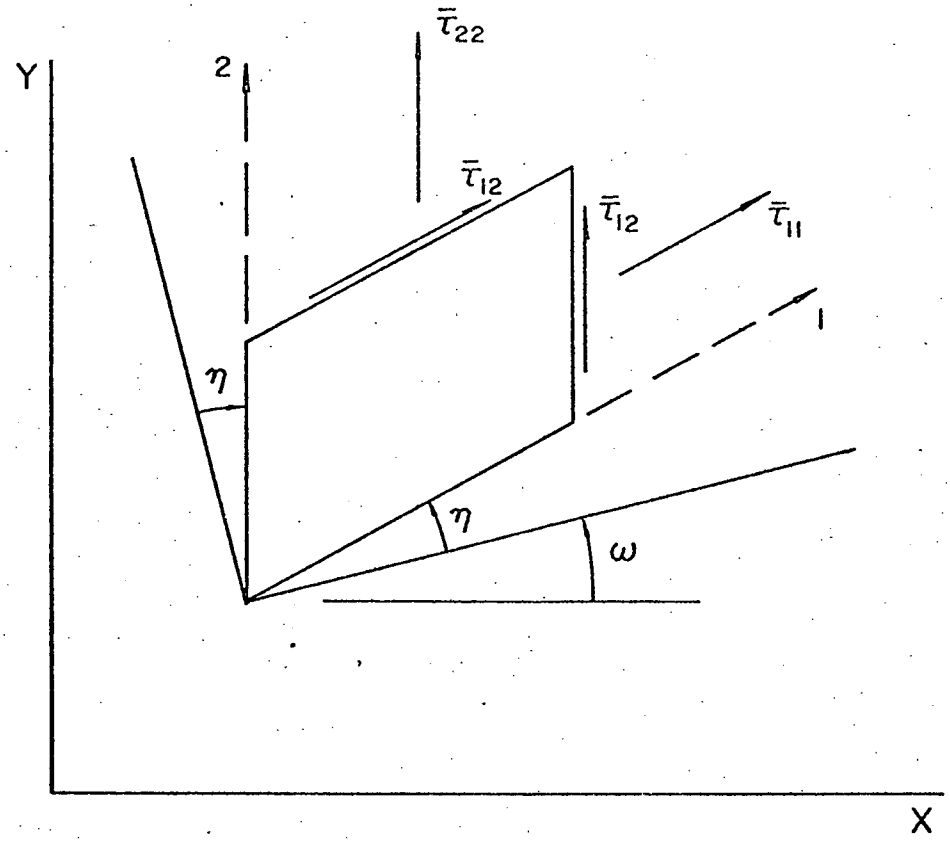

Fig. 58 Subsequent Physical Stresses Referred to a Convected Coordinate System

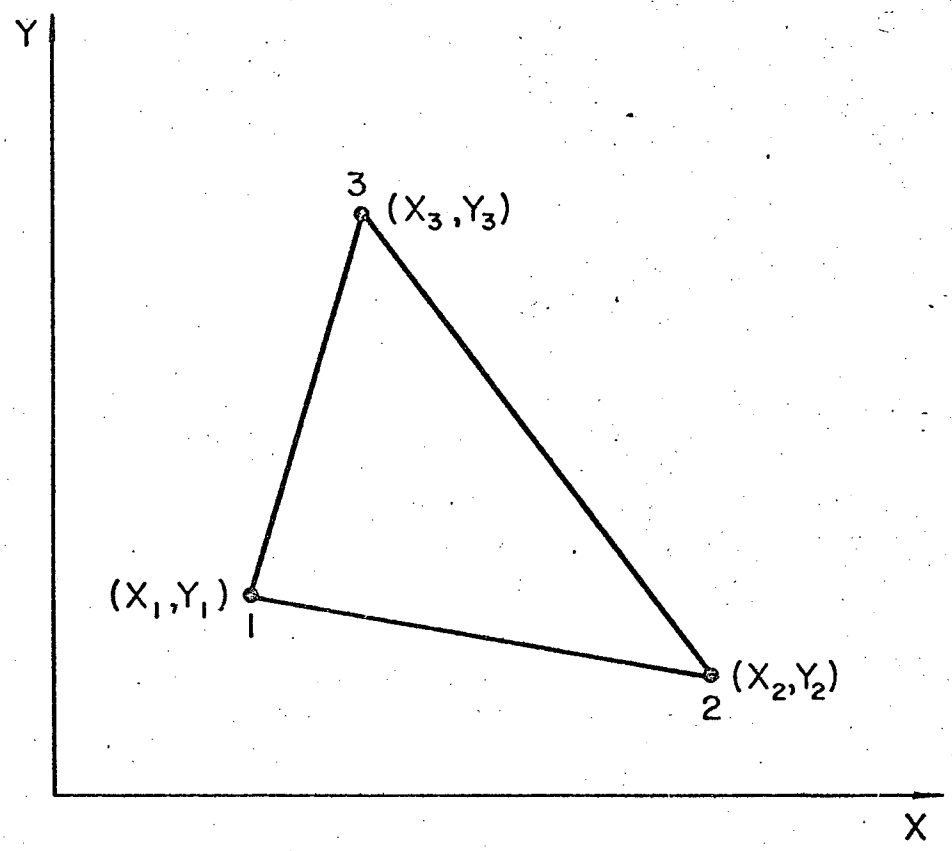

Fig. 59 Generic Finite Element

REFERENCES

1. Akyuz, F. A. and Merwin, J. E., "Solution of Nonlinear Problems of Elastoplasticity by Finite Element Method," AIAA Journal, Vol. 6, No. 10, October 1968, pp. 1825-1831.

2. Ang, A. H. S. and Harper, G. N., "Analysis of Contained Plastic Flow in Plane Solids," Journal of the Engineering Mechanics Division, ASCE, Vol. 90, No. EM5, October 1964, pp. 397-418.

3. Argyris, J. H., "Elasto-plastic Matrix Displacement Analysis of Three-Dimensional Continua," Journal of the Royal Aeronautical Society, Vol. 69, 1965, pp. 633-636.

4. Armen, H., Pifko, A. and Levine, H. S., "A Finite Element Method for the Plastic Bending Analysis of Structures," Proceedings of the Second Conference on Matrix Methods in Structural Mechanics, Wright-Patterson Air Force Base, AFFDL-TR-68-150, 1968, pp. 1301-1339.

5. Biot, M. A., "Sur la stabilite de l'equilibre elastique. Equations de l'elasticité d'un milieu soumis a'tension initiale," Annales de la Societe Scientifique de Bruxelles, Vol. 54, Ser. B, part I, 1934, pp. 18-21.

6. Biot, M. A., "Non-linear theory of Elasticity and the linearized case for a body under initial stress, Philosophical Magazine, Vol. 27, Ser. 7, 1939, pp. 468-489.

7. Biot, M. A., Mechanics of Incremental Deformations, John Wiley and Sons, Inc., New York, 1965.

8. Bishop, A. W., "The Strength of Soils as Engineering Materials," Geotechnique, Vol. 16, No. 2, June 1966, pp. 91-128.

9. Burland, J. B., "The Yielding and Dilation of Clay", correspondence, Geotechnique, Vol. 15, No. 2, June 1965, pp. 211-219.

10. Calladine, C. R., "The Yielding of Clay," correspondence, Geotechnique, Vol. 13, No. 3, September 1963, pp. 250-255.

11. Capurso, M., "A General Method for the Incremental Solution of Elastic-Plastic Problems," Meccanica, Vol. 4, No. 4, December 1969, pp. 267-280.

12. Chen, W. F. and Davidson, H. L., "Bearing Capacity Determination by Limit Analysis," Journal of the Soil Mechanics and Foundations Division, ASCE, Vol. 99, No. SM6, June 1973, pp. 433-449.

13. Christian, J. T., "Two-Dimensional Analysis of Stress and Strain in Soils, Report 3: Plane-Strain Deformation Analysis of Soil", U.S. Army Engineer Waterways Experiment Station, Contract Report No. 3-129, December 1966.

14. D'Appolonia, D. J., Poulos, H. G. and Ladd, C. C., "Initial Settlement of Structures on Clay", Journal of the Soil Mechanics and Foundations Division, ASCE, Vol. 97, No. SM10, October 1971, pp. 1359-1377.

15. Desai, C. S., "Nonlinear Analysis Using Spline Functions, Journal of the Soil Mechanics and Foundations Division, ASCE, Vol. 97, SM10, Oct. 1971, pp. 1461-1480.

16. Desai, C. S. and Reese, L. C., "Analysis of Circular Footings on Layered Soils," Journal of the Soil Mechanics and Foundations Division, ASCE, Vol. 96, No. SM4, July 1970, pp. 1289-1310.

17. Drucker, D. C., "A More Fundamental Approach to Plastic Stress-Strain Relations," Proceedings of the 1st National Congress of Applied Mechanics, June 1951, ASME, pp. 487-491.

18. Drucker, D. C., "Limit Analysis of Two- and Three-Dimensional Soil Mechanics Problems," Journal of the Mechanics and Physics of Solids, Vol. 1, 1953, pp. 217-226.

19. Drucker, D. C., "On Stress-Strain Relations for Soil and Load Carrying Capacity," Proceedings of the 1st International Conference on the Mechanics of Soil-Vehicle Systems, Torino, Minerva Tecnica, 1965, pp. 15-23.

20. Drucker, D. C., "Concepts of Path Independence and Material Stability for Soils," Rheology and Soil Mechanics, Proceedings of the IUTAM Symposium, Grenoble, Springer-Verlag, April 1964, pp. 23-43.

21. Drucker, D. C., Gibson, R. E. and Henkel, D. J., "Soil Mechanics and Work-Hardening Theories of Plasticity", Proceedings, ASCE, Vol. 81, Paper 798, September 1955.

22. Drucker, D. C. and Prager, W., "Soil Mechanics and Plastic Analysis or Limit Design," Quarterly of Applied Mathematics, Vol. 10, No. 2, July 1952, pp. 157-165.

23. Duncan, J. M. and Chang, C.-Y., "Nonlinear Analysis of Stress and Strain in Soils," Journal of the Soil Mechanics and Foundations Division, ASCE, Vol. 96, No. SM5, September 1970, pp. 1629-1653.

24. Dupuis, G. A., Hibbitt, H. D., McNamara, S. F. and Marcal, P. V., "Nonlinear Material and Geometric Behavior of Shell Structures," Computer Oriented Analysis of Shell Structures, Proceedings of a conference held at Palo Alto, California, AFFDL-TR-71-79, 1971, pp. 485-512.

25. Felippa, C. L., "Refined Finite Element Analysis of Linear and Nonlinear Two-Dimensional Structures," thesis presented to the University of California, at Berkeley, in partial fulfillment of the requirements of the degree of Doctor of Philosophy, 1966.

26. Fernandez, R. M. and Christian, J. T., "Finite Element Analysis of Large Strains in Soils, NASA research report R71-37, September 1971.

27. Fung, Y. C., "Finite Deformation," Foundations of Solid Mechanics, Prentice-Hall, Inc., Englewood Cliffs, New Jersey, 1965, pp. 934-939.

28. Gallagher, R. H., "Geometrically Nonlinear Finite Element Analysis, Proceedings of the Specialty Conference on Finite Element Methods in Civil Engineering, Mucutcheon, Mirza and Mufti, eds., McGill University, June 1972, pp. 3-33.

29. Gallagher, R. H., Padlog, J. and Bijlaard, P. P., "Stress Analysis of Heated Complex Shapes," ARS Journal, Vol. 32, No. 5, May 1962, pp. 700-707.

30. Girijavallabhan, C. and Reese, L. C., "Finite Element Method for Problems in Soil Mechanics," Journal of the Soil Mechanics and Foundations Division, ASCE, Vol. 94, No. SM2, March 1968, pp. 473-496.

31. Haisler, W. E., Strickland, J. A. and Stebbins, F. J., "Development and Evaluation of Solution Procedures for Geometrically Nonlinear Structural Analysis," AIAA Journal, Vol. 10, No. 3, March 1972, pp. 264-272.

32. Hartz, B. J. and Nathan, N. D., "Finite Element Formulation of Geometrically Nonlinear Problems of Elasticity," Recent Advances in Matrix Methods of Structural Analysis and Design, Proceedings of Japan-U.S. seminar, Tokyo, Gallagher, Yamada, and Oden, eds., U. of Alabama Press, University, 1971.

33. Hibbitt, H. D., Marcal, P. V. and Rice, J. R., "A finite element formulation for problems of large strain and large displacement," International Journal of Solids and Structures, Vol. 6, No. 8, August 1970, pp. 1069-1086.

34. Hoeg, K., "Finite Element Analysis of Strain-Softening Clay", Journal of the Soil Mechanics and Foundations Division, ASCE, Vol. 98, SM1, January 1972, pp. 43-58.

35. Hoeg, K., Christian, J. T. and Whitman, R. V., "Settlement of Strip Load on Elastic-Plastic Soil," Journal of the Soil Mechanics and Foundations Division, ASCE, Vol. 94, No. SM2, March 1968, pp. 431-445.

36. Hofmeister, L. D., Greenbaum, G. A. and Evensen, D. A., "Large Strain, Elasto-Plastic Finite Element Analysis," AIAA Journal, Vol. 9, No. 7, July 1971, pp. 1248-1254.

37. Kachanov, L. M., Foundations of the Theory of Plasticity, American Elsevier Publishing Co., Inc., New York, 1971, p. 197.

38. Ketter, R. L. and Prawel, S. P., Modern Methods of Engineering Computation, McGraw-Hill Book Co., New York, 1968.

39. Lansing, W., Jensen, W. R. and Falby, W., "Matrix Analysis Methods for Inelastic Structures," Matrix Methods in Structural Mechanics, Proceedings of the Conference held at Wright-Patterson Air Force Base, AFFDL-TR-66-80, 1965, pp. 605-633.

40. Mallett, R. H. and Marcal, P. V., "Finite Element Analysis of Nonlinear Structures," Journal of the Structural Division, ASCE, Vol. 94, No. ST9, September 1968, pp. 2081-2105.

41. Marcal, P. V., "A Stiffness Method for Elastic-Plastic Problems," International Journal for Mechanical Sciences, Vol. 7, 1965, pp. 229-238.

42. Marcal, P. V., "Finite-Element Analysis of Combined Problems of Non-Linear Material and Geometric Behavior," Computational Approaches in Applied Mechanics, E. Sevin, ed., ASME, New York, 1969, pp. 133-149.

43. Marcal, P. V. and King, I. P., "Elastic-Plastic Analysis of Two-Dimensional Stress Systems by the Finite Element Method," International Journal of Mechanical Sciences, Vol. 9, 1967, pp. 143-155.

44. Martin, H. C., "On the Derivation of Stiffness Matrices for the Analysis of Large Deflection and Stability Problems," Matrix Methods in Structural Mechanics, Proceedings of the Conference held at Wright-Patterson Air Force Base, AFFDL-TR-66-80, 1965, pp. 697-716.

45. Mendelson, A., "The Method of Successive Elastic Solutions," Plasticity: Theory and Application, The MacMillan Co., New York, 1968, pp. 164-212.

46. Mendelson, A. and Manson, S. S., "Practical Solution of Plastic Deformation Problems in Elastic-Plastic Range," NACA Technical Note 4088, 1959.

47. Methods of Analysis and Solutions of Crack Problems, Ed., G. C. Sih, Chap. 8, Application of Finite Element Method to the Calculation of Stress Intensity Factors, Noordhoff Publications, 1973, pp. 426-483.

48. Muskhelishvili, N. I., Some Basic Problems of the Mathematical Theory of Elasticity, P. Noordhoff Ltd., Groningen - The Netherlands, 1963, pp. 475-477.

49. Novozhilov, V. V., Foundations of the Nonlinear Theory of Elasticity, Graylock Press, Rochester, N. Y., 1953.

50. Oden, J. T., "Finite Element Applications in Nonlinear Structural Analysis", Proceedings of the Symposium on Applications of Finite Element Methods in Civil Engineering, Vanderbuilt University, Nashville, Tenn., 1969, pp. 419-456.

51. Oden, J. T., "Finite Elements of Elastic Bodies," Finite Elements of Nonlinear Continua, McGraw-Hill Book Co., New York, 1972, pp. 254-261.

52. Owen, D. R. J., Nayak, G. L., Kfouri, A. P. and Griffiths, J. R., "Stresses in a Partially Yielded Notched Bar--An Assessment of Three Alternative Programs," International Journal for Numerical Methods in Engineering, Vol. 6, 1973, pp. 63-73.

53. Pope, G. G., "The Application of the Matrix Displacement Method in Plane Elasto-Plastic Problems," Matrix Methods in Structural Mechanics, Proceedings of the Conference held at Wright-Patterson Air Force Base, AFFDL-TR-66-80, 1965, pp. 635-654.

54. Popov, E. P., Khojesteh-Bakht, M. and Yaghmai, S.,"Analysis of Elastic-Plastic Circular Plates," Journal of the Engineering Mechanics Division, ASCE, Vol. 93, No. EM6, December 1967, pp. 49-65.

55. Prager, W. and Hodge, P. G., "Plane Strain: Specific Problems," Theory of Perfectly Plastic Solids, Dover Publications, New York, 1968, pp. 169-173.

56. Prandtl, L., "Uber Die Haerte Plastischer Korper", Nachrichten Von Der Koeniglichen Gesellschaft Der Wissenschaften Zu Geottingen, Mathematisch-physikalische Klasse, 1920, pp. 74-85.

57. Richard, R. M. and Blacklock, J. R., "Finite Element Analysis of Inelastic Structures," AIAA Journal, Vol. 7, No. 3, March 1969, pp. 432-438.

58. Roscoe, K. H., "The Influence of Strains in Soil Mechanics," Geotechnique, Vol. 20, No. 2, June 1970, pp. 129-170.

59. Roscoe, K. H. and Burland, J. B., "On the Generalized Stress-Strain Behavior of 'Wet' Clay," Engineering Plasticity, Heyman, J. and Leckie, F. A., eds., Cambridge University Press, 1968, pp. 535-609.

60. Roscoe, K. H. and Poorooshasb, H. B., "A Theoretical and Experimental Study of Strains in Triaxial Compression Tests on Normally Consolidated Clays," Geotechnique, Vol. 13, No. 1, March 1963, pp. 12-38.

61. Roscoe, K. H., Schofield, A. N. and Thurairajah, A., "Yielding of Clays in States Wetter than Critical," Geotechnique, Vol. 13, No. 3, September 1963, pp. 211-240.

62. Roscoe, K. H., Schofield, A. N. and Thurairajah, A., "An Evaluation of Test Data for Selecting a Yield Criterion for Soils," ASTM Special Technical Publication No. 361, Laboratory Shear Testing of Soils, 1963, pp. 111-128.

63. Roscoe, K. H., Schofield, A. N. and Wroth, C. P., "On the Yielding of Soils", Geotechnique, Vol. 8, No. 1, March 1958, pp. 22- 53.

64. Schofield, A. and Wroth, P., Critical State Soil Mechanics, McGraw-Hill Book Co., New York, 1968.

65. Shield, R. T., "Plastic Potential Theory and the Prandtl Bearing Capacity Solution", Journal of Applied Mechanics, Vol. 21, No. 2, June 1954, pp. 193-194.

66. Shield, R. T., "On Coulomb's Law of Failure in Soil," Journal of Mechanics and Physics of Solids, Vol. 4, No. 1, October 1955, pp. 10-16.

67. Smith, I. M., "Incremental Numerical Solution of a Simple Deformation Problem in Soil Mechanics," Geotechnique, Vol. 20, No. 4, December 1970, pp. 357-372.

68. Smith, I. M. and Kay, S., "Stress Analysis of Contractive or Dilative Soils," Journal of the Soil Mechanics and Foundations Division, ASCE, Vol. 97, No. SM7, July 1971, pp. 981-997.

69. Strickland, J. A., Haisler, W. E. and Von Riesemann, W. A., "Geometrically Nonlinear Structural Analysis by Direct Stiffness Method," Journal of the Structural Division, ASCE, Vol. 97, No. ST9, September 1971, pp. 2229-2314.

70. Swedlow, J. L., Williams, M. L. and Yang, W. H., "Elasto-Plastic Stresses and Strains in Cracked Plates," Proceedings of the First International Conference on Fracture, Vol. 1, 1965, pp. 259-282.

71. Tang, W. H. and Hoeg, K., "Two-Dimensional Analysis of Stress and Strain in Soils, Report 5: Plane-Strain Loading of a Strain-Hardening Soil", U.S. Army Engineer Waterways Experiment Station, Contract Report No. 3-129, March 1968.

72. Turner, M. J., Dill, E. H., Martin, H. C. and Melosh, R. J., "Large deflections of structures subjected to heating and external loads," Journal of the Aero/Space Sciences, Vol. 27, No. 2, February 1960, p. 97.

73. Valliappan, S., discussion, Journal of the Soil Mechanics and Foundations Division, ASCE, Vol. 95, No. SM2, March 1969, pp. 676-678.

74. Wilson, E. L., "Finite Element Analysis of Two Dimensional Structures," thesis presented to the University of California at Berkeley, in partial fulfillment of the degree of Doctor of Philosophy, 1963.

75. Wissmann, J. W., "Nonlinear Structural Analysis; Tensor Formulation," Matrix Methods in Structural Mechanics, Proceedings of the Conference held at Wright-Patterson Air Force Base, AFFDL-TR-66-80, 1965, pp. 679-696.

76. Witmer, E. A. and Kotanchik, J. J., "Progress Report on Discrete-Element Elastic and Plastic Analyses of Shells of Revolution Subjected to Axisymmetric and Asymmetric Loading", Proceedings of the Second Conference on Matrix Methods of Structural Mechanics, Wright-Patterson Air Force Base, AFFDL-TR-68-150, 1968, pp. 1341-1453.

77. Yaghmai, S., "Incremental Analysis of Large Deformations in Mechanics of Solids with Applications to Axisymmetric Shells of Revolution, NASA contractor report CR-1350, June 1969.

78. Yamada, Y. and Yoshimura, N., "Plastic Stress-Strain Matrix and its Application for the Solution of Elastic-Plastic Problems by the Finite Element Method", International Journal of Mechanical Sciences, Vol. 10, 1968, pp. 343-354.

79. Zienkiewicz, O. C., The Finite Element Method in Engineering Science, McGraw-Hill, London, 1971.

80. Zienkiewicz, O. C. and Nayak, G. C., "A General Approach to Problems of Large Deformation and Plasticity Using Isoparametric Elements, presented at 3rd Conference on Matrix Methods in Structural Mechanics--Wright-Patterson Air Force Base, October 1971.

81.. Zienkiewicz, O. C. and Nayak, G. C., Elasto-Plastic Stress Analysis. A Generalization for Various Constitutive Relations Including Strain Softening," International Journal for Numerical Methods in Engineering, Vol. 5, 1972, pp. 113-135.

82. Zienkiewicz, O. C. and Naylor, D. J., "The Adaption of Critical State Soil Mechanics Theory for use in Finite Elements," Stress-Strain Behavior of Soils, ed. by Parry, R. H. G., G. T. Foulis and Co., Ltd., Henley-on-Thames, Oxfordshire, 1971, pp. 537-547.

83. Zienkiewicz, O. C. and Naylor, D. J., "Finite Element Studies of Soils and Porous Media," Lectures on Finite Element Methods in Continuum Mechanics, delivered at Advanced Study Institute held at Lisbon, Portugal, September 1971, ed. by Oden, J. T. and Oliveira, E. R. A., pp. 459-493.

84. Zienkiewicz, O. C., Valliappan, S. and King, I. P., "Elasto-Plastic Solutions of Engineering Problems: "Initial Stress" Finite Element Approach," International Journal for Numerical Methods in Engineering, Vol. 1, 1969, pp. 75-100.

APPENDIX I - DERIVATION OF THE Ψ MATRIX

As a demonstration of how the Ψ matrix can be derived, we show that to the first order,

$$\Delta S_{11} = \Delta\tau_{11} - \sigma_{11}\, e_{11} + \sigma_{11}\, e_{22} - 2\,\sigma_{12}\, e_{12} \tag{A1.1}$$

We begin by considering yet another description of the stress state in the subsequent configuration. Referring to Fig. 13 we consider an infinitesimal element which in the initial configuration is square and whose sides are parallel to the global coordinate system. In the subsequent configuration, the square has been rotated ω radians (to the first order) and has been deformed into a parallelogram (Fig. 58) where to the first order,

$$\eta = e_{12} \tag{A1.2}$$

Associated with the deformed element is a set of locally convected base vectors labeled 1 and 2 in Fig. 58. Stress components $\bar{\tau}_{ij}$ are referred to this locally convected system and define force per unit of area in the subsequent configuration. Reducing Novozhilov's (49) three-dimensional equations to the plane strain case, we have,

$$S_{11} = \left(\frac{1 + 2\,\epsilon_{22}}{1 + 2\,\epsilon_{11}}\right)^{1/2} \bar{\tau}_{11} \tag{A1.3}$$

$$S_{22} = \left(\frac{1 + 2\,\epsilon_{11}}{1 + 2\,\epsilon_{22}}\right)^{1/2} \bar{\tau}_{22} \tag{A1.4}$$

$$S_{12} = \bar{\tau}_{12} \tag{A1.5}$$

Referring to Figs. 14 and 58, we note the following transformation

$$\bar{\tau}_{11} = \frac{\tau_{11} \cos^2\eta + \tau_{22} \sin^2\eta - \tau_{12} \sin 2\eta}{\cos^2\eta - \sin^2\eta} \tag{A1.6}$$

Taking a Taylor expansion in η about zero and retaining only linear terms, Eq. A1.6 reduces to

$$\bar{\tau}_{11} = \tau_{11} - 2\,\tau_{12}\,\eta \tag{A1.7}$$

Substituting Eq. A1.7 into Eq. A1.3 we have

$$S_{11} = \left(\frac{1 + 2\,\epsilon_{22}}{1 + 2\,\epsilon_{11}}\right)^{1/2} [\tau_{11} - 2\,\tau_{12}\,\eta] \tag{A1.8}$$

A linear Taylor expansion of Eq. A1.8 with respect to ϵ_{11} and ϵ_{22} yields

$$S_{11} = (1 + \epsilon_{22} - \epsilon_{11})\,(\tau_{11} - 2\,\tau_{12}\,\eta) \tag{A1.9}$$

or, for a first order approximation,

$$S_{11} = (1 + e_{22} - e_{11})\,(\tau_{11} - 2\,\tau_{12}\,\eta) \tag{A1.10}$$

Substituting Eqs. 71 and 76 into Eq. A1.10 we have,

$$\Delta S_{11} + \sigma_{11} = (1 + e_{22} - e_{11})\,(\Delta\tau_{11} + \sigma_{11} - 2\,[\Delta\tau_{12} + \sigma_{12}]\,e_{12}) \tag{A1.11}$$

Finally, eliminating terms which are nonlinear with respect to the incremental variables, we have

$$\Delta S_{11} = \Delta\tau_{11} - \sigma_{11}\,e_{11} + \sigma_{11}\,e_{22} - 2\,\sigma_{12}\,e_{12} \tag{A1.12}$$

APPENDIX II - CONSTANT STRAIN TRIANGLE MATRICES

We refer the reader to Ref. 79 for a detailed discussion of the constant strain triangle. Referring to Fig. 59, we write a linear displacement expansion over the element,

$$\begin{Bmatrix} u_1 \\ u_2 \end{Bmatrix} = [N] \{v\} \tag{A2.1}$$

where u_1 and u_2 are the X and Y displacements respectively at a generic point in the element, and $\{v\}$ is a vector of element nodal displacements,

$$\{v\} = \begin{Bmatrix} u_{11} \\ u_{21} \\ u_{12} \\ u_{22} \\ u_{13} \\ u_{23} \end{Bmatrix} \tag{A2.2}$$

where, for example, u_{13} is the X displacement component of node 3. Also,

$$[N] = \begin{bmatrix} \ell_1 & 0 & \ell_2 & 0 & \ell_3 & 0 \\ 0 & \ell_1 & 0 & \ell_2 & 0 & \ell_3 \end{bmatrix} \tag{A2.3}$$

where ℓ_1, ℓ_2 and ℓ_3 are the so-called area coordinates of the triangle (79), that is,

$$\ell_1 = (a_1 + b_1 X + c_1 Y)/2A \tag{A2.4}$$

$$\ell_2 = (a_2 + b_2 X + c_2 Y)/2A \tag{A2.5}$$

$$\ell_3 = (a_3 + b_3 X + c_3 Y)/2A \tag{A2.6}$$

and

$$a_1 = X_2 Y_3 - X_3 Y_2 \tag{A2.7}$$

$$b_1 = Y_2 - Y_3 \tag{A2.8}$$

$$c_1 = X_3 - X_2 \tag{A2.9}$$

$$a_2 = X_3 Y_1 - X_1 Y_3 \tag{A2.10}$$

$$b_2 = Y_3 - Y_1 \tag{A2.11}$$

$$c_2 = X_1 - X_3 \tag{A2.12}$$

$$a_3 = X_1 Y_2 - X_2 Y_1 \tag{A2.13}$$

$$b_3 = Y_1 - Y_2 \tag{A2.14}$$

$$c_3 = X_2 - X_1 \tag{A2.15}$$

In addition, the area of the triangle is denoted by A.

Finally, we define matrices [B] and $[\tilde{B}]$,

$$[B] = \frac{1}{2A} \begin{bmatrix} b_1 & 0 & b_2 & 0 & b_3 & 0 \\ 0 & c_1 & 0 & c_2 & 0 & c_3 \\ c_1 & b_1 & c_2 & b_2 & c_3 & b_3 \end{bmatrix} \tag{A2.16}$$

$$[\tilde{B}] = \frac{1}{2A} \begin{bmatrix} b_1 & 0 & b_2 & 0 & b_3 & 0 \\ 0 & c_1 & 0 & c_2 & 0 & c_3 \\ c_1 & b_1 & c_2 & b_2 & c_3 & b_3 \\ -c_1/2 & b_1/2 & -c_2/2 & b_2/2 & -c_3/2 & b_3/2 \end{bmatrix} \tag{A2.17}$$

APPENDIX III - THE COMPUTER PROGRAM

All of the solutions presented here were generated by a FORTRAN IV computer program designed and coded by the author. The program was compiled and executed on Lehigh University's CDC 6400 computer, SCOPE 3.4, using the FTN compiler.

The program is capable of solving, numerically, elastic-perfectly plastic, large deformation boundary value problems (plane strain). In particular the program incorporates the Drucker-Prager model which contains the von Mises model as a special case. It can, of course, also solve linear elastic, elastic large deformation and elastic-plastic small deformation problems. The current version of the program was designed specifically to handle boundary conditions peculiar to punch problems where forces or displacements can be prescribed beneath the punch. Simple modifications must be made in order to treat more general boundary conditions and load conditions.

The input consists essentially of mesh data, increment data and material property data. All mesh data must be read in since the program contains no algorithms for automatic mesh generation. The number of increments and the size of each increment (force or displacement) must also be read in since the program does not have the capability of making decisions concerning increment size.

The output at the end of each increment consists of:

1) total nodal displacements,
2) incremental nodal displacements,

3) residual vector,

4) total element stresses, and

5) the yield condition of each element.

At the end of every third increment nodal stresses are printed.

Element stiffness matrices and the global stiffness matrix are generated in a single pass through all of the elements. At any one time, element data and a partial global stiffness matrix corresponding to 25 quadrilateral elements (100 triangular elements) are stored in central memory. Thus, reading and writing of scratch tapes are required, but the program can be compiled in 70,000 octal words (28,672 decimal).

Only the lower banded half of the symmetric global stiffness matrix is generated and stored. In the linear equation solution subroutine, this entire matrix is contained in core. Thus although there is no limit on the number of elements that can be handled, the banded half stiffness matrix must contain less than 15,000 elements (decimal). For example, if a mesh contained 250 nodes, the half band width must be less than 15 nodes.

For mesh 3 (Fig. 29) with quadrilaterals defined by four constant strain triangles, the nonlinear solutions required about 13 seconds of central processing time per increment and 12 seconds of peripheral processing time per increment. Thus a typical nonlinear analysis which required, say, 30 increments would cost about 60 dollars and take about 400 and 360 seconds of CP and PP time respectively.

APPENDIX IV - NOTATIONS

$a_1, b_1, c_1, a_2, b_2, c_2, a_3, b_3, c_3$ = defined by Eqs. A2.7 - A2.15

A = area of triangle

$[A]$ = initial stress matrix

B = defined by Eq. 20

$[B]$ = matrix relating element strain to element nodal displacements

$[\tilde{B}]$ = matrix relating element strain and rotation to nodal displacements

C = cohesive strength

$[D]$ = elastic-plastic constitutive matrix

e_v = void ratio

e_{ij} = infinitesimal strain tensor

$\{e\}$ = strain vector

$\{\tilde{e}\}$ = augmented strain vector

E = Young's modulus

f = yield function

F_i = body force vector

G = shear modulus

H = defined Eq. 58

H_1, H_2, H_3, H_4 = defined by Eq. 26

J_2 = second invariant of the deviatoric stress tensor

k = material constant of Drucker-Prager yield function

$[K]$ = element tangent stiffness in Chap. 3; global tangent

stiffness in Chap. 4

$[K_G]$ = element geometric stiffness

$[K_m]$ = element material stiffness

ℓ_o = length used in example problem shown in Fig. 19

ℓ_1, ℓ_2, ℓ_3 = area coordinates of a triangle

L = length of cantilever beam in Chap. 5; defined by Eq. 55 in Chap. 2

M = material constant of modified Cam-clay

[N] = coordinate function matrix associated with constant strain triangle

p = hydrostatic stress component

p_o = strain hardening parameter

{P} = element load vector in Chap. 3; global load vector in Chap. 4

q = average vertical stress beneath footing

q_o = average vertical stress beneath footing at limit state

R = defined by Eq. 56

{R} = residual vector

s = surface area

s_{ij} = deviatoric stress tensor

S_{ij} = Kirchhoff stress tensor

t = time like parameter

T_i = traction vector

u_i = incremental displacement vector

$u_{11}, u_{21}, u_{12}, u_{22}, u_{13}, u_{23}$ = nodal displacements of a generic finite element

$\{U\}$ = two-dimensional incremental displacement vector

$\{v\}$ = vector of element nodal displacements

$\{V\}$ = displacement vector of discretized body

x_i = cartesian coordinates

X,Y,Z = global coordinates

α = material constant of Drucker-Prager yield function

β = instantaneous elastic shear modulus associated with modified Cam-clay

γ = weight density

γ_{xy} = engineering shearing strain

δ = denotes a virtual quantity

δ_{ij} = Kronecker delta

δ_m = maximum mobilized friction angle beneath footing

Δ = end displacement of cantilever beam

ε_{ij} = Green's strain tensor

η = material constant of modified Cam-clay in Chap. 2 and an angle in Appendix I

λ = constant relating plastic strain vector and normal to yield surface

Λ = material constant of modified Cam-clay

ν = Poisson's ratio

ξ_i = cartesian coordinates

ρ = mass density

σ = applied stress

σ_o = yield stress is simple tension

σ_{ij} = Cartesian stress tensor

$\sigma_1, \sigma_2, \sigma_3$ = principal stresses

τ_{ij} = locally rotated stress tensor

$\bar{\tau}_{ij}$ = stress tensor associated with convected coordinates

φ = soil friction angle

ψ = defined by Eqs. 60 and 61

$[\Psi]$ = matrix relating Kirchhoff stress tensor and τ_{ij}

ω_{ij} = infinitesimal rotation tensor

VITA

The author is the son of Hugh L. and Elizabeth W. Davidson and was born on March 12, 1940 in Tacoma Park, Maryland. He is married to the former Genevieve P. Mies.

He graduated from Damascus High School, Damascus, Maryland in 1958 and was awarded a Bachelor of Science in Civil Engineering in 1963 from the University of Maryland. While at the University of Maryland he was elected to Tau Beta Pi and Chi Epsilon. He attended Lehigh University from 1963 to 1965 while working as a half time research assistant and was awarded a Master of Science in Civil Engineering. He returned to Lehigh in 1970 to study for a doctorate and work as a teaching assistant. He has also done graduate study at the University of California at Berkeley and at the University of Connecticut.

The author's industrial experience consists of eight months as a research engineer with the Naval Ship Research and Development Center, two years as a structural research engineer with General Dynamics/Electric Boat and eight months as a mechanical development engineer with General Electric.